SUBCONTINUUM THERMAL TRANSPORT IN TIP-BASED THERMAL ENGINEERING

by

Sina Hamian

A dissertation submitted to the faculty of
The University of Utah
in partial fulfillment of the requirements for the degree of

Doctor of Philosophy

Department of Mechanical Engineering

The University of Utah

May 2017

The University of Utah Graduate School

STATEMENT OF DISSERTATION APPROVAL

The dissertation of **Sina Hamian**

has been approved by the following supervisory committee members:

Keunhan Park	, Chair	**02/28/2017** Date Approved
Mathieu Francoeur	, Member	**02/28/2017** Date Approved
Bruce Gale	, Member	**02/28/2017** Date Approved
Massood Tabib-Azar	, Member	**02/28/2017** Date Approved
Taylor Sparks	, Member	**02/28/2017** Date Approved

and by **Tim Ameel** , Chair/Dean of

the Department/College/School of **Mechanical Engineering**

and by David B. Kieda, Dean of The Graduate School.

ABSTRACT

For the past two decades, tip-based thermal engineering has made remarkable advances to realize unprecedented nanoscale thermal applications, such as thermomechanical data storage, thermophysical/chemical property characterization of materials in nanometer scale, and scanning thermal imaging and analysis. All these applications involve localized heating with elevated temperature, generally in the order of mean free paths of heat carriers, thus necessitates fundamental understanding of sub-continuum thermal transport across point constrictions and within thin films. Considering the demands, this dissertation is divided into three main scopes providing: (1) a numerical model that provides insight onto nanoscale thermal transport, (2) an electrothermal characterization of a heated microcantilever as a localized heating source, and (3) qualitative measurement of tip-substrate thermal transport using high resolution nanothermometer/heater.

This dissertation starts with a literature review on the three aforementioned scopes followed by a numerical model for two-dimensional transient ballistic-diffusive heat transfer combining finite element analysis with discrete ordinate method (DOM-FEA), seeking to provide insight on subcontinuum thermal transport. The phonon Boltzmann transport equation (BTE) under grey relaxation time approximation is solved for different Knudsen numbers. Next, a thermal microcantilever, as one of the main tools in tip-based thermal engineering, is characterized under periodic heating operation in air and vacuum using 3ω technique. A three-dimensional FEA simulation of a thermal microcantilever is

used to model heat transfer in frequency domain resulting in good agreement with the experiment. Next, quantitative thermal transport is measured by a home-built nanothermometer fabricated using combination of electron-beam lithography and photolithography. An atomic force microscope (AFM) cantilever is used to scan over the sensing probe of the nanothermometer at an elevated temperature causing local cooling. The experiment is done in air resulting in a tip-substrate effective thermal conductance of 32.5 nW/K followed by theoretical calculations predicting contribution of solid-solid thermal conduction to be 48%. Finally, the same experiment is conducted in vacuum with similar operating condition, showing 50% contribution of solid-solid conductance, which is in good agreement with the theory, assuming no water meniscus in vacuum condition. The outcomes of these studies provide a strong platform to fundamentally understand thermal transport at the micro/nanometer scale.

To my father
Alireza Hamian.
And his great heart, which stopped beating way too early, yet is closer to me than ever.
I have missed you dad.

To my mother,
Shahin Seif,
her smiles, and her patience. All I have is because of her.

To Nima, my lovely younger brother.
To Mina, my amazing sister, and ArashMehr her cute son.
To Sirvan, my Khan Dadash, the man of experiences, and Lia, his beautiful daughter.

TABLE OF CONTENTS

NOMENCLATURE

C	volumetric heat capacity (J/K-m^3)
D_p	phonon density of state (m^{-3})
e_0^*	nondimensional emissive power
e''	directional energy density (J/m^3 Sr)
e_0''	equilibrium energy density (J/m^3)
E_n	exponential integral
f	phonon distribution function
f_0	phonon distribution function at equilibrium
H	height of the 2-D domain (m)
Kn	Knudsen number
L	length of the 2-D domain (m)
$\hat{\mathbf{n}}$	outward-pointing normal from the domain
q''	heat flux (W/m^2)
$\hat{\mathbf{r}}$	position vector
$\hat{\mathbf{s}}$	direction vector
t	time (s)
T	temperature (K)

v_g phonon group velocity (m/s)

W weight function of Gaussian quadrature

Greek Symbols

θ polar angle (rad)

Θ dimensionless temperature

Λ phonon mean free path (m)

τ relaxation time (s)

μ directional cosine

ξ optical thickness

φ azimuthal angle (rad)

ω angular frequency (s^{-1})

Ω solid angle (Sr)

Subscripts and Superscripts

b boundary

m azimuthal angle distribution

n polar angle distribution

p phonon

r direction

SS steady state

ACKNOWLEDGEMENTS

I would like to highly acknowledge the everyday support of my wonderful advisor, Professor Keunhan Park, and express my deepest gratitude for his untiring guidance during my studies. This research would have not been accomplished without his encouragements, support, and advice. Also, I would like to acknowledge the distinguished members of my dissertation committee, Professor Mathieu Francoeur, Professor Bruce Gale, Professor Massood Tabib-Azar, and Professor Taylor Sparks. I have benefited from their guidance at different occasions along my research path. My special thanks goes to Dr. Ryan Murdick, former scientist at the RHK Technology Inc., who designed and manufactured the custom-built atomic force microscope (AFM) with which I was able to accomplish a significant part of my research.

Also, I acknowledge the valuable advice I received from Professor Mohammad Faghri of the University of Rhode Island, Professor Mohammad Behshad Shafii of Sharif University of Technology, my Master's advisor, and Professor Majid Ghassemi of K.N.Toosi University of Technology. My gratitude also goes to my former colleagues at the University of Rhode Island, Dr. Toru Yamada, Andrew Gauffreau, Timothy Walsh, and Nola Palombo along with my current colleagues at the University of Utah, Mohammad Ghashami, Amun Jarzembski, Devon Jensen, and Cedric Shaskey. They were always there for brainstorming and for great discussions on how to overcome obstacles. My special appreciation goes to Meisam Taasori, AmirHossein Eskandari, and Sara Arezoomandan,

for their time to discuss issues in the electrical engineering, numerical modeling, and material science parts of this research. I would like to thank my officemates Sheila Edalatpour, Michael Bernardi, John DeSutter, Vahid Hatamipour, Fatemeh Esmaeili, Lei, and Mike Starks for the great time we always had together. Also, I would like to thank my friends Roozbeh Gholizadeh, Kiavash Fayyaz Shahandashti, Amir Banari, Hediyeh Hosseini, Telli Davoudi, Farid Moghim, Sara Kadkhodaii, Reza Aghajani, Ladan Karimi, Noushin Rostami, Hassan Allami, Ali Shafii, Taraneh Kalati, Babak Goshayeshi, Hadi Javan, Ramin Nasrabadi, Sanam Maghsoudnia, Mahsa Mirzargar, Mina Ghashami, Mohammad Yazdian, Amir Shirazi, Arash Shirazi, Tayyebeh Tajalibakhsh, Mohsen Zayernoori, Mohammad Reza Abtahi, Amin Mivehchi, Arash Bigdeli, Christopher Turgeon, Amir Motlagh, Farhad Shiri, Hossein Mehrpour, Pouya Sabetian, Shakiba Fallahi, Valentin Romanov, Sarvenaz Chaeibakhsh, Elham Norasteh, Jaquiline Beckvermit, Nathan Miller, Henis Carcani, Saeid Taheri, Saeide Keivani, Sepideh Emami, Sara Fotros, Roozbeh Mirhosseini, Hassan Tavakol, Hesam Tavakol, Arad Lajevardi, Erfan Goharian, Judith Ross, Kaveh Narimani, Noosha Narimani, Morteza Sofla, Ali Hedayat Mofidi, Mansour Ariazand, and others with whom I enjoyed my time during my PhD studies.

Finally, I would like to express my deepest appreciation to my family for their love from thousands of miles away. My mother, Dr. Shahin Seif, who has always been there for me, and my older brother, Sirvan Hamian, my sister, Dr. Mina Hamian, and my younger brother Nima Hamian for their kindness. This dissertation is especially dedicated to the heart of my father which stopped too soon yet I do my best to keep it happy by continuing to reach for the best.

CHAPTER 1

INTRODUCTION

Over the past three decades, nanotechnology has been subject to unprecedented advances in different applications, such as healthcare [1–3], energy [4–6], and industry [7,8], with direct impact on human life. As a side product, nanoart has attracted attention by depicting images with nanometer-sized features, familiarizing the general audience with this novel technology [9,10]. When it comes to visualizing extremely small features, different instruments including, but not limited to, the scanning electron microscope (SEM) [11], tunneling electron microscope (TEM) [12], atomic force microscope (AFM) [13], scanning thermal microscope (SThM) [14], and near-field scanning optical microscope (NSOM) [15] have been invented. Each of these revolutionary inventions has provided a promising platform for further investigation in the world of extremes in small length scale, allowing further advances in nanotechnology. Meanwhile, breakthroughs in materials and technology resulted in a shrinkage of micro/nano electromechanical devices [16], with an emphasis on the importance of effective thermal management in such systems [17].

Scanning thermal microscopy, as one of the main tools in tip-based thermal engineering, provides a variety of applications in nanotechnology, raising strong demands to understand fundamentals of thermal transport on a mesoscopic scale. This is the main

reason behind the increased investigation into thermal science which has been well-known on a macro scale for the past century [18,19], yet is less well-known on a small scale [20–22]. To start with, it is crucial to understand the theory behind thermal energy transport at the micro/nanometer scale. Then it is important to characterize the thermal behavior of devices used in tip-based thermal engineering. Finally, it is important to quantitatively measure the contributions of different heat transfer mechanisms involved in an extremely miniaturized medium. As of now, different methods and various approaches by different research groups, discussed in the following subsections, are applied to address these subjects, yet further investigation is required to better enlighten the path and investigate remaining unknowns.

In this dissertation, the aforementioned subjects are addressed, starting with a numerical simulation of phonon thermal transport in thin films. For the first time, a two-dimensional phonon Boltzmann transport equation (BTE) is solved using a commercial package, COMSOL Multiphysics, widely available to public. This provides a strong tool to model nanoscale heat transfer problems, emphasizing the effect of dominant energy carriers with respect to length scale. This is followed by numerical and experimental characterization of the thermal behavior of an AFM thermal microcantilever, an important player in tip-based thermal engineering, under periodic operational conditions. The numerical simulation, for the first time, models a thermal cantilever as a three-dimensional domain. Finally, a quantitative study on thermal transport between a sharp AFM cantilever tip in contact with a home-built nanothermometer/heater is presented, analyzing different thermal transport mechanisms between a locally heated sensing probe and the tip. In this study, the smallest-ever fabricated four-probe resistive nanothermometer is used to

quantitatively measure tip-substrate thermal transport, averaging the temperature over a small area of the sensing probe of the nanothermometer. The following subsections read the latest reports on the theory and fundamentals of thermal transport in nanometer scale, followed by an overview of AFM and thermal microcantilevers, finally recent studies in characterizing different thermal transport mechanisms in nanoscale are provided.

1.1 Ballistic-Diffusive Heat Transfer

Over the past two centuries, heat conduction in macroscale has been well understood by the traditional model for thermal diffusion. The conventional thermal conduction problems can be easily addressed and solved applying Fourier's law [23,24] assuming an infinite propagation speed for energy carriers. This model, though, becomes incapable once the domain is either subject to an oscillatory thermal disturbance at high frequency [25,26] resulting in a time scale shorter than the dominant thermal energy carriers' relaxation time; or its size is smaller than, or comparable to, the mean free path of the carriers [27,28]. In such cases, thermal energy transfers in a subcontinuum regime, which is a combination of ballistic and diffusive heat transfer, with phonons as the dominant thermal energy carriers. Different approaches are suggested for modeling thermal transport in the subcontinuum regime.

A promising approach for modeling heat transfer in small length and/or short time scales is using the equation of phonon radiative transport (EPRT) [29–31], derived from the Boltzmann transport equation (BTE) [32]. As a nonlinear integro-differential equation with a total of seven dimensions including 3 spatial coordinates, 3 wave vector coordinates, and time, phonon BTE is a notoriously complicated equation to solve. Yet many numerical

simulations are conducted to model subcontinuum thermal transport using EPRT adopting assumptions, such as the frequency-independent behavior of phonons, to simplify the problem. Some of these models are listed in Chapter 2 of this dissertation [33]. In addition, Mansoor et al. [34] solves the EPRT for curved thin films examining temperature disturbance at edges of the thin film. Meanwhile, Murthy's group introduced a coupled-ordinates method to improve the convergence time for solving phonon BTE for small Knudsen numbers, the ratio of mean-free path to the characteristic system length scale, where poor convergence is seen in sequential numerical solution methods [35]. Phonon BTE is also applied to predict phonon mean free path distribution [36], material thermal conductivity [37–39], and interfacial thermal resistance (Kapitza resistance) [40–42]. Mazumder's group performed large-scale parallel computations to solve phonon BTE for a three-dimensional silicon thin film with 400 phonon propagation directions in an angular domain and a total of ~9.7×10^9 unknowns (3 orders of magnitude larger than previous studies in this area), predicting thermal conductivity of Si with good agreement with previously reported measurements [43]. A software package for solving phonon BTE was introduced by Li et al. [44] to compute thermal conductivity of crystalline bulk materials and nanowires. In addition, an asymptotic approach was presented to derive an equation in a continuum regime from the phonon BTE and extend the validity range of Fourier's law, using Knudsen numbers in different orders [45]. The second chapter of this dissertation elaborates on governing equation of phonon BTE, discusses different solving techniques, and presents steady state and transient results for ballistic-diffusive thermal transport in two-dimensional domains.

1.2 Thermal Microcantilever

Thermal microcantilever is an SThM probe integrated with a resistive thermal heater/sensor capable of heating up to ~900ºC. Thermal analysis and manipulation of materials and structures at an extremely small scale provides the possibility of different applications in nanotechnology such as material characterization [46], mass spectrometry [47], thermophysical property measurement [48,49], and many more that are listed in Chapter 3 of this dissertation. Besides Joule heating of a microcantilever integrated with resistive heater, a microcantilever can be heated up using laser light to over 1500ºC [50]. Using laser heating, Rashcke's group [50] conducted thermal near-field spectroscopy on multiple samples. Sarid et al. [51] used an AFM to map thermal-conductivity features of a sample as a laser heated probe scans over it. Heat assisted magnetic recording [52], as the future of hard disk drive (HDD) technology, benefits from laser light by exciting surface plasmons in a gold near-field transducer [53,54], resulting in a temperature rise in recording media. Even though most of these applications require heating operation at a steady state, an oscillatory heating operation is required for precision measurements. A well-known technique is the 3ω method which has been widely used for thermal property measurement in solids [55], liquids [56], and gases [57,58]. This method is implemented to understand the frequency-dependent behavior of a thermal microcantilever under periodic operational conditions in air and vacuum, both experimentally and numerically. The third chapter of this dissertation elaborates on transient heat conduction equations in a frequency domain synced with electrical equations applying appropriate boundary conditions to model the behavior of a thermal microcantilever under periodic heating operations. As a result, thermal transfer functions at each operating frequency, and the ac temperature distribution

throughout the domain are presented.

1.3 Nanoscale Thermal Conduction and Extreme Near-Field Radiation

Fast growing tip-based thermal engineering applications have created strong demands on extensive analysis of point contact thermal transport between a tip and a substrate. During the past three decades, there has been unprecedented advances in applications using atomic force microscope (AFM) equipped with thermal microcantilevers with Joule-heating capability, or laser heated probes. The first has been widely used in scanning thermal microscopy (SThM) for nanoscale topography mapping [59–61], data storage [62–64], material characterization [65–68], and nanolithography [69,70]. The latter has been used for nanomachining [71], thermal near-field spectroscopy and imaging [50], and heat-assisted magnetic recording (HAMR) [72,73]. These applications have created strong demands on the fundamental understanding of nanoscale thermal transport between a sharp tip and a substrate. Many numerical studies as well as experimental investigations are reported to predict and measure tip-substrate heat transfer through solid-solid conduction [74–76], surrounding medium [77–79], and near-field radiative heat transfer [80,81]. Many more studies are listed in Chapter 4.

The fourth chapter of this dissertation introduces a new device that follows a four-point-probe scheme for resistive nanothermoemtry with a sensing probe smaller than its ancestors. The nanothermometer/heater is used to quantitatively study thermal transport between an AFM cantilever tip in contact with the nanoheater in an air environment. An extensive calculation is reported to distinguish contribution of each and every thermal transport mechanism (i.e., solid-solid conduction, air conduction, and near-field thermal

radiation). Even though the experiment reported in this chapter is conducted in an air environment, later in the dissertation a similar experiment is done in both air and vacuum environments that compliments the analysis in Chapter 4. The study in vacuum is reported in the conclusion chapter (Chapter 5) of this dissertation.

1.4 Overview of the Dissertation

This dissertation aims to address three main scopes, starting by introducing the theory behind phonon thermal transport in nanometer scale, continuing with an electrothermal characterization of a thermal microcantilever, the main player in tip-based thermal engineering, and ends with an investigation on thermal transport between a nanothermometer/heater and a sharp tip through solid-solid point contact.

Following this introductory chapter, Chapter 2 introduces a governing equation for modeling phonon heat transfer based on the Boltzmann transport equation (BTE) for a two-dimensional thin film in a subcontinuum regime. Discussing boundary conditions and various methods for solving this complicated equation, Chapter 2 applies a combination of finite element method (FEM) with discrete ordinate method (DOM) to discretize the medium in spatial and angular coordinates, respectively. Two different approaches are introduced to validate the simulation both in 1-D and 2-D, followed by contours of temperature distribution for different Knudsen numbers, indicating dependence of thermal transport on film thickness with respect to phonon mean free path. Finally, time dependent phonon BTE is solved and presented for different Knudsen numbers. This chapter is a reprint of a publication in the International Journal of Heat and Mass Transfer in 2014 titled "Finite Element Analysis of Transient Ballistic-Diffusive Phonon Heat Transport in Two-

Dimensional Domains."

Chapter 3 starts by introducing a variety of applications for thermal microcantilevers in tip-based thermal engineering and a literature review of previous characterization techniques, emphasizing the demands for ac characterization of this tool. Followed by scanning electron microscope (SEM) images of the device indicating details of the geometry, this chapter details the experimental set up and the electrical circuitry used to measure temperature oscillation at the heating area as a function of oscillation frequency of the heating power which depends on the third harmonic electric potential difference across the thermal microcantilever. After the experimental section, the finite element analysis including the governing equations to couple electrical and thermal equations along with boundary conditions is presented. Heat transfer equations are solved in frequency-domain to avoid large and expensive computations. Then the results are presented in terms of thermal transfer function at each operating frequency, and ac temperature contours throughout the thermal microcantilever for different heating frequencies starting as low as 90 Hz up to 34 kHz, both in air and vacuum. The effect of air on maximum temperature change is addressed and different scenarios in simulation are considered. Finally, the effect of thermal microcantilever geometry based on the size of heater and constriction region is studied, providing a design optimization tool depending on application interest. This chapter is a reprint of a publication in the Journal of Heat Transfer in 2016 titled "Electrothermal Thermal Characterization of Doped-Si Heated Microcantilevers Under Periodic Heating Operation."

Chapter 4 discusses thermal interactions between a sharp AFM microcantilever tip in contact with a nanothermometer/heater, starting with reviewing recent reports on tip-

substrate heat transfer analysis. Design, fabrication, and characterization of the new home-built four-point-probe resistive nanothermometer with a 250 nm × 350 nm sensing area is presented next. After showing that the device can be applied as a nanoheater, it is used to conduct a tip-induced cooling experiment, resulting in quantitative measurement of tip-substrate thermal transport and the temperature of the sensing area, used to calculate local thermal conductance. This experiment is done in air medium followed by additional calculation to theoretically distinguish effects of each heat transfer mechanism, and in particular conduction through solid-solid contact. The appendix reports on the results of the same experiment conducted in both air and vacuum conditions complementing the theory in Chapter 4. Finally, Chapter 5 covers the summary and conclusion of the aforementioned research followed by suggestions for future research.

1.5 References

[1] Stylios, G. K., Giannoudis, P. V., and Wan, T., 2005, "Applications of Nanotechnologies in Medical Practice," Injury, 36(SUPPL. 4), pp. 5–13.

[2] Raffa, V., Vittorio, O., Riggio, C., and Cuschieri, A., 2010, "Progress in Nanotechnology for Healthcare.," Minim. Invasive Ther. Allied Technol., 19(3), pp. 127–35.

[3] Sosnik, A., Cornier, J., Owen, A., Kwade, A., and Voorde, M. Van de, 2017, *Pharmaceutical Nanotechnology: Innovation and Production*, Wiley-VCH Verlag GmbH & Co. KGaA, Weinheim, Germany.

[4] Serrano, E., Rus, G., and García-Martínez, J., 2009, "Nanotechnology for Sustainable Energy," Renew. Sustain. Energy Rev., 13(9), pp. 2373–2384.

[5] Zang, L., 2011, *Energy Efficiency and Renewable Energy Through Nanotechnology*, Springer, New York.

[6] Wang, Z. L., and Wu, W., 2012, "Nanotechnology-Enabled Energy Harvesting for Self-Powered Micro-/Nanosystems," Angew. Chemie - Int. Ed., 51(47), pp. 11700–11721.

[7] Miyazaki, K., and Islam, N., 2007, "Nanotechnology Systems of Innovation-An Analysis of Industry and Academia Research Activities," Technovation, 27(11), pp. 661–675.

[8] Becker, S., 2013, "Nanotechnology in the Marketplace: How the Nanotechnology Industry Views Risk," J. Nanoparticle Res., 15, p. 1426.

[9] Ursyn, A., 2012, "NanoArt: Nanotechnology and Art," *Biologically-Inspired Computing for the Arts: Scientific Data through Graphics*, Information Science Reference, Hershey, PA, USA.

[10] Thomas, P., 2013, *Nanoart: The Immateriality of Art*, Intellect, Chicago, USA.

[11] Gabor, D., 1948, "A New Microscopic Principle.," Nature, 161(4098), pp. 777–778.

[12] Binnig, G., Rohrer, H., Gerber, C., and Weibel, E., 1982, "Surface Studies by Scanning Tunneling Microscopy," Phys. Rev. Lett., 49(1), pp. 57–61.

[13] Binnig, G., and Quate, C. F., 1986, "Atomic Force Microscope," Phys. Rev. Lett., 56(9), pp. 930–933.

[14] Williams, C. C., and Wickramasinghe, H. K., 1986, "Scanning Thermal Profiler," Microelectron. Eng., 5(1–4), pp. 509–513.

[15] Buratto, S. K., 1996, "Near-Field Scanning Optical Microscopy," Curr. Opin. Solid State Mater. Sci., 1, pp. 485–492.

[16] Huff, H. R., 2016, "(Invited) Transistors, Integrated Circuits and Nano-Technology: A Historical Review," ECS Trans., 72(4), pp. 275–287.

[17] Pop, E., 2010, "Energy Dissipation and Transport in Nanoscale Devices," Nano Res., 3, pp. 147–169.

[18] Yunus, C. A., and Afshin, J. G., 2011, *Heat and Mass Transfer: Fundamentals and Applications*, McGraw Hill Education, New York.

[19] Modest, M. F., 2013, *Radiative Heat Transfer*, Academic Press, Inc, Oxford, UK.

[20] Volz, S., 2007, *Microscale and Nanoscale Heat Transfer*, Springer-Verlag, Berlin Heidelberg.

[21] Shen, S., Narayanaswamy, A., and Chen, G., 2009, "Surface Phonon Polaritons Mediated Energy Transfer Between Nanoscale Gaps," Nano Lett., 9(8), pp. 2909–2913.

[22] Krüger, M., Emig, T., and Kardar, M., 2011, "Nonequilibrium Electromagnetic Fluctuations: Heat Transfer and Interactions," Phys. Rev. Lett., 106(21), p. 210404.

[23] Carson, J. E., 1963, "Analysis of Soil and Air Temperatures by Fourier Techniques," J. Geophys. Res., 68(8), pp. 2217–2232.

[24] Incropera, F. P., and De Witt, D. P., 1985, *Fundamentals of Heat and Mass Transfer*, John Wiley and Sons Inc, New York.

[25] Yuen, W. W., and Lee, S. C., 1989, "Non-Fourier Heat Conduction in a Semi-infinite Solid Subjected to Oscillatory Surface Thermal Disturbances," J. Heat Transf., 111(1), pp. 178–181.

[26] Tang, D. W., and Araki, N., 2000, "Non-Fourier Heat Condution Behavior in Finite Mediums Under Pulse Surface Heating," Mater. Sci. Eng. A, 292(2), pp. 173–178.

[27] Majumdar, A., 1993, "Microscale Heat Conduction in Dielectric Thin Films," J. Heat Transfer, 115, pp. 7–16.

[28] Tien, C. L., Majumdar, A., and Gerner, F., 1998, *Microscale Energy Transport*, Taylor and Francis, New York.

[29] Majumdar, A., 1993, "Microscale Heat Conduction in Dielectric Thin Films," J. Heat Transfer, 115, pp. 7–16.

[30] Joshi, A. A., and Majumdar, A., 1993, "Transient Ballistic and Diffusive Phonon Heat Transport in Thin Films," J. Appl. Phys., 74(1), p. 31.

[31] Prasher, R., 2003, "Generalized Equation of Phonon Radiative Transport," Appl. Phys. Lett., 83(1), pp. 48–50.

[32] Gurbin, H. L., Ferry, D. K., and Jocoboni, C., 1988, *The Physics of Submicron Semiconductor Devices*, Springer Science & Business Media, LLC, New York.

[33] Hamian, S., Yamada, T., Faghri, M., and Park, K., 2015, "Finite Element Analysis of Transient Ballistic–Diffusive Phonon Heat Transport in Two-Dimensional Domains," Int. J. Heat Mass Transf., 80, pp. 781–788.

[34] Mansoor, S. B., and Yilbas, B. S., 2016, "Phonon Transport Across Nano-Scale Curved Thin Films," Phys. B Condens. Matter, 503, pp. 130–140.

[35] Loy, J. M., Mathur, S. R., and Murthy, J. Y., 2015, "A Coupled Ordinates Method for Convergence Acceleration of the Phonon Boltzmann Transport Equation," J. Heat Transf., 137(1), p. 12402.

[36] Chiloyan, V., Zeng, L., Huberman, S., Maznev, A. A., Nelson, K. A., and Chen, G., 2016, "Variational Approach to Extracting the Phonon Mean Free Path Distribution from the Spectral Boltzmann Transport Equation," J. Appl. Phys., 120(2), pp. 1–5.

[37] McGaughey, A., and Kaviany, M., 2004, "Quantitative Validation of the Boltzmann Transport Equation Phonon Thermal Conductivity Model Under the Single-Mode Relaxation Time Approximation," Phys. Rev. B, 69(9), pp. 1–12.

[38] Romano, G., Esfarjani, K., Strubbe, D. A., Broido, D., and Kolpak, A. M., 2016, "Temperature-Dependent Thermal Conductivity in Silicon Nanostructured Materials Studied by the Boltzmann Transport Equation," Phys. Rev. B - Condens. Matter Mater. Phys., 93(3), pp. 1–7.

[39] Sobolev, S. L., 2017, "Discrete Space-Time Model for Heat Conduction: Application to Size-Dependent Thermal Conductivity in Nano-Films," Int. J. Heat Mass Transf., 108, pp. 933–939.

[40] Ali, S. A., and Mazumder, S., 2015, "Phonon Heat Conduction in Multidimensional Heterostructures: Predictions Using the Boltzmann Transport Equation," J. Heat Transf., 137(10), p. 102401.

[41] Ordonez-Miranda, J., Yang, R., Volz, S., and Alvarado-Gil, J. J., 2015, "Steady State and Modulated Heat Conduction in Layered Systems Predicted by the Analytical Solution of the Phonon Boltzmann Transport Equation," J. Appl. Phys., 118(7), p. 075103.

[42] Ali, H., and Yilbas, B. S., 2016, "Phonon Cross-Plane Transport and Thermal Boundary Resistance: Effect of Heat Source Size and Thermal Boundary Resistance on Phonon Characteristics," Contin. Mech. Thermodyn., 28, p. 1373.

[43] Ali, S. A., Kollu, G., Mazumder, S., Sadayappan, P., and Mittal, A., 2014, "Large-

Scale Parallel Computation of the Phonon Boltzmann Transport Equation," Int. J. Therm. Sci., 86, pp. 341–351.

[44] Li, W., Carrete, J., Katcho, N. A., and Mingo, N., 2014, "ShengBTE: A Solver of the Boltzmann Transport Equation for Phonons," Comput. Phys. Commun., 185(6), pp. 1747–1758.

[45] Peraud, J. P. M., and Hadjiconstantinou, N. G., 2016, "Extending the Range of Validity of Fourier's Law into the Kinetic Transport Regime via Asymptotic Solution of the Phonon Boltzmann Transport Equation," Phys. Rev. B - Condens. Matter Mater. Phys., 93(4), p. 045424.

[46] Duvigneau, J., Schönherr, H., and Vancso, G. J., 2010, "Nanoscale Thermal AFM of Polymers: Transient Heat Flow Effects," ACS Nano, 4(11), pp. 6932–6940.

[47] Ovchinnikova, O. S., Kjoller, K., Hurst, G. B., Pelletier, D. A., and Van Berkel, G. J., 2014, "Atomic Force Microscope Controlled Topographical Imaging and Proximal Probe Thermal Desorption/Ionization Mass Spectrometry Imaging," Anal. Chem., 86(2), pp. 1083–1090.

[48] Varandani, D., Agarwal, K., Brugger, J., and Mehta, B. R., 2016, "Scanning Thermal Probe Microscope Method for the Determination of Thermal Diffusivity of Nanocomposite Thin Films," Rev. Sci. Instrum., 87(8), p. 84903.

[49] Pereira, M. J., Amaral, J. S., Silva, N. J. O., and Amaral, V. S., 2016, "Nano-Localized Thermal Analysis and Mapping of Surface and Sub-Surface Thermal Properties Using Scanning Thermal Microscopy (SThM)," Microsc. Microanal., 22(6), pp. 1270–1280.

[50] O'Callahan, B. T., and Raschke, M. B., 2017, "Laser Heating of Scanning Probe Tips for Thermal Near-Field Spectroscopy and Imaging," APL Photonics, 2(2), p. 21301.

[51] Sarid, D., McCarthy, B., and Grover, R., 2006, "Scanning Thermal-Conductivity Microscope," Rev. Sci. Instrum., 77(2), p. 023703.

[52] Pan, L., and Bogy, D. B., 2009, "Data Storage: Heat-Assisted Magnetic Recording," Nat. Photonics, 3(4), pp. 189–190.

[53] Zhou, N., Xu, X., Hammack, A. T., Stipe, B. C., Gao, K., Scholz, W., and Gage, E. C., 2014, "Plasmonic Near-Field Transducer for Heat-Assisted Magnetic Recording," Nanophotonics, 3(3), pp. 141–155.

[54] Scheunert, G., Cohen, S., Kullock, R., Mccarron, R., Dawson, P., and Oron, D., 2017, "Grazing-Incidence Optical Magnetic Recording with Super-Resolution," Beilstein J. Nanotechnol., 8, pp. 28–37.

[55] Hu, X. J., Padilla, A. A., Xu, J., Fisher, T. S., and Goodson, K. E., 2005, "3-Omega

Measurements of Vertically Oriented Carbon Nanotubes on Silicon," J. Heat Transfer, 128(11), pp. 1109–1113.

[56] Park, B. K., Park, J., and Kim, D., 2010, "Note: Three-Omega Method to Measure Thermal Properties of Subnanoliter Liquid Samples," Rev. Sci. Instrum., 81(6), pp. 6–9.

[57] Yusibani, E., Woodfield, P. L., Kohno, M., Shinzato, K., Takata, Y., and Fujii, M., 2009, "End Effects in the Three-Omega Method to Measure Gas Thermal Conductivity," Int. J. Thermophys., 30(3), pp. 833–850.

[58] Schiffres, S. N., and Malen, J. A., 2011, "Improved 3-Omega Measurement of Thermal Conductivity in Liquid, Gases, and Powders Using a Metal-Coated Optical Fiber.," Rev. Sci. Instrum., 82(6), p. 64903.

[59] Majumdar, A., Carrejo, J. P., and Lai, J., 1993, "Thermal Imaging Using the Atomic Force Microscope," Appl. Phys. Lett., 62(1993), pp. 2501–2503.

[60] Somnath, S., Corbin, E. A., and King, W. P., 2011, "Improved Nanotopography Sensing via Temperature Control of a Heated Atomic Force Microscope Cantilever," IEEE Sens. J., 11(11), pp. 2664–2670.

[61] Lee, B., Somnath, S., and King, W. P., 2013, "Fast Nanotopography Imaging Using a High Speed Cantilever with Integrated Heater-Thermometer.," Nanotechnology, 24, p. 135501.

[62] Binnig, G., Despont, M., Drechsler, U., Häberle, W., Lutwyche, M., Vettiger, P., Mamin, H. J., Chui, B. W., and Kenny, T. W., 1999, "Ultrahigh-Density Atomic Force Microscopy Data Storage with Erase Capability," Appl. Phys. Lett., 74(9), p. 1329.

[63] King, W. P., Kenny, T. W., Goodson, K. E., Cross, G., Despont, M., Dürig, U., Rothuizen, H., Binnig, G. K., and Vettiger, P., 2001, "Atomic Force Microscope Cantilevers for Combined Thermomechanical Data Writing and Reading," Appl. Phys. Lett., 78(9), p. 1300.

[64] Lee, D. W., Ono, T., Abe, T., and Esashi, M., 2002, "Microprobe Array with Electrical Interconnection for Thermal Imaging and Data Storage," J. Microelectromechanical Syst., 11(3), pp. 215–221.

[65] Reading, M., Price, D. M., Grandy, D. B., Smith, R. M., Bozec, L., Conroy, M., Hammiche, A., and Pollock, H. M., 2001, "Micro-Thermal Analysis of Polymers: Current Capabilities and Future Prospects," Macromol. Symp., 167, pp. 45–62.

[66] Bond, L., Allen, S., Davies, M. C., Roberts, C. J., Shivji, A. P., Tendler, S. J. B., Williams, P. M., and Zhang, J., 2002, "Differential Scanning Calorimetry and Scanning Thermal Microscopy Analysis of Pharmaceutical Materials," Int. J. Pharm., 243, pp. 71–82.

[67] Hinz, M., Marti, O., Gotsmann, B., Lantz, M., and Durig, O., 2008, "High Resolution Vacuum Scanning Thermal Microscopy of HfO2 and SiO2," Appl. Phys. Lett., 92, p. 43122.

[68] Xu, D., Zhang, Y., Zhou, H., Meng, Y., and Wang, S., 2016, "Characterization of Adhesive Penetration in Wood Bond by Means of Scanning Thermal Microscopy (SThM)," Int. J. Biol. Chem. Physics, Technol. Wood, 70(4), pp. 323–330.

[69] Milner, A. A., Zhang, K., and Prior, Y., 2008, "Floating Tip Nanolithography.," Nano Lett., 8(7), pp. 2017–22.

[70] Knoll, A. W., Pires, D., Coulembier, O., Dubois, P., Hedrick, J. L., Frommer, J., and Duerig, U., 2010, "Probe-Based 3-D Nanolithography Using Self-Amplified Depolymerization Polymers," Adv. Mater., 22, pp. 3361–3365.

[71] Chimmalgi, A., Choi, T. Y., Grigoropoulos, C. P., and Komvopoulos, K., 2003, "Femtosecond Laser Aperturless Near-Field Nanomachining of Metals Assisted by Scanning Probe Microscopy," Appl. Phys. Lett., 82(8), pp. 1146–1148.

[72] Mark H. Kryder, Edward C. Gage, Terry W. McDaniel, William A. Challener, Robert E. Rottmayer, Ganping Ju, Yiao-Tee Hsia, and M. F. E., 2008, "Heat Assisted Magnetic Recording," Springer Proc. Phys., 96(11), pp. 1810–1835.

[73] Challener, W. A., Peng, C., Itagi, A. V., Karns, D., Peng, W., Peng, Y., Yang, X., Zhu, X., Gokemeijer, N. J., Hsia, Y.-T., Ju, G., Rottmayer, R. E., Seigler, M. A., and Gage, E. C., 2009, "Heat-Assisted Magnetic Recording by a Near-Field Transducer with Efficient Optical Energy Transfer," Nat. Photonics, 3(5), pp. 303–303.

[74] Singh, D., Murthy, J. Y., and Fisher, T. S., 2011, "Phonon Transport Across Mesoscopic Constrictions," J. Heat Transfer, 133(4), p. 42402.

[75] Pettes, M. T., and Shi, L., 2013, "A Reexamination of Phonon Transport Through a Nanoscale Point Contact in Vacuum," J. Heat Transfer, 136(3), p. 32401.

[76] Ge, Y., Zhang, Y., Booth, J. A., Weaver, J. M. R., and Dobson, P. S., 2016, "Quantification of Probe–Sample Interactions of a Scanning Thermal Microscope Using a Nanofabricated Calibration Sample Having Programmable Size," Nanotechnology, 27, p. 325503.

[77] Majumdar, A., 1999, "Scanning Thermal Microscopy," Annu. Rev. Mater. Sci., 29(1), pp. 505–585.

[78] Shi, L., and Majumdar, A., 2002, "Thermal Transport Mechanisms at Nanoscale Point Contacts," J. Heat Transfer, 124(2), pp. 239–337.

[79] Park, K., Cross, G. L. W., Zhang, Z. M., and King, W. P., 2008, "Experimental Investigation on the Heat Transfer Between a Heated Microcantilever and a Substrate," J. Heat Transfer, 130(10), p. 102401.

[80] Kim, K., Song, B., Fernández-Hurtado, V., Lee, W., Jeong, W., Cui, L., Thompson, D., Feist, J., Reid, M. T. H., García-Vidal, F. J., Cuevas, J. C., Meyhofer, E., and Reddy, P., 2015, "Radiative Heat Transfer in the Extreme Near Field," Nature, 528, pp. 387–391.

[81] Edalatpour, S., and Francoeur, M., 2016, "Near-Field Radiative Heat Transfer Between Arbitrarily Shaped Objects and a Surface," Phys. Rev. B - Condens. Matter Mater. Phys., 94(4), pp. 1–11.

CHAPTER 2

FINITE ELEMENT ANALYSIS OF TRANSIENT BALLISTIC-DIFFUSIVE PHONON HEAT TRANSPORT IN TWO-DIMENSIONAL DOMAINS

Reproduced from International Journal of Heat and Mass Transfer (2015) **80**, 781–788. Finite Element Analysis of Transient Ballistic–Diffusive Phonon Heat Transport in Two-Dimensional Domains. Sina Hamian, Toru Yamada, Mohammad Faghri, Keunhan Park, © Owned by the authors, published by ELSEVIER, 2015, with the permission of the International Journal of Heat and Mass Transfer (IJHMT).

2.1 Abstract

While sub-continuum heat conduction becomes more important as the size of micro/nanodevices keeps shrinking under the mean free path of heat carriers, its computation still remains challenging to the general engineering community due to the lack of easily accessible numerical simulation tools. To address this challenge, this article reports the finite element analysis (FEA) of transient ballistic-diffusive phonon heat transport in a two-dimensional domain using a commercial package (COMSOL Multiphysics). The Boltzmann transport equation under the gray relaxation-time approximation was numerically solved by discretizing the angular domain with the discrete ordinate method (DOM) and the spatial domain with the FEA. The DOM-FEA method was

validated by comparing the results with different benchmark studies, such as the equation of phonon radiative transfer, the ballistic-diffusive equation, and the finite difference method of the phonon Boltzmann transport equation. The calculation of phonon heat transport for a 2-D square slab reveals that heat conduction becomes more ballistic with temperature jumps at boundaries as Knudsen number (Kn) increases. The ballistic nature also significantly affects transient thermal behaviors at high Kn numbers. The obtained results clearly demonstrate the capability of the DOM-FEA as a promising engineering tool for calculating sub-continuum phonon heat transport.

2.2 Introduction

For the last two centuries, the conventional Fourier heat conduction equation has been used for modeling a diffusive nature of macroscale heat conduction by considering the energy conservation and Fourier's linear approximation of heat flux. However, it cannot accurately predict heat transport when the length scale is comparable to or smaller than the mean free path of thermal energy carriers or when the time scale is shorter than the carrier relaxation time [1–4]. When considering phonons as the dominant energy carrier of heat conduction, the Boltzmann transport equation (BTE) for phonons, or equivalently the equation of phonon radiative transport (EPRT), has been implemented to predict phonon heat transport in the sub-continuum space and time domains [5,6]. Majumdar's group [7,8] was the first who derived the EPRT from the BTE and proved its analogy with the radiative transport equation (RTE). By calculating the temperature profile and heat flux in a thin film from the one-dimensional (1-D) EPRT, they showed that the EPRT can describe a ballistic feature of phonon heat transport for the sub-continuum spatial and time scales.

The EPRT has been also used to calculate the thermal boundary resistance across the interface of a thin film on a substrate [9], across interfaces of superlattices [10], and across mesoscopic constrictions at cylinder-substrate and sphere-substrate interfaces [11]. Narumanchi *et al.* [12] solved the transient two-dimensional (2-D) BTE under the gray relaxation-time approximation to study the effect of an unsteady, localized hot spot to phonon heat transport. In the following work, they considered frequency-dependent interactions between transverse and longitudinal acoustic phonons and optical phonons to incorporate more realistic phonon dispersion relations in silicon thin films [13]. The transient 1-D BTE with frequency- and polarization-dependence was also solved in Ref. [14] to better understand how phonon mean free paths can be extracted from the transient thermoreflectance experiment.

It should be noted that the BTE is inherently difficult to solve, particularly when the full physics of phonon dispersion and scattering is to be considered, due to its integro-differential formulation. However, the analogy between the phonon BTE (or EPRT) and the RTE has allowed the extension of several numerical schemes originally developed to solve the RTE to the computation of the phonon BTE [5]. Such methods include the finite volume method (FVM) [11–13,15–17], the finite element analysis (FEA) [18–20], and the finite difference method (FDM) [7,8,14,21], combined with the discrete ordinate method (DOM) for angular discretization. In addition, the ballistic-diffusive approximation of the BTE has been introduced to alleviate computational complexities in directly solving the BTE while conveying the ballistic-diffusive features of phonon heat transport [21–24]. The advancement of computing power has also allowed the implementation of computation-intensive numerical methods, such as the molecular dynamics (MD) [25,26], Monte Carlo

simulation [27–30] and the lattice Boltzmann method [31–33]. Recently, Yamada *et al.* [34] applied the dissipative particle dynamics with energy conversion, a coarse-grained MD simulation, to simulate heat conduction in a thin film with a less computational cost than the MD.

Although significant advances have been made in computing sub-continuum heat transfer, most of the aforementioned numerical approaches are not readily accessible to the general engineering community. It often requires too much time and effort to develop a home-built code, preventing the routine computation of sub-continuum phonon heat transport for the reliable design of micro/nanodevices and their performance evaluations. To overcome this challenge, the present study implements a commercial FEA package, COMSOL Multiphysics, to numerically solve the 2-D transient BTE. Although the COMSOL package has been used to compute the BTE [19,20], their works have been restricted to 1-D thin films. Since the BTE has a directional dependence, the DOM was combined to discretize the BTE in the angular direction [21]. The details of the numerical scheme are described in the consecutive section. In the results and discussion, the DOM-FEA is verified by comparing the numerically obtained temperature distribution along the centerline of a long rectangular domain with the semi-analytical solution of the 1-D EPRT [2]. The obtained results for 2-D geometry are also compared with DOM-FDM and ballistic diffusive equations (BDE) results from Ref. [21]. We also discuss steady and transient temperature distributions and related heat fluxes in a 2-D square slab for a wide range of Knudsen numbers, when an illustrative boundary condition has a hot temperature on the top surface while the other surfaces remain at a cold temperature.

2.3 Computation Model

It is well known that phonons follow the Bose-Einstein statistics and interact with other phonons, electrons, and defects via scattering processes. Since BTE can model the statistical distribution of particle interactions via short-range forces, it is a valid and useful tool for studying classical size effects on phonon transport. In general, the BTE is a complicated nonlinear integro-differential equation and can be simplified with the gray relaxation-time approximation [5]:

$$\frac{\partial f}{\partial t} + \mathbf{v}_g \cdot \nabla f = \frac{f_0 - f}{\tau} \tag{2.1}$$

where f is the frequency-dependent distribution function of phonons, v_g is the averaged phonon group velocity, f_0 is the equilibrium distribution function, and τ is the effective relaxation time due to all phonon-scattering processes. The equilibrium distribution function of phonons follows the Bose-Einstein distribution, $f_0 = 1/[\exp(\hbar\omega / k_B T) - 1]$, where $\hbar$ is the reduced Planck constant, ω is the angular frequency, k_B is the Boltzmann constant, and T is temperature. It should be noted that the right-hand side of the equation denotes gray phonon-scattering with a single phonon velocity v_g in all directions and a single phonon relaxation time τ. Despite its simple form, the gray relaxation time approximation has proven to provide insight on phonon transport behaviors with an acceptable accuracy [11,13]. The BTE can be formulated with the phonon energy density as [5,35]

$$\frac{\partial e''}{\partial t} + \nabla \cdot (v_g \hat{\mathbf{s}} e'') = \frac{e_0'' - e''}{\tau} + \dot{q}_{vol} \tag{2.2}$$

The directional phonon energy density at position $\mathbf{r}$ and in direction $\hat{\mathbf{s}}$ (J/m^3-sr) is defined as

$$e''(\mathbf{r}, \hat{\mathbf{s}}, t) = \sum_p \left(\int_0^{\omega_D} D_p(\omega) f \hbar \omega d\omega \right) \tag{2.3}$$

where $D_p(\omega)$ is the phonon density of state, ω_D is the Debye cutoff frequency, and the subscript p is the phonon polarization. The generation term $\dot{q}_{vol}$ represents the phonon source term due to electron-phonon scattering [21]. The directional phonon energy density at equilibrium, e_0'', can be determined from the following equation:

$$e_0''(\mathbf{r}, t) = \frac{1}{4\pi} \int_{4\pi} e''(\mathbf{r}, \hat{\mathbf{s}}, t) d\Omega \tag{2.4}$$

where $d\Omega$ is incremental solid angle. Once the equilibrium directional energy density is determined, the temperature field can be obtained from $T(\mathbf{r}, t) = 4\pi e_0''(\mathbf{r}, t) / C$, where C is the volumetric heat capacity and assumed to be constant due to small temperature difference in the domain. In addition, the heat flux can also be obtained from the phonon energy density [13]:

$$\mathbf{q}''(\mathbf{r}, t) = \int_{4\pi} e''(\mathbf{r}, \hat{\mathbf{s}}, t) v_g \hat{\mathbf{s}} d\Omega \tag{2.5}$$

In order to numerically solve the BTE for the 2-D domain illustrated in Fig. 2.1, we combined the finite element analysis (FEA) and the discrete ordinate method (DOM) in the present study. Since the phonon energy density is directionally dependent, Eq. (2.2) should be discretized in both the spatial and angular domains. While the spatial domain is discretized in the FEA, the angular domain at any location is discretized into non-overlapping polar and azimuthal angles with the DOM. Since a weighting scheme in the DOM considerably affects the accuracy of the integration [36], the present study implemented the Gaussian quadrature distribution for all phonon propagation directions in the 3-D space [14,20]. The maximum number of angular discretization was 32 directions for polar ($0 \le \theta \le \pi$) and 8 directions for azimuthal angles ($0 \le \varphi \le \pi$; not $0 \le \varphi \le 2\pi$ due to symmetry), or 32×8 (256) directions for simplicity, while coarse discretization cases were also simulated to investigate the effect of angular discretization to the computation accuracy.

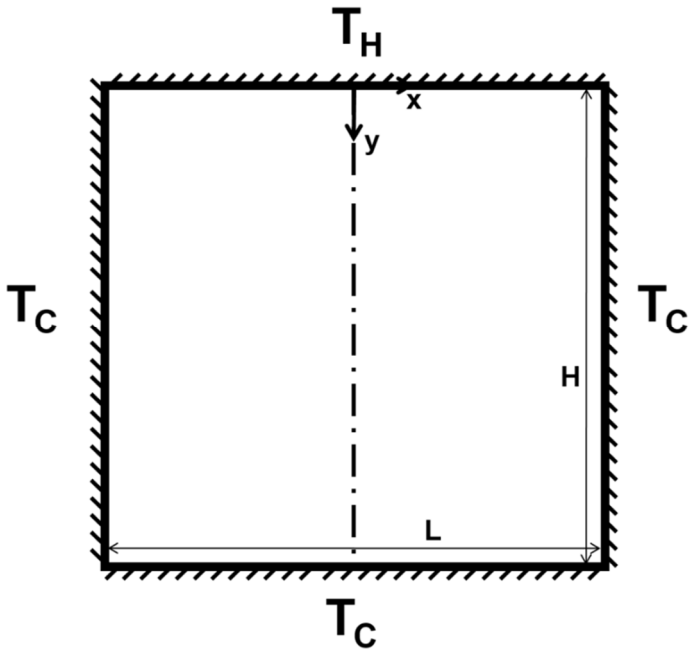

Figure 2.1. Schematic of the boundary conditions of 2D heat conduction simulation

Under the assumption of no heat generation (i.e., $\dot{q}_{vol} = 0$), Eq. (2.2) can be written as the angularly discretized and normalized form in the 2-D domain:

$$\frac{\partial e''_{n,m}}{\partial t^*} + Kn\left[\mu_n \frac{\partial e''_{n,m}}{\partial x^*} + \eta_{n,m} \frac{\partial e''_{n,m}}{\partial y^*}\right] = e''_0 - e''_{n,m} \tag{2.6}$$

where $t^* = t/\tau$, $x^* = x/\min(L,H)$, and $y^* = y/\min(L,H)$. The polar angle θ and azimuthal angle φ are discretized and normalized to yield $\mu_n = \cos\theta_n$ and $\eta_{n,m} = \sin\theta_n \cos\varphi_m$. The Knudsen number (Kn) is defined as $\mathrm{Kn} = \Lambda/\min(L,H)$, where $\Lambda = v_g\tau$ is the effective phonon mean free path. The phonon energy density at equilibrium, Eq. (2.4), can then be expressed as

$$e''_0(t^*, x^*, y^*) = \frac{2}{4\pi}\sum_n \sum_m e''_{n,m}(t^*, x^*, y^*) w_n w'_m \tag{2.7}$$

where w_n and w'_m are weighting factors that satisfy $\sum_n \sum_m w_n w'_m = 2\pi$ [21]. The factor 2 in the numerator is due to the symmetry in the azimuthal angle. Accordingly, the temperature field can be expressed as

$$T(t^*, x^*, y^*) = \frac{4\pi e''_0(t^*, x^*, y^*)}{C} = \frac{2}{C}\sum_n \sum_m e''_{n,m}(t^*, x^*, y^*) w_n w'_m \tag{2.8}$$

and the heat flux in *x*- and *y*- directions as

$$q_x''(t^*, x^*, y^*) = 2v_g \sum_n \sum_m e''_{n,m}(t^*, x^*, y^*)\mu_n w_n w'_m$$
$$q_y''(t^*, x^*, y^*) = 2v_g \sum_n \sum_m e''_{n,m}(t^*, x^*, y^*)\eta_{n,m} w_n w'_m \tag{2.9}$$

The boundary conditions employed in the present study are the thermalizing boundary conditions with fixed temperatures at all boundaries. As shown in Fig. 2.1, the temperature at the top side of the square domain is kept constant at T_H while all the other three sides are T_C ($T_H > T_C$). For the thermalizing boundary condition, the phonon energy density entering the domain from the boundary ($\hat{\mathbf{s}} \cdot \hat{\mathbf{n}} \le 0$, where $\hat{\mathbf{n}}$ is an outward-pointing normal vector from the domain) should satisfy

$$e''(\mathbf{r}_b, \mathbf{s}) = e_0''(\mathbf{r}_b) = \frac{CT_b}{4\pi} \tag{2.10}$$

where T_b is the temperature at the boundary position, $\mathbf{r}_b$. Although the present study focuses on the fixed temperature boundary condition, the diffusely reflecting boundary condition can be applied using $e''(\mathbf{r}_b, \mathbf{s}) = \frac{1}{\pi}\int_{\hat{\mathbf{s}}\cdot\hat{\mathbf{n}}>0} e''\hat{\mathbf{s}} \cdot \hat{\mathbf{n}}\, d\Omega$ for all the phonon propagation directions entering the domain ($\hat{\mathbf{s}} \cdot \hat{\mathbf{n}} \le 0$). The specularly reflecting boundary condition can be expressed as $e''(\mathbf{r}_b, \mathbf{s}) = e''(\mathbf{r}_b, \mathbf{s}_\mathbf{r})$ for all directions incoming to the domain ($\hat{\mathbf{s}} \cdot \hat{\mathbf{n}} \le 0$), where $\hat{\mathbf{s}}_\mathbf{r}$ is the specular direction corresponding to $\hat{\mathbf{s}}$: $\hat{\mathbf{s}}_\mathbf{r} = \hat{\mathbf{s}} - 2(\hat{\mathbf{s}} \cdot \hat{\mathbf{n}})\hat{\mathbf{n}}$ [11,12].

The algorithm for solving the BTE can be summarized as follows: with the initial guess of the equilibrium directional phonon energy density e_0'', Eq. (2.6) is solved to obtain the directional phonon energy density at each phonon propagation direction, $e''_{n,m}$. After

obtaining the phonon energy densities for all solid angles, e_0'' is updated using Eq. (2.7). The computation of the phonon energy density is iterated until the convergence occurs for e'' and e_0''. After the computation of e'', the temperature field and heat flux can be obtained using Eqs. (2.8) and (2.9), respectively. For the numerical simulation, we ran a COMSOL Multiphysics 4.3b commercial package with a computing server (20 cores of 2.4 GHz Intel processor with 256GB RAM), provided by the Center of High Performance Computing (CHPC) at the University of Utah. The BTE was solved for various Knudsen numbers ranging from 0.03 to 10. All computations for the geometry were conducted with 578 triangular meshes. In fact, the mesh refinement beyond 578 meshes did not improve the accuracy of the solution; when the computation results were compared between 578 meshes and 928 meshes, the difference was only in the order of 1×10^{-8}. The calculation of the steady 2-D BTE for 578 mesh elements and 32×8 angular directions using the above computer configuration took around 50 minutes.

2.4 Results and Discussion

In order to validate the DOM-FEA scheme, the 2-D BTE has been solved for a rectangular domain with a high aspect ratio ($L/H = 10$) and compared with the 1-D solution of the EPRT. The boundary condition was set to have T_H and T_C on the top and bottom surfaces, respectively, while the side walls are adiabatic (i.e., the diffusely reflecting boundary condition). The 1-D solution of the EPRT is expressed with a closed form as [2,7]

$$e_0^*(x^*) = \frac{1}{2}\left[E_2(x^*) + \int_0^{\xi} e_0^*(\kappa) E_1(|\, x^* - \kappa \,|) d\kappa \right] \tag{2.11}$$

where e_0^* is the phonon emissive power normalized with that at the wall, ξ is the acoustic thickness, and $E_n(x) = \int_0^1 \alpha^{n-2} \exp(-x/\alpha) d\alpha$ is the exponential integral. Fig. 2.2(a) shows the steady-state temperature distributions along the centerline of the rectangular domain for different Knudsen numbers. The temperature is normalized with $\Theta = (T - T_C)/(T_H - T_C)$. When compared with the 1-D solution of the EPRT, the DOM-FEA solutions are in excellent agreement with the EPRT solutions: the deviations are 0.18% for Kn = 0.1 and 0.62 % for Kn = 10, respectively. We believe that the small deviation may be due to the truncation error in the angular discretization (32×8) and the side wall effects of the 2-D domain. At low Kn cases, thermal behaviors are diffusive with the almost linear temperature distributions with no temperature jump at the boundaries. However, as Kn increases, the ballistic nature of phonon heat transfer is manifested by a uniform temperature distribution and the temperature jump at the boundaries [2]. At the acoustically thin limit at Kn = 10, phonons can travel directly from one end to the other with almost no scattering.

Another validation results of the DOM-FEA are shown in Fig. 2.2(b), where the FEA results are compared with the FDM results of the BTE and the ballistic-diffusive approximation published in Ref. [21]. The considered geometry is a 2-D rectangular domain with the aspect ratio of $L/H = 2$, where the center portion of the top wall is maintained at T_H while all the other boundaries remain at T_C: the schematics of the geometry is illustrated in the inset. To ease the comparison, the Knudsen number is defined

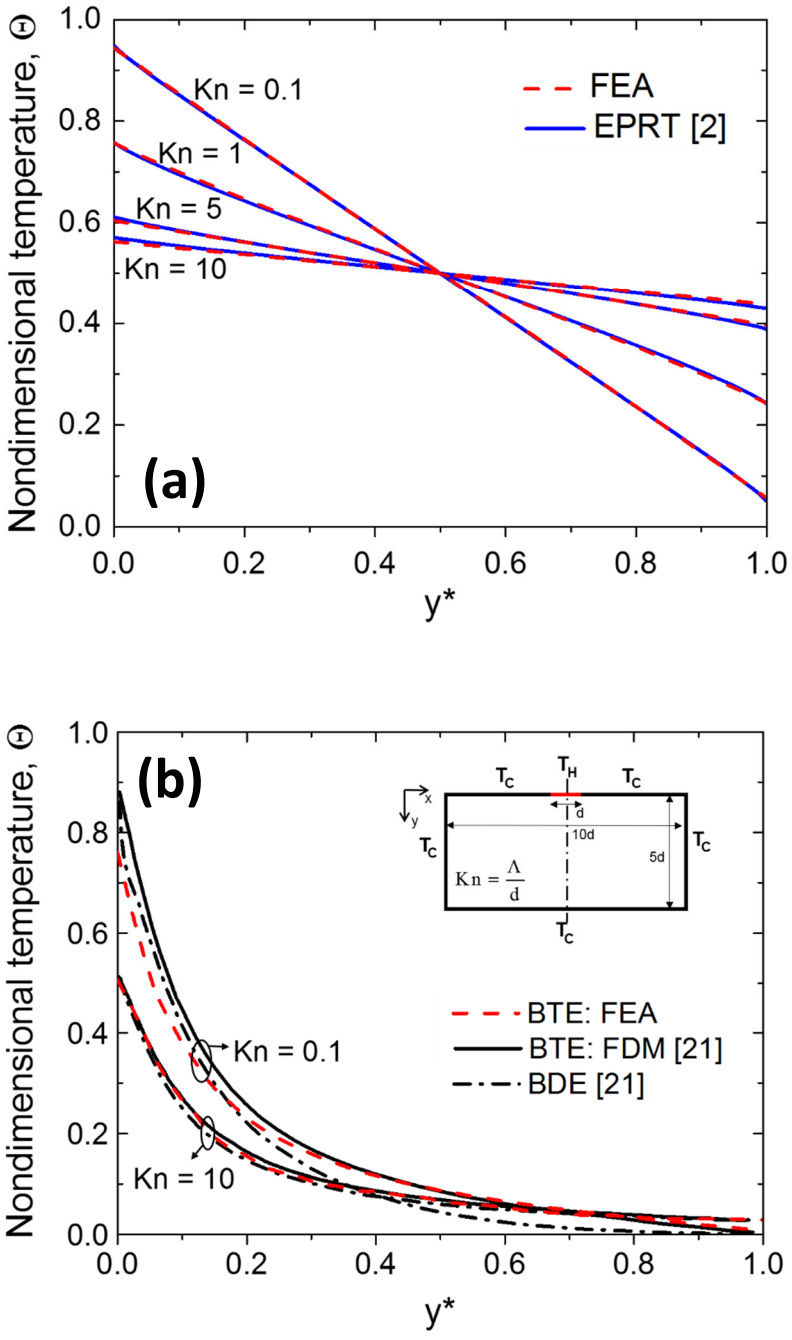

Figure 2.2. (a) Nondimensional temperature distribution along its center line of the rectangular domain with a high aspect ratio. Temperature distribution is normalized using the hot and cold boundaries, i.e., $\Theta = (T - T_C)/(T_H - T_C)$. To validate the model, the computation results are compared with the semi-analytical solution of the 1-D equation of phonon radiative transfer (EPRT) [2]. (b) Temperature distribution along the centerline of the rectangular domain illustrated in the inset. Results are compared with BTE-FDM and BDE from Ref. [21] for further validation.

as the ratio of phonon mean free path to the length of the hot wall (i.e., $\mathrm{Kn} \equiv \Lambda / d$) following Ref. [21], and only the steady-state temperature distributions along the centerline are plotted. All three computation results show a good agreement for both Kn numbers, Kn = 0.1 and Kn = 10, while the agreement is much better at Kn = 10. At Kn = 0.1, the FEA slightly underestimates the temperature near the hot wall compared to the other two, while the ballistic-diffusive approximation predicts a lower temperature distribution than the FEA and FDM results near the bottom wall. As mentioned in Ref. [21], such deviations between different numerical solutions for Kn = 0.1 are likely due to the subtle difference in applying boundary conditions. These results clearly demonstrate that the FEA

Fig. 2.3(a) shows the effect of the Knudsen number on the temperature distribution of the square domain. The BTE was solved for Kn = 0.03, 0.3, 1, and 10 with a 32×8 angular discretization, and the spatial domain was discretized with 578 triangular meshes for the space and 60 elements for boundaries. The temperature distribution at Kn = 0.03 is almost identical to the Fourier temperature distribution except a small temperature jump at the hot surface, indicating that heat is transferred almost diffusively as a result of strong phonon-scattering. This result suggests that heat conduction should become fully diffusive when the device size is several ten times bigger than the effective phonon mean free path. For instance, silicon-based microdevices should have a characteristic length at least in the order of 10 μm to safely use the Fourier conduction equation for heat transfer analysis, as the effective mean free path of silicon is 260.4 nm at room temperature [9,10]. As Kn increases, higher temperature jumps at boundaries are observed. Moreover, the temperature jump is greater at the hot surface than the cold surface, suggesting that hot phonons emitted from the top surface be more ballistically transferred before colliding with cold phonons near

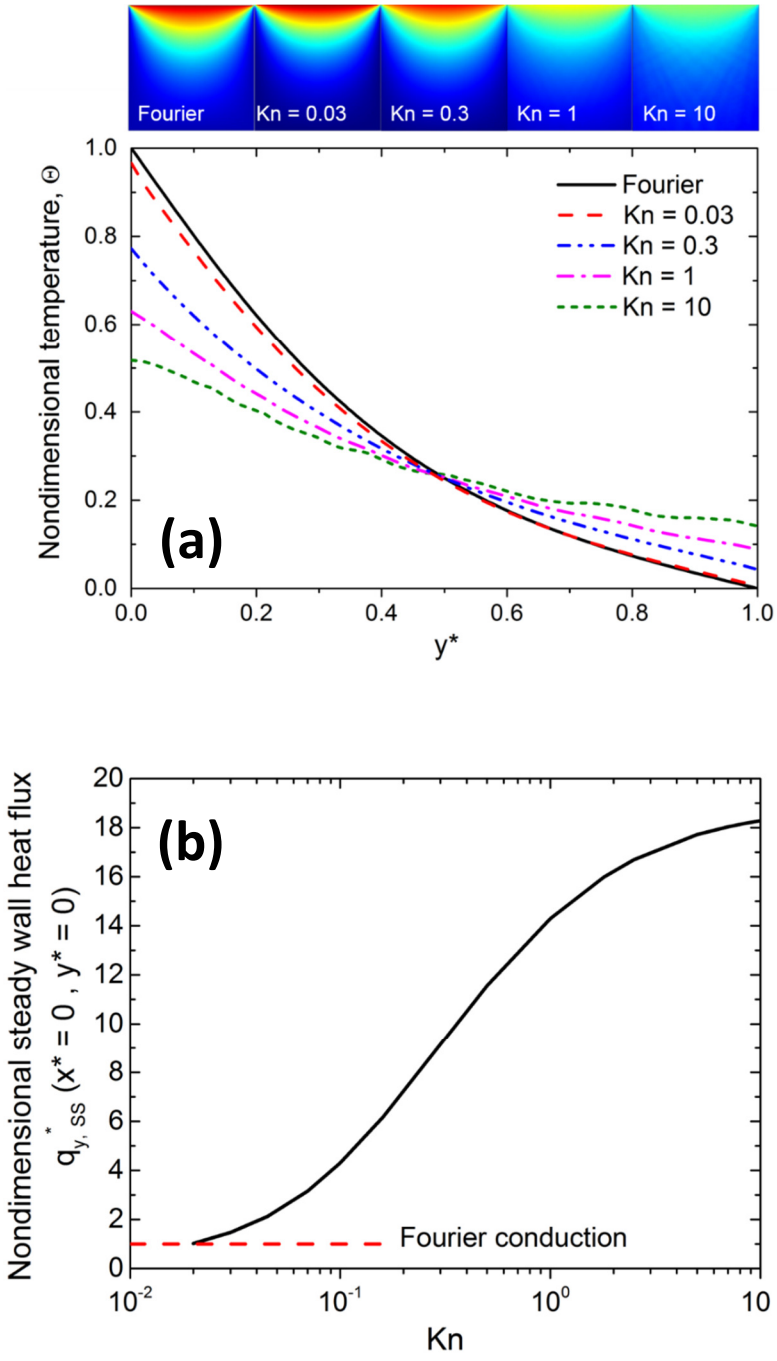

Figure 2.3. (a) Nondimensional temperature distribution predicted with the BTE for different Kn numbers. For comparison, nondimensional temperature distribution predicted with the Fourier heat conduction equation is also plotted. (b) Nondimensional steady-state heat flux in the y-direction at the center of the top wall ($x^*=0, y^*=0$). Heat flux is normalized with the conventional Fourier's law at the steady state, i.e., $q^*_{y,SS} = q''_{y,SS} / q''_{y,SS,Fourier}$, indicating that $q^*_{y,SS}$ becomes unity when the heat conduction is fully diffusive.

the other surfaces at T_C. Another interesting observation is that phonon heat transport becomes more ballistic as Kn increases over unity. This trend can be further confirmed in Fig. 2.3(b), which shows the steady heat flux at the center of the top wall (i.e., $x^* = 0, y^* = 0$). The heat flux is normalized with the steady heat flux at the same position calculated from the Fourier heat conduction equation, i.e., $q^*_{y,SS} = q''_{y,SS} / q''_{y,SS,Fourier}$. This normalization yields $q^*_{y,SS} = 1$ when heat conduction is fully diffusive. For direct comparison between the BTE and the Fourier results, silicon (Si) was selected as a domain material, having $C = 930\,\text{kJ/m}^3\text{-K}$, $\Lambda = 260.4$ nm and $v_g = 1804$ m/s [9]. The thermal conductivity was determined from the kinetic theory, $k = Cv_g\Lambda / 3$, to yield 145 W/m-K. In addition, the domain size for the computation of the Fourier heat conduction equation was assumed to be 100 times the phonon mean free path, i.e., Kn = 0.01. In Fig. 2.3(b), nondimensional heat flux approaches unity for small Kn numbers, representing the diffusive nature of heat flux. This value increases up to ~19 when ballistic phonon transport is dominant at Kn = 10. Most of transition from diffusive to ballistic thermal transport (over 75% of the $q^*_{y,SS}$ change) occurs within a small Kn range up to Kn = 1. Once the domain size becomes comparable to the mean free path, $q^*_{y,SS}$ does not increase as quickly, increasing only 25% as Kn changes from 1 to 10. This trend indicates that diffusive-to-ballistic transition below Kn = 1 is likely due to phonon transport from the hot wall to the sidewalls, while the further increase of $q^*_{y,SS}$ above Kn = 1 is attributed to phonon transport to the bottom wall.

The effect of the angular domain discretization to the accuracy of the BTE solution is shown in Fig. 2.4 for Kn = 1 and 10, respectively. Gaussian quadrature distribution was used to discretize the angular direction to 2×2, 8×4, and 32×8, where the first number

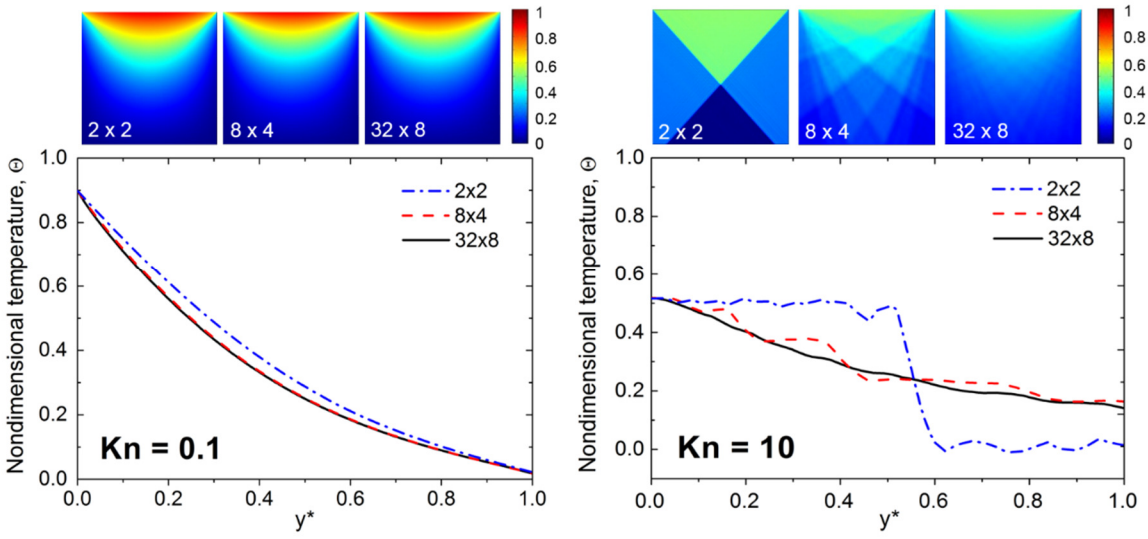

Figure 2.4. Effects of the angular domain discretization to the accuracy of the BTE solution when (a) Kn = 0.1 and (b) Kn = 10. As can be seen clearly in (b), the ray effect is the main source of numerical errors, and angular refinement is crucial to get more accurate results particularly for high Kn numbers

represents the number of discretized polar angles and the second represents that of azimuthal angles. For Kn = 0.1, not many angular discretization is required to ensure a smooth solution, although the 2×2 case yields the erroneous temperature distribution when compared with the 8×4 and 32×8 cases. However, significant wiggles are observed for Kn = 10 when 2×2 or 8×4 are implemented. This ray effect is slightly observed even for the 32×8 case, indicating that more angular refinement is required for a smooth temperature curve at high Kn. We believe that over 1000 equations should be solved simultaneously if the standard DOM is used for Kn > 5, or modified DOMs should be implemented to diminish the ray effect [37–39].

Fig. 2.5 shows the transient temperature change of the square domain with contour plots and nondimensional temperature distributions along the centerline for different Kn numbers. As mentioned earlier, the domain size for the Fourier conduction analysis is

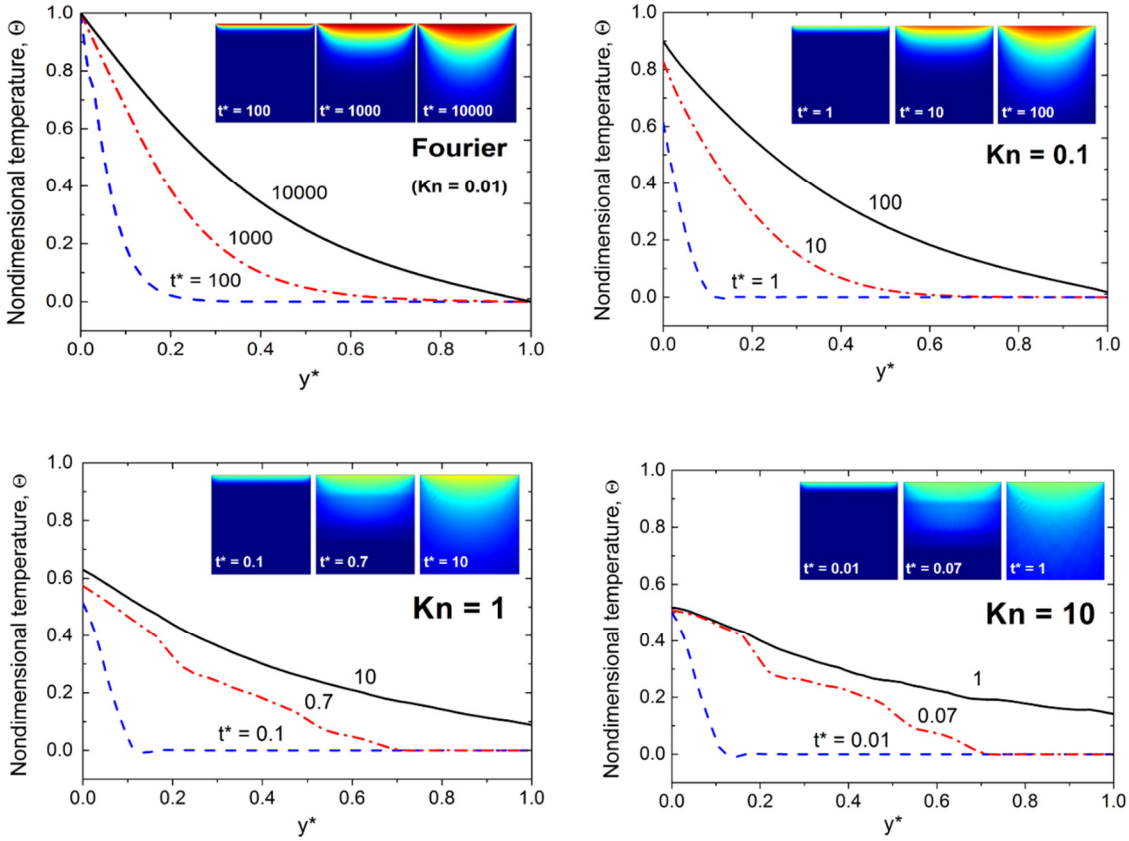

Figure 2.5. Transient nondimensional temperature changes along the centerline of the square domain computed by (a) the Fourier simulation (Kn = 0.01) and the BTE simulation for (b) Kn = 0.1, (c) Kn = 1 and (d) Kn = 10. The temperature contours are for each case are also shown in the inset

assumed to be approximately 100 times the phonon mean free path (Kn = 0.01). Apparently, the Fourier conduction yields no temperature jump at the boundaries during the transient temperature change, reaching the steady state when the nondimensional time ($t^* = t / \tau$) becomes in the order of 10000. On the other hand, the BTE solution at Kn = 0.1 shows the transient change of the boundary temperature at the center of the top wall ($x^* = 0, y^* = 0$), from the substantial jump down to 0.6 at the initial time step ($t^* = 1$) to the gradual recovery to 0.9 at the steady state ($t^* = 100$). This observation suggests that the initial phonon transport be governed by its ballistic nature while the following transient

behavior is dominated by the diffusive thermal energy transport. The transient boundary temperature change at the top wall becomes small as Kn increases and finally disappears at Kn = 10, where thermal energy is ballistically transferred across the square domain. For all Kn ranges under consideration, time that is required to reach the steady state can be approximated to be $10\tau / \mathrm{Kn}$, where τ / Kn is the time scale for thermal information to propagate from one side to the other side. It should be noted that the ray effect is still observed for high Kn numbers, and it is more severe at the intermediate time step than the initial and steady-state solutions.

Fig. 2.6 shows the transient heat flux throughout the domain as well as heat flux in the *y*-direction along the centerline of the domain for different Kn numbers. The transient heat flux is normalized using $q_y^* = q_y'' / q_{y,SS,Fourier}''$, similarly to the steady case. At Kn = 0.1, the transient heat flux diffusively changes from the high heat flux initially at the top wall to the smoothly distributed heat flux across the domain at the steady state. At Kn = 10, however, no change is observed in the transient heat flux at the center of the top wall, i.e., $q_y^*(0,0) \approx 19$, while the heat flux at the bottom wall increases up to $q_y^*(0,1) \approx 8$. For more insightful discussions, the transient change of the heat flux at the center of the top wall is shown in Fig. 2.7. Although not fully plotted for clarity, all Kn cases start from the same initial wall heat flux at $q_y^*(0,0) \approx 19$ and follow the almost identical trajectory formed by the overlying transient curves for different Kn numbers until they reach the steady state. At high Kn numbers, the wall heat flux experiences only a small transient change, e.g., only around 3% for Kn = 10, as it reaches the steady state. The transient change of the wall heat flux becomes more substantial as Kn decreases, e.g., ~ 24% decrease for Kn = 1 and ~ 95% decrease for Kn = 0.02. Such substantial changes occur in the time interval from *t**

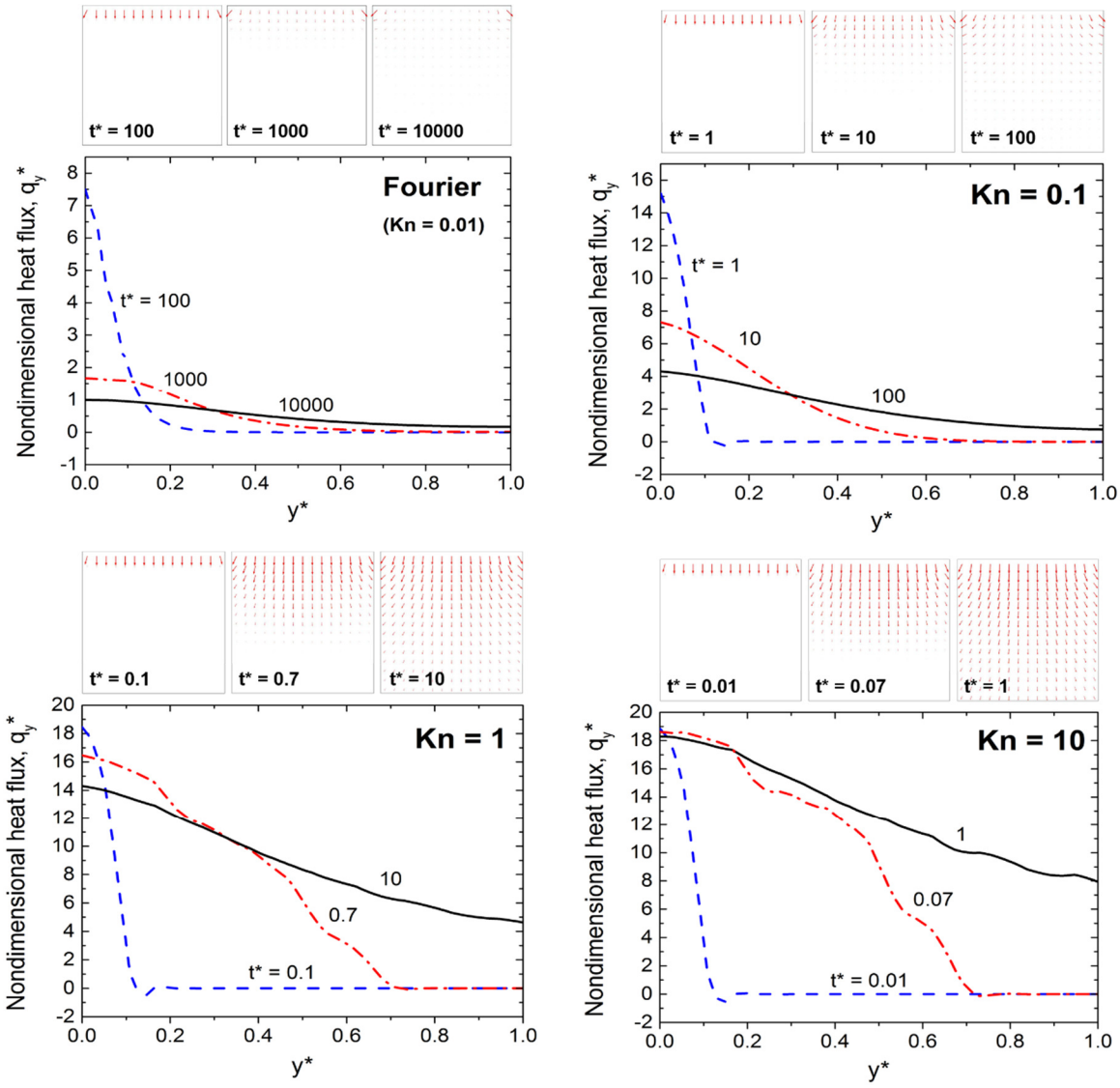

Figure 2.6. Transient nondimensional heat flux in the y-direction along the centerline of the square domain computed by (a) the Fourier simulation (Kn = 0.01) and the BTE simulation for (b) Kn = 0.1, (c) Kn = 1 and (d) Kn = 10. The heat flux distributions are also plotted in arrows for different time steps. Heat flux is normalized using steady Fourier heat flux at the center of the top boundary, i.e., $q_y^* = q_y / q_{y,Fourier,SS}$.

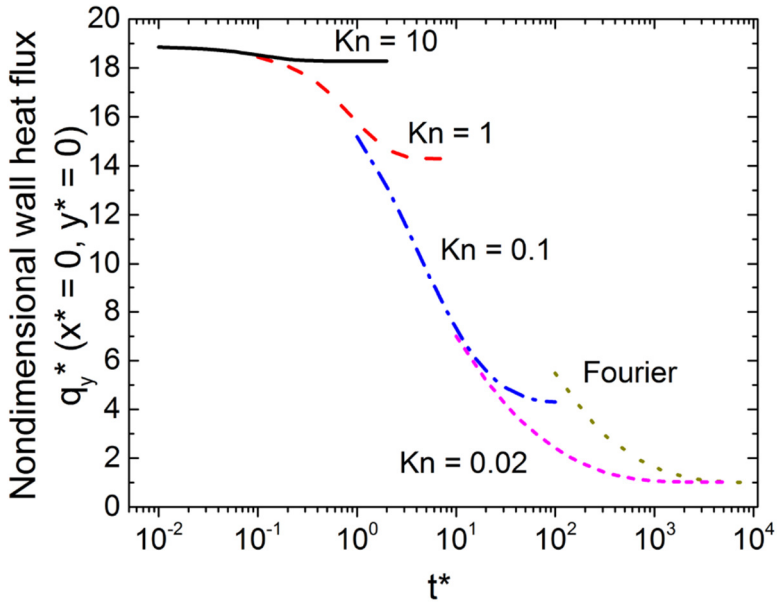

Figure 2.7. Transient change of the heat flux in the y-direction at the center of the top wall predicted by the BTE for different Kn numbers and by the Fourier heat conduction equation (Kn = 0.02). When the BTE and Fourier solutions are compared for the same Kn number (Kn = 0.02), the Fourier heat conduction equation overestimates the transient behaviors in the early transient stage.

= 10^0 to 10^3 due to the contribution of the diffusive nature of phonon heat transfer in this domain. It should be noted that the nondimensional wall heat flux for Kn = 0.02 gradually decrease to finally approach unity at the steady state: it becomes fully diffusive at the steady state. However, the Fourier conduction at the same Kn number (Kn = 0.02) overestimates the transient wall heat flux in the early transient stage. We believe that the deviation between the BTE and the Fourier model may result from the contribution of ballistic phonon transport in the early transient behavior.

2.5 Conclusion

In this paper, the transient Boltzmann transport equation (BTE) with the gray relaxation-time approximation was numerically solved to investigate the ballistic-diffusive

nature of phonon heat transport in the micro/nanoscale. The 2-D BTE was solved for different Kn numbers ranging from 0.01 to 10 by implementing the finite element analysis (FEA) and the discrete ordinates method (DOM). When compared with the semi-analytical solution for the 1-D equation of phonon radiative transfer (EPRT), the DOM-FEA shows an excellent agreement within 0.18% for Kn = 0.1 and 0.62% for Kn = 10 for a high aspect-ratio rectangular domain. By solving the BTE for a square domain with fixed temperature boundary conditions, we demonstrated that phonon heat transport undergoes diffusive to ballistic transition as Kn increases. The transient analysis of phonon heat transport was also conducted using the BTE, showing different transient behaviors for diffusive and ballistic phonon heat transport. The ray effect turned out to be the main source of error for the DOM-FEA scheme, but can be diminished with angular refinement. Although only simple 2-D geometries were considered in the present study, the DOM-FEA can be easily extended to other 2-D and 3-D geometries with complicated boundary conditions. Since the FEA is a readily accessible simulation tool with commercial packages, our approach will benefit general users in computing ballistic-diffusive phonon heat transfer and integrating the results with microdevice designs and multiphysics analysis.

2.6 Acknowledgement

This work was supported by the National Research Foundation Grant funded by the Korean Government (NRF-2011-220-D00014) and the National Science Foundation (CBET-1067441). SH and KP also acknowledge the startup support at the University of Utah, including the computation at the Center for High-Performance Computing (CHPC).

2.7 References

[1] C.L. Tien, A. Majumdar, F. Gerner, Microscale Energy Transport, first ed., Taylor and Francis, New York, 1998.

[2] G. Chen, Nanoscale Energy Transport and Conversion: A Parallel Treatment of Electrons, Molecules, Phonons, and Photons, Oxford University Press, New York, 2005.

[3] Z.M. Zhang, Nano/Microscale Heat Transfer, fifth ed. McGraw Hill, New York 2007.

[4] K. Park, G.LW. Cross, Z.M. Zhang, W. King, Experimental investigation on the heat transfer between a heated microcantilever and a substrate, J. Heat Transfer 130 (2008) 102401.

[5] J.Y. Murthy, S.V.J. Narumanchi, J.A. Pascual-Gutierrez, T. Wang, C. Ni, S.R. Mathur, Review of Multiscale Simulation in Submicron Heat Transfer, Int. J. Multiscale Comput. Eng. 3 (1) (2005) 5–32.

[6] G. Chen, Nonlocal and Nonequilibrium Heat Conduction in the Vicinity of Nanoparticles, J. Heat Transfer 118 (3) (1996) 539.

[7] A.A. Joshi, A. Majumdar, Transient Ballistic and Diffusive Phonon Heat Transport in Thin Tilms, J. Appl. Phys. 74 (1) (1993) 31.

[8] A. Majumdar, Microscale Heat Conduction in Dielectric Thin Films, J. Heat Transfer 115 (1993) 7–16.

[9] T. Zeng, G. Chen, Phonon Heat Conduction in Thin Films: Impacts of Thermal Boundary Resistance and Internal Heat Generation, J. Heat Transfer 123 (2) (2001) 340.

[10] G. Chen, Thermal Conductivity and Ballistic-Phonon Transport in the Cross-Plane Direction of Superlattices, Phys. Rev. B 57 (23) (1998) 14958.

[11] D. Singh, J.Y. Murthy, T.S. Fisher, Phonon Transport Across Mesoscopic Constrictions, J. Heat Transfer 133 (4) (2011) 042402.

[12] S.V.J. Narumanchi, J.Y. Murthy, C.H. Amon, Simulation of Unsteady Small Heat Source Effects in Sub-Micron Heat Conduction, J. Heat Transfer 125 (5) (2003) 896.

[13] S.V.J. Narumanchi, J.Y. Murthy, C.H. Amon, Submicron Heat Transport Model in Silicon Accounting for Phonon Dispersion and Polarization, J. Heat Transfer 126 (6) (2004) 946.

[14] A.J. Minnich, G. Chen, S. Mansoor, B.S. Yilbas, Quasiballistic Heat Transfer Studied using the Frequency-Dependent Boltzmann Transport Equation, Phys. Rev.

B 84 (23) (2011) 235207.

[15] J.Y. Murthy, S.R. Mathur, An Improved Computational Procedure for Sub-Micron Heat Conduction, in ASME 2002 International Mechanical Engineering Congress and Exposition, vol. 7(5), 2002, p. 75.

[16] J.Y. Murthy, S.R. Mathur, Computation of Sub-Micron Thermal Transport Using an Unstructured Finite Volume Method, J. Heat Transfer 124 (6) (2002) 1176.

[17] A. Mittal, S. Mazumder, Hybrid Discrete Ordinates - Spherical Harmonics Solution to the Boltzmann Transport Equation for Phonons for Non-Equilibrium Heat Conduction, J. Comput. Phys. 230 (18) (2011) 6977.

[18] P. Lee, R. Yang, K. Maute, An Extended Finite Element Method for the Analysis of Submicron Heat Transfer Phenomena, in: R. de Borst E. Ramm (Eds.), Multiscale Methods in Computational Mechanics, Lecture Notes in Applied and Computational Mechanics, vol. 55, pp. 195–212, 2011.

[19] S. Pisipati, C. Chen, J. Geer, B. Sammakia, B.T. Murray, Multiscale Thermal Device Modeling using Diffusion in the Boltzmann Transport Equation, Int. J. Heat Mass Transf. 64 (2013) 286.

[20] S. Sihn, A.K. Roy, Nanoscale Heat Transfer using Phonon Boltzmann Transport Equation, in COMSOL Conference, 2009, p. 1.

[21] R. Yang, G. Chen, M. Laroche, Y. Taur, Simulation of Nanoscale Multidimensional Transient Heat Conduction Problems Using Ballistic-Diffusive Equations and Phonon Boltzmann Equation, J. Heat Transfer 127 (3) (2005) 298.

[22] G. Chen, Ballistic-Diffusive Heat Conduction Equations, Phys. Rev. Lett. 86 (2001) 2230.

[23] G. Chen, Ballistic-Diffusive Equations for Transient Heat Conduction From Nano to Macroscales, J. Heat Transfer 124 (2) (2002) 320.

[24] A. Mittal, S. Mazumder, Generalized Ballistic-Diffusive Formulation and Hybrid SN-PN Solution of the Boltzmann Transport Equation for Phonons for Nonequilibrium Heat Conduction, J. Heat Transfer 133 (9) (2011) 092402.

[25] A.J.H. McGaughey, M. Kaiviany, Phonon Transport in Molecular Dynamics Simulations: Formulation and Thermal Conductivity Prediction, Adv. Heat Transf. 39 (2006) 169.

[26] S.K. Saha, L. Shi, Molecular Dynamics Simulation of Thermal Transport at a Nanometer Scale Constriction in Silicon, J. Appl. Phys. 101 (7) (2007) 074304.

[27] S. Mazumder, A. Majumdar, Monte Carlo Study of Phonon Transport in Solid Thin Films Including Dispersion and Polarization, J. Heat Transfer 123 (4) (2001) 749.

[28] T. Klitsner, J. VanCleve, H. Fischer, R. Pohl, Phonon Radiative Heat Transfer and Surface Scattering, Phys. Rev. B 38 (11) (1988) 7576.

[29] J. Randrianalisoa, D. Baillis, Monte Carlo Simulation of Steady-State Microscale Phonon Heat Transport, J. Heat Transfer 130 (7) (2008) 072404.

[30] M.-S. Jeng, R. Yang, D. Song, G. Chen, Modeling the Thermal Conductivity and Phonon Transport in Nanoparticle Composites Using Monte Carlo Simulation, J. Heat Transfer 130 (4) (2008) 042410.

[31] A. Nabovati, D. P. Sellan, C. H. Amon, On the Lattice Boltzmann Method for Phonon Transport, J. Comput. Phys. 230 (15) (2011) 5864.

[32] Y.-F. Han, X.-L. Xia, H.-P. Tan, H.-D. Liu, Modeling of Phonon Heat Transfer in Spherical Segment of Silica Aerogel Grains, Phys. B: Condens. Matter 420 (2013) 58.

[33] S. Pisipati, J. Geer, B. Sammakia, B.T. Murray, A Novel Alternate Approach for Multiscale Thermal Transport using Diffusion in the Boltzmann Transport Equation, Int. J. Heat Mass Transf. 54 (15-16) (2011) p. 3406.

[34] T. Yamada, S. Hamian, B. Sundén, K. Park, M. Faghri, Diffusive-Ballistic Heat Transport in Thin Films using Energy Conserving Dissipative Particle Dynamics, Int. J. Heat Mass Transf. 61 (2013) 287.

[35] K.E. Sverdrup, P.G. Ju, Y.S. Goodson, Sub-Continuum Simulations of Heat Conduction in Silicon-on-Insulator Transistors, J. Heat Transf. 123 (2001) 130.

[36] L. Pilon, K.M. Katika, Modified Method of Characteristics for Simulating Microscale Energy Transport, J. Heat Transfer 126 (5) (2004) 735.

[37] J.C. Chai, H.S. Lee, S.V. Patankar, Finite Volume Method for Radiation Heat Transfer, J. Thermophys. Heat Transf. 8 (3) (1994) 419.

[38] S.V. Chai, J.C., Lee, H.S., Patankar, Ray Effect and False Scattering in the Discrete Ordinates Method, Numer. Heat Transf. 24 (1993) 373.

[39] P.H. Gaskell, A.K.C. Lau, Curvature-Compensated Convective Transport: SMART, A New Boundedness Preserving Transport Algorithm, Int. J. Numer. Methods Fluids 8 (1988) 617.

CHAPTER 3

ELECTROTHERMAL CHARACTERIZATION OF DOPED-SI HEATED MICROCANTILEVERS UNDER PERIODIC HEATING OPERATION

Reproduced from Journal of Heat Transfer (2016) **138**, 052401-1. Electrothermal Characterization of Doped-Si Heated Microcantilevers Under Periodic Heating Operation. Sina Hamian, Andrew M Gauffreau, Timothy Walsh, Jungchul Lee, Keunhan Park, © Owned by the authors, published by ASME, 2016, with the permission of the Journal of Heat Transfer (JHT).

3.1 Abstract

This paper reports the frequency-dependent electrothermal behaviors of a freestanding doped-silicon heated microcantilever probe operating under periodic (ac) Joule heating. We conducted a frequency-domain finite-element analysis (FEA) and compared the steady periodic solution with 3ω experiment results. The computed thermal transfer function of the cantilever accurately predicts the ac electrothermal behaviors over a full spectrum of operational frequencies, which could not be accomplished with the 1D approximation. In addition, the thermal transfer functions of the cantilever in vacuum and in air were compared, through which the frequency-dependent heat transfer coefficient of the air was quantified. With the developed FEA model, design parameters of the cantilever (i.e., the

size and the constriction width of the cantilever heater) and their effects on the ac electrothermal behaviors were carefully investigated. Although this work focused on doped-Si heated microcantilever probes, the developed FEA model can be applied for the ac electrothermal analysis of general microelectromechanical systems.

3.2 Introduction

The advent of the micro/nanotechnology has created a pressing need for the ability to analyze and manipulate nanoscale structures. Thermal microcantilevers, which can measure and manipulate local thermal fields with an integrated thermal transducer, have proven uniquely suited to this task. Thermal microcantilevers have been widely used in various tip-based thermal metrologies, such as nanoscale thermometry [1–6] and thermal analysis [7–11], thermally driven topography mapping [12–16], and nanoscale infrared spectroscopy [17–22]. Heated tips also have been actively used for thermomechanical nanomanufacturing, such as data storage [23,24], synthesis/modification of carbon-based nanostructures [25–27], additive manufacturing of polymers [28–30], chemical species [31], and metals [32], and subtractive manufacturing of energetic [7] and organic [33–36] materials.

While most of the aforementioned applications operate thermal cantilevers at steady-state or with short electrical pulses, the periodic heating (ac) operation could realize precision scientific measurements that are not feasible with the steady-state cantilever operation. By implementing the 3ω method [37], thermal cantilevers can measure local temperature with a resolution of ~1 mK [38,39], opening the possibility of nanoscale thermophysical property measurement. The photothermomechanical actuation of

cantilever probes is another example of the periodic heating operation [40–43]. By photothermally oscillating a cantilever with a modulating laser and monitoring the oscillation amplitude and phase changes at different modulation frequencies, the periodic heating technique can be used for high-resolution solution imaging [44,45], virus detection [46], and deoxyribonucleic acid (DNA) bound enumeration [47]. When considering the growing impacts of the periodic heating operation of microcantilever probes on micro/nanoscale thermal metrologies, it is imperative to systematically understand their frequency-dependent thermal behaviors.

The present study aims to investigate the frequency-dependent electrothermal responses of a doped-silicon (Si) heated microcantilever under periodic heating conditions. The doped-Si microcantilever is one of the most widely used thermal probes that has a lightly doped heater region at its free end and a heavily doped leg region, thus allowing the local heating of the tip above 1000 K and precision resistive thermometry [48]. However, understanding the full-spectrum 3ω signal of the doped-Si heated cantilever still remains challenging, mainly due to the inherent complexities of the cantilever, such as the presence of two doped regions, nonlinear temperature dependence of the cantilever resistance, and the complicated geometry. While previous studies have attempted to predict the ac behaviors of the microcantilever with a simple 1-D model [38,39,49–53], they observed serious deviations of the 1D model from experimental data at high frequencies [51,52]. FEA was applied for the transient modeling of the cantilever during pulse and periodic heating operations [54]. However, FEA in the time domain is computationally expensive to obtain steady periodic solutions under the ac operation. To conduct a more cost effective yet accurate frequency-dependent electrothermal analysis, the present study implements a

frequency-domain FEA that can accurately predict the in-phase and out-of-phase 3ω voltage signals and the corresponding thermal transfer functions. The obtained results are compared with the measured thermal transfer functions for a full range of the operational frequencies from 10 Hz to 34 kHz under vacuum conditions. In addition, the thermal transfer functions of the cantilever in vacuum and air environments are compared to demonstrate that the air heat conduction significantly affects the ac electrothermal behaviors of the cantilever. The effects of the heater size and the constriction width on the ac electrothermal behaviors of the cantilever are also investigated to optimize the cantilever design for periodic heating.are

3.3 Experiment

Figure 3.1(a) illustrates the experimental setup for the 3ω signal measurement of a doped-Si heated cantilever alongside a scanning electron microscope (SEM) image of the cantilever. The leg region of the cantilever is 133 μm in length and 20 μm wide, while the constriction region is 35 μm in length and 7.6 μm in width. The constriction region includes a 16 μm long heater at the free end. The cantilever thickness was also determined from the SEM images: see supplemental Fig. 3.S1(a), which is available under the Supplemental Data tab for this paper on the ASME Digital Collection. The cantilever is thicker at the free end (1.63±0.01 μm) than at the anchor (1.18±0.01 μm), from which the average cantilever thickness is estimated to be 1.33 μm. The cantilever was mounted on a temperature-controlled stage in a Janis VPF-800 cryostat, which was used as a high vacuum chamber in the present study. A turbo pump (Pfeiffer HiCube 80 Eco) was used to acquire a vacuum condition of 10^{-5} Torr. The cantilever was connected in a Wheatstone bridge circuit with

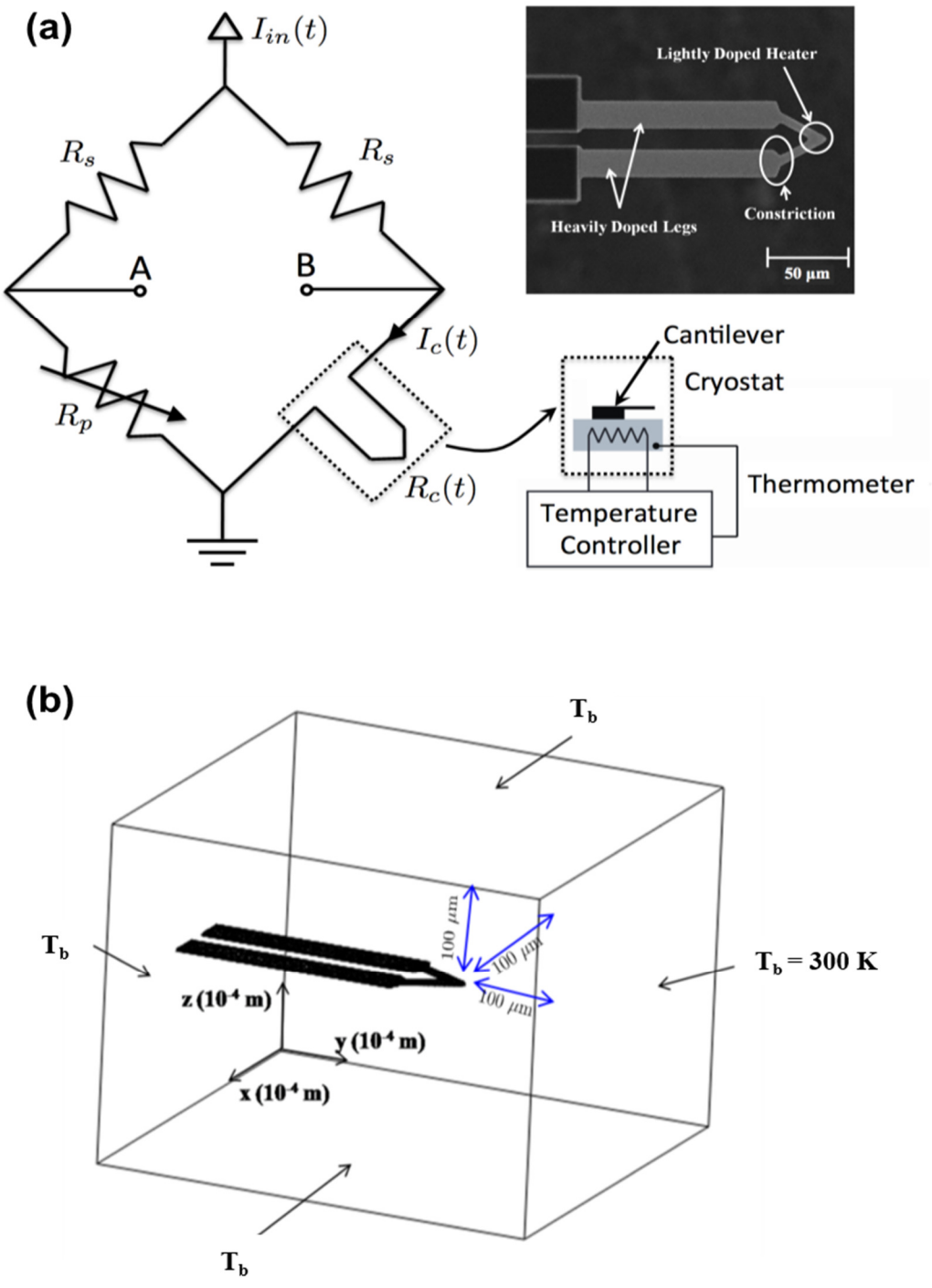

Figure 3.1. (a) Schematic of the *3ω* experimental setup with the SEM image of a doped-Si heated microcantilever and (b) its FEA model with an environment box. The cantilever base was anchored to the wall of the environment box while the remaining cantilever facets were spaced 100 μm away from the other side walls.

a pair of 10 kΩ sense resistors and a potentiometer. The sense resistors were noninductive resistors with 1% tolerance, being purely resistive at frequencies up to 100 MHz. The Wheatstone bridge was used as a nulling circuit to minimize the 1ω signal, which is typically over 1000 times greater than the 3ω signal and would create a lack of precision in the 3ω measurement [52]. The effective temperature coefficient of resistivity (TCR) of the cantilever at 300 K was determined by measuring the resistance while changing the stage temperature from 300 K to 310 K with a 50 mK accuracy. An ac input current of 112 μA-rms was applied to the bridge circuit by a Keithley 6221 ac/dc source meter over a range of frequencies spanning 10 Hz–34 kHz. The direct use of a current source obviates the signal adjustment that is required to correct a measurement error when using a voltage source [39,55]. While the cantilever was operated under periodic current flow in a vacuum environment, the in-phase and out-of-phase 3ω voltage signals across the cantilever were measured by a differential lock-in scheme [37].

3.4 FEA Modeling

Figure 3.1(b) illustrates the 3-D FEA model of the heated microcantilever suspended freely in the environment box. The surrounding box was assumed to be 100 μm away from the free end of the cantilever, filled with quiescent air or in vacuum depending on the operational condition. The previous computational study showed that the heater temperature of the cantilever in the 100-μm-thick air box is within 1% deviation from that in the 1000-μm-thick air box [54]. The temperature at the walls was set to $T_b = 300$ K. The transient heat conduction equation of the cantilever is written as

$$C_i \frac{\partial \Theta(\mathbf{r},t)}{\partial t} = \nabla \cdot \left[k_i \nabla \Theta(\mathbf{r},t)\right] + \dot{q}_i(t) \tag{3.1}$$

where $\Theta = T - T_b$ is the temperature difference relative to the base temperature T_b, and C, k, and $\dot{q}_i$ are the volumetric heat capacity, the thermal conductivity and the volumetric heat generation rate, respectively. The subscript i is used to denote the heater and leg regions of the cantilever to reflect different thermal and electrical properties for different doping level. The cantilever can be segmented into more subdomains in the FEA if neccessary. When the cantilever is periodically heated, it is computationally expensive to obtain the steady periodic solution of Eq. (3.1) in the time domain without losing information. The Nyquist theorem demands the sampling rate to be at least double that of the heating frequency for a smooth solution. Moreover, initial transient periods exist before the solution reaches the steady periodic state, imposing extra computational cost. As an alternative approach to address these challenges, this study employs the complex temperature method in the frequency domain [56].

When the input current has both dc and ac components (I_0 and I_ω, respectively), the input current is written as $I(t) = I_\omega[\eta + \cos(\omega t)]$, where $\eta = I_0 / I_\omega$. Under a small ac current input to the cantilever, the power dissipation can be approximated as $Q(t) = I(t)^2 R_0$, where R_0 is the dc-offset cantilever resistance under the periodic heating operation. The complex form of the heat generation in each region can be expressed as $Q_i(t) = \mathrm{Re}[Q_0 + Q_{1\omega} e^{j\omega t} + Q_{2\omega} e^{j2\omega t}]_i$, where

$$
\begin{aligned}
Q_0 &= \left(\sqrt{\eta^2 + 1/2}\, I_\omega\right)^2 R_0 \\
Q_{1\omega} &= \left(\sqrt{2\eta}\, I_\omega\right)^2 R_0 \\
Q_{2\omega} &= \left(I_\omega / \sqrt{2}\right)^2 R_0
\end{aligned}
\tag{3.2}
$$

It should be noted that higher harmonics beyond 2ω are not considered here due to their relatively small values. However, they should be considered for accurate calculation when the cantilever is operated near the thermal runaway point with high nonlinearity [51]. By expressing the temperature oscillation in a complex form as $\Theta(\mathbf{r},t) = \mathrm{Re}[\Theta_0(\mathbf{r}) + \tilde{\Theta}_{1\omega}(\mathbf{r})e^{j\omega t} + \tilde{\Theta}_{2\omega}(\mathbf{r})e^{j2\omega t}]$ and decomposing the harmonic terms into real and imaginary components, i.e., $\tilde{\Theta}_{n\omega} = \left[\Theta_R + j\Theta_I\right]_{n\omega}$, Eq. (3.1) becomes the following equation set in the frequency domain:

$$
\begin{aligned}
&\nabla \cdot \left[k_i \nabla \Theta_0(\mathbf{r})\right] + \dot{q}_0(\mathbf{r}) = 0 \\
&\nabla \cdot \left[k_i \nabla \Theta_{R,n\omega}(\mathbf{r})\right] + \dot{q}_{n\omega}(\mathbf{r}) = -n\omega C_i \Theta_{I,n\omega}(\mathbf{r}) \\
&\nabla \cdot \left[k_i \nabla \Theta_{I,n\omega}(\mathbf{r})\right] = n\omega C_i \Theta_{R,n\omega}(\mathbf{r})
\end{aligned}
\tag{3.3}
$$

where n = 1 or 2 depending on the harmonic order under consideration. The thermal conductivity of doped Si was taken from the previous studies considering the doping level, temperature, and boundary scattering (i.e., k_H = 121 W/m-K and k_L = 65 W/m-K at 300K) [57,58], and the specific heat was assumed to be the same as that of intrinsic bulk Si for both the heater and leg regions [59]. Only heat conduction was considered as a dominant heat transfer mechanism in the air due to the reduced surface area of the cantilever, as confirmed in the previous studies [51,60,61]. Thermal radiation was neglected during

periodic heating because $8\sigma_s T_b^3 l^2 / \pi^2 kd \ll 1$, where σ_s is the Stefan-Boltzmann constant, l and d are the characteristic length and thickness of the cantilever, respectively, and k is the thermal conductivity of the cantilever. The relative contribution of thermal radiation was estimated to be 2.306×10^{-4} for the cantilever, which is small enough to ignore thermal radiation.

The volumetric heat generation in Eq. (3.3) can be determined by numerically solving Gauss's law at dc and each harmonic component:

$$\nabla \cdot [\sigma_0(\mathbf{r}) \nabla \Phi_{n\omega}(\mathbf{r})] = 0 \tag{3.4}$$

where $\Phi_{n\omega}(\mathbf{r})$ is the electric potential at each harmonic component and σ_0 is the local electrical conductivity of doped Si at the dc-offset temperature, i.e., $T_0 = T_b + \Theta_0$. In order to calculate the temperature-dependent electric conductivity of doped Si, we implemented Reggiani's model that predicts the carrier mobility of phosphorus-doped silicon for the doping concentration of 10^{14} – 10^{21} cm^{-3} up to 700 K [62] and Kuzmicz's ionization model that is valid for 10^{15} – 10^{20} cm^{-3} for 250 – 400 K with an accuracy better than 3% [63]. Since a doping profile across the cantilever thickness is not uniform due to phosphorus implantation and diffusion processes, doping profiles for the heater and leg regions were obtained by running the Ssuprem3 simulation with the implantation and diffusion conditions of phosphorus used in the cantilever fabrication (see supplemental Fig. 3.S2 which is available under the Supplemental Data tab for this paper on the ASME Digital Collection) [64]. The harmonic components of the volumetric heat generation can then be written as $\dot{q}_{n\omega}(\mathbf{r}) = J_{n\omega}(\mathbf{r})^2 / \sigma_0(\mathbf{r})$, where $J_{n\omega}(\mathbf{r}) = -\sigma_0(\mathbf{r}) \nabla \Phi_{n\omega}(\mathbf{r})$ is the local electric

current density. To solve Eq. (3.4) in the frequency domain, Eq. (3.2) was interpreted as $Q_{n\omega} = I_{n\omega}^2 R_0$, where $I_{n\omega}$ is a dummy electric current representing joule-heating at each harmonic, and applied as the boundary conditions under the assumption of the uniform current density, i.e., $J_{n\omega,b} = I_{n\omega} / A_L$, where A_L is the cross section area of the cantilever leg.

To compare the 3ω experimental results with the FEA simulation, the voltage drop across the cantilever was calculated from the current input and cantilever resistance using $V_C(t) = I(t)R_C(t)$, where $R_C(t)$ is the time-harmonic electrical resistance of the cantilever. When the cantilever is operated under the small ac current input, the electrical resistance of the cantilever can be assumed to be in the same phase as the temperature oscillation. The complex cantilever resistance oscillation $\tilde{R}_C(t)$ can be expressed as $\tilde{R}_C(t) = R_0 + \tilde{R}_{1\omega} e^{j\omega t} + \tilde{R}_{2\omega} e^{j2\omega t}$. Due to the small current input, the cantilever resistance varies linearly with the averaged temperature change to yield $\tilde{R}_{n\omega} = \sum_i [R_0 \alpha \bar{\Theta}_{n\omega}]_i$, where α_i is the TCR of *i*-th region at the base temperature T_b, and $\bar{\Theta}_{n\omega}$ is the averaged ac temperature at each harmonic. After manipulation, the complex voltage drop across the cantilever can be expressed as $\tilde{V}_C(t) = V_0 + \sum_{n=1}^{3} \tilde{V}_{n\omega} e^{jn\omega t}$, where

$$
\begin{aligned}
V_0 &= I_\omega \left[\eta R_0 + \sum_i \left(\frac{\left|\tilde{R}_{1\omega}\right|}{2} \cos \bar{\varphi}_{1\omega} \right)_i \right] \\
\tilde{V}_{1\omega} &= I_\omega \left[R_0 + \sum_i \left(\eta \tilde{R}_{1\omega} + \frac{\tilde{R}_{2\omega}}{2} \right)_i \right] \\
\tilde{V}_{2\omega} &= I_\omega \sum_i \left(\frac{\tilde{R}_{1\omega}}{2} + \eta \tilde{R}_{2\omega} \right)_i \\
\tilde{V}_{3\omega} &= I_\omega \sum_i \left(\frac{\tilde{R}_{2\omega}}{2} \right)_i
\end{aligned}
\tag{3.5}
$$

It should be noted that the dc and 2ω harmonics of the cantilever voltage become zero if the input current does not have a dc offset ($\eta = 0$). The ac electrothermal behaviors of the cantilever can be better characterized with the thermal transfer function. The second harmonic thermal transfer function, or simply the thermal transfer function in this study, is related with the 3ω voltage signal [55]

$$
\tilde{Z}_{2\omega} = -\frac{2V_{3\omega\text{-rms}}}{\bar{\alpha} R_0^2 I_{\omega\text{-rms}}^3} \tag{3.6}
$$

where $\bar{\alpha}$ is the effective TCR of the cantilever at the base temperature T_b, determined from the slope of the dc cantilever resistance change. It should be noted that the thermal transfer function has a unit of K/mW, equivalent to the thermal impedance, thus indicating the in-phase (real) and out-of-phase (imaginary) temperature oscillations for a given periodic power dissipation [52].

In the present study, a commercial package (COMSOL Multiphysics) was used to compute the elctrical and thermal transport behaviors of the cantilever in the frequency

domain. For the numerical simulation, 70,000 tetrahedral elements were used to mesh the whole domain. In order to avoid mesh-dependence of the solution and increase the computational speed, the mesh size was made smaller in the heater region compared to that away from the heater. The mesh size effect on convergence is presented in supplemental Fig. 3.S3, which is available under the Supplemental Data tab for this paper on the ASME Digital Collection where the maximum thermal transfer function computed with 70,000 meshes is converged to the result for 675,000 mesh elements within a 0.03% error. All the simulations were performed at the Center for High Performance Computing (CHPC) at the University of Utah. When using a 64GB memory and 2.6GHz CPU on a CHPC computing node, the calculation time for 53 frequency points between 10 Hz and 34 kHz was half an hour for the vacuum case and 4 hrs for the air case, respectively.

3.5 Results and Discussion

While other parameters were used from the design values, the doping concentration at the top surface of the heater region was numerically determined by comparing the calculated TCR of the cantilever with the measurement. As mentioned in Section 3, the depth profiles of doping concentration in heater and leg regions, $N_H(z)$ and $N_L(z)$, were adopted from the Ssuprem3 simulation (see supplemental Fig. 3.S2., which is available under the Supplemental Data tab for this paper on the ASME Digital Collection) [64]. For simplicity of the computation, we used the design value for the doping concentration at the top surface of the leg region, i.e., $N_L(z=0) = 1.7\times10^{20}$ cm^{-3}. However, the doping concentration at the top surface of the heater region $N_H(z=0)$ should be carefully determined, as ~93% of the cantilever resistance is attributed to the heater region [52]. We

calculated the electrical resistance of the cantilever suspended in vacuum for different base temperatures from 300 K to 310 K and fitted the calculated values with the measurement by adjusting $N_H(0)$. As shown in supplemental Fig. 3.S4, which is available under the Supplemental Data tab for this paper on the ASME Digital Collection, the corresponding TCR of the cantilever is estimated to be $(1.77\pm0.02)\times10^{-3}$ K^{-1} at room temperature, which is slightly lower than the previous measurement (i.e., 0.0029 K^{-1} [38]). We believe that this difference is mainly due to the variance of the doping concentration at the heater region in different cantilever batches. The estimated doping concentration at the top surface of the heater region is 7.96×10^{17} cm^{-3}, which is in the same order of the target doping concentration for the heater region. Using the obtained parameters, we computed the temperature distribution of the cantilever under the steady-heating (or dc) operation: see Fig. 3.S4, which is available under the Supplemental Data tab for this paper on the ASME Digital Collection.

Figure 3.2 shows the in-phase and out-of-phase thermal transfer functions of the cantilever in vacuum. To ease the comparison between the measurement and the computation, the thermal transfer function was normalized by the thermal resistance (or the dc thermal transfer function) Z_0, which was calculated to be 98 K/mW from the steady state analysis. The overall agreement is very good within ~2.4 % for the in-phase component and ~6.1 % for the out-of-phase component. The negative in-phase values in the measurement at high frequencies over 10 kHz is due to parasitic electrical impedance of the cantilever and the involved circuit [51,52]. At low frequencies, the thermal transfer function of the cantilever is similar to that of a 1-D suspended wire, exhibiting a typical first-order ac response [55]. This similarity indicates that heat generated at the heater region

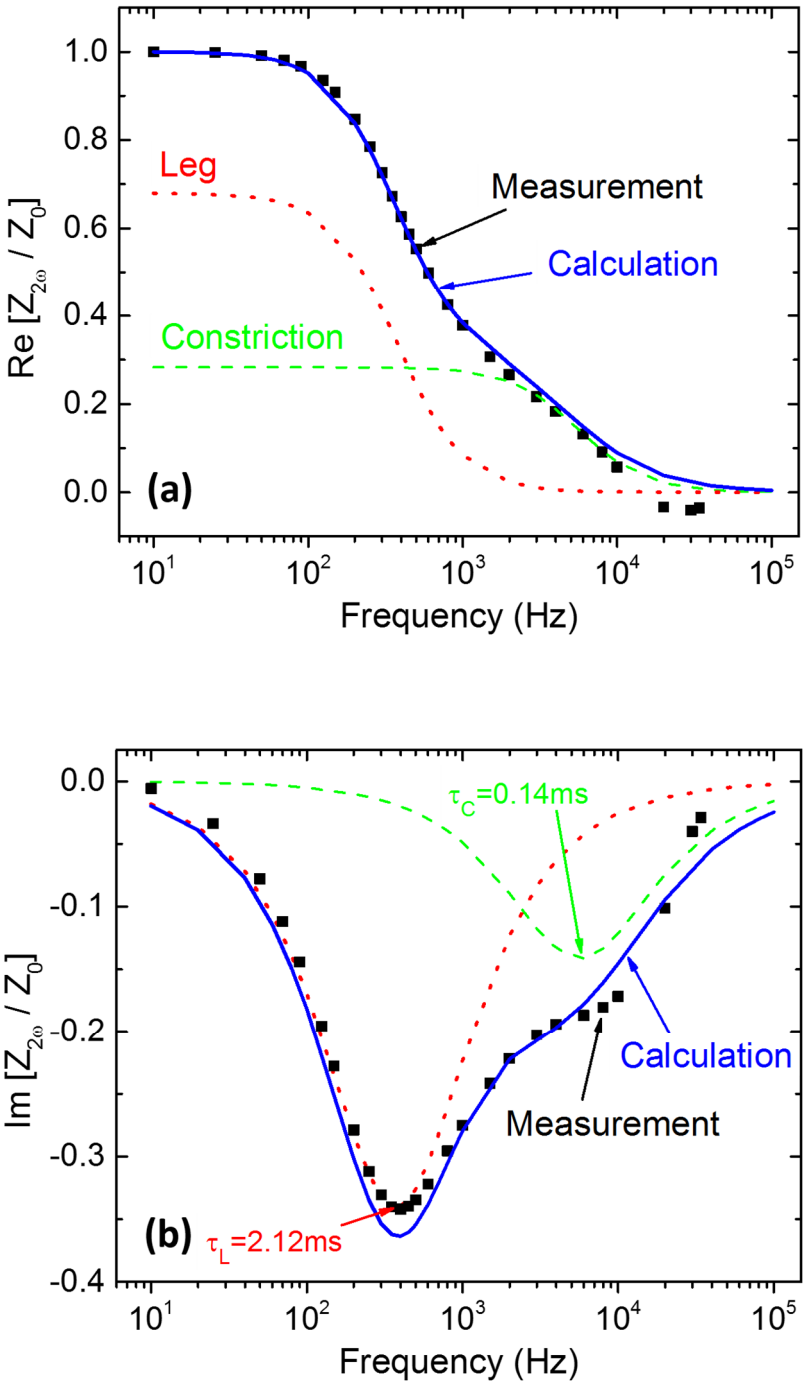

Figure 3.2. Normalized (a) in-phase and (b) out-of-phase thermal transfer function of the cantilever from the experimental (square marks) and computational (solid line) results. The dashed curve and the dotted curve are associated with the RC model of the leg and the heater, respectively.

is completely diffused to the whole cantilever in a 1-D manner. However, as the frequency increases, the cantilever thermal transfer function deviates from the ac response of the suspended wire. It seems to have another first-order response superposed at high frequencies as reflected from the shoulder of the imaginary component at ~6 kHz. We believe that thermal diffusion is confined to the heater region when the cantilever is heated at high frequencies, analogous with a short suspended wire subjected to the periodic heating.

The electrothermal behavior of the cantilever that deviates from the 1-D ac response can be better understood by approximating the normalized cantilever thermal transfer function with the series connection of two lumped first-order (RC) thermal systems [55]:

$$\frac{Z_{2\omega,\text{lump}}}{Z_0} = \frac{\beta_C}{1 + j2\omega(\tau_C/10)} + \frac{1-\beta_C}{1 + j2\omega(\tau_L/10)} \tag{3.7}$$

where β_C is the ratio of the thermal resistance of the constriction region to the total thermal resistance, τ_C (τ_L) is the characteristic diffusion time of the constriction (the leg) region, and $\omega = 2\pi f$ is the operational angular frequency. It should be noted that a correction factor of 10 was considered to correlate τ_C and τ_L with the lumped approximation [55]. The lumped RC model is also plotted in Figure 3.2. By comparing the RC model with the FEA simulation, β_C is determined to be 0.29: the thermal resistance of the constriction region takes ~30% of the total thermal resistance. The 1-D approximation of β_C can be written as $\beta_C = (l/kA)_C \Big/ \left[(l/kA)_C + (l/kA)_L\right]$, where l is the length, k is the thermal conductivity, and A is the cross sectional area of each region, yielding 0.27 for the

cantilever. The good agreement of β_C between the FEA and 1-D approximation suggests that the dc thermal behavior of the cantilever is governed by 1-D heat diffusion along the cantilever length. However, the 1-D approximation may not accurately predict the ac thermal response of the cantilever. The 1-D characteristic diffusion time can be written as $\tau_{C(L)} = [4l^2/\kappa]_{C(L)}$ with κ being the thermal diffusivity, yielding $\tau_C = 0.068$ ms and $\tau_L =$ 1.82 ms. These values deviate from $\tau_C = 0.14$ ms and $\tau_L = 2.12$ ms determined by the RC model based on the FEA simulation, suggesting that a multi-dimensional model is required for the accurate ac characterization of the heated cantilever, particularly near the heater region.

Figure 3.3 compares the ac temperature distributions of the cantilever when it is operated in vacuum for four different frequencies, i.e., (a) 90 Hz, (b) 1 kHz, (c) 10 kHz and (d) 34 kHz. The input current for the FEA was 112 μA-rms without dc offset, consistent with the experimental condition. It should be noted that the periodic temperature oscillation at 2ω is expressed as $\tilde{\Theta}_{2\omega}(\mathbf{r})e^{j2\omega t}$ in the time domain, where $\tilde{\Theta}_{2\omega}(\mathbf{r})$ provides the amplitude and the phase of the temperature oscillation through $\left|\tilde{\Theta}_{2\omega}\right| = \left[\Theta_R(\mathbf{r})^2 + \Theta_I(\mathbf{r})^2\right]^{1/2}_{2\omega}$ and $\varphi = \tan^{-1}\left[\Theta_I(\mathbf{r})/\Theta_R(\mathbf{r})\right]_{2\omega}$. Thus the negative out-of-phase temperature indicates the phase lag of the ac temperature relative to the periodic heating. At lower frequencies, i.e., $f < 1/\tau_L$ (or 472 Hz), the ac temperature distribution is similar to the dc case in supplemental Fig. 3.S4, which is available under the Supplemental Data tab for this paper on the ASME Digital Collection, except there is a small out-of-phase component as can be seen at 90 Hz. However, the cantilever operation at higher frequencies over $1/\tau_C$ (or 6.7 kHz) does not provide enough time to thermally

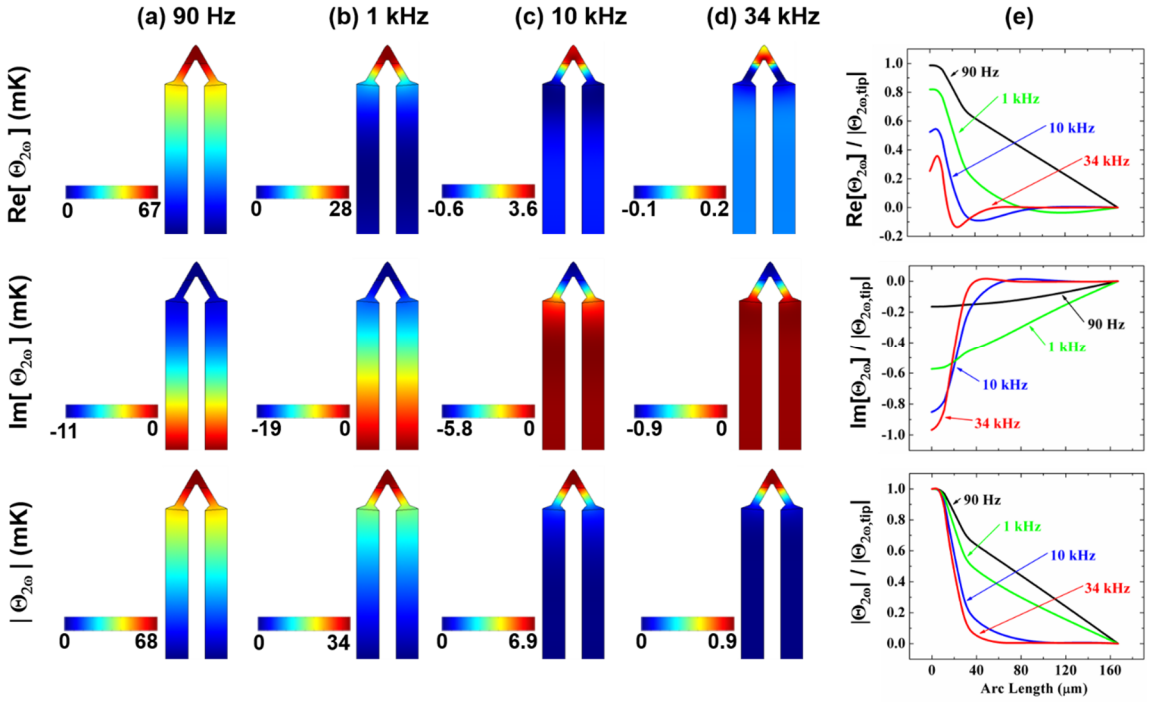

Figure 3.3. The in-phase and out-of-phase components and the magnitude of the ac temperature distributions of the cantilever under the periodic heating operation in vacuum at various frequencies: (a) 90 Hz, (b) 1 kHz, (c) 10 kHz, and (d) 34 kHz. (e) The normalized temperature distributions along the centerline of the cantilever for different frequencies. They are normalized by the magnitude of the tip temperature at each frequency.

respond to the periodic heating, leading to the temperature oscillation confined within the heater region with smaller amplitudes for both in-phase and out-of-phase components. In addition, as can be seen in Fig. 3.3(e), the ac temperature response becomes more out of phase as the frequency increases. The reduction of the effective ac heating area under the high-frequency operation is a unique feature and might be beneficial when the cantilever is to be used for local measurement of temperature and possibly thermophysical properties, as harmonic voltage signals at high frequencies may reflect the thermal responses only around the tip area.

We also calculated the ac temperature distribution of the cantilever in the quiescent air: see Fig. 3.4. While the overall trend is very similar to the vacuum case, heat loss to the air yields a lower temperature rise of the cantilever as manifested by the scale bars in Figs. 3.3 and 3.4. The temperature difference between the vacuum and the air cases becomes smaller as the frequency increases, indicating that the air also cannot respond to the periodic heating fast enough, and only the air near the cantilever dissipates heat at high frequencies over 10 kHz. At 34 kHz, for example, the heat penetration depth in the air is ~1 μm away from the cantilever heater. The heat loss to air affects the thermal transfer functions of the cantilever, as shown in Fig. 3.5. At frequencies below ~300 Hz, the cantilever thermal transfer function in the air is approximately 80% of the vacuum case: ~20% smaller temperature rise is expected at the cantilever heater due to heat loss in the air. The dip position of the out-of-phase thermal transfer function also shifts to a high frequency by ~100 Hz, indicating that τ_L decreases by ~0.45 ms due to the presence of the air. However, the thermal transfer functions for the air and the vacuum cases get closer as the frequency increases, which is consistent with the ac temperature distributions in Figs. 3.3 and 3.4.

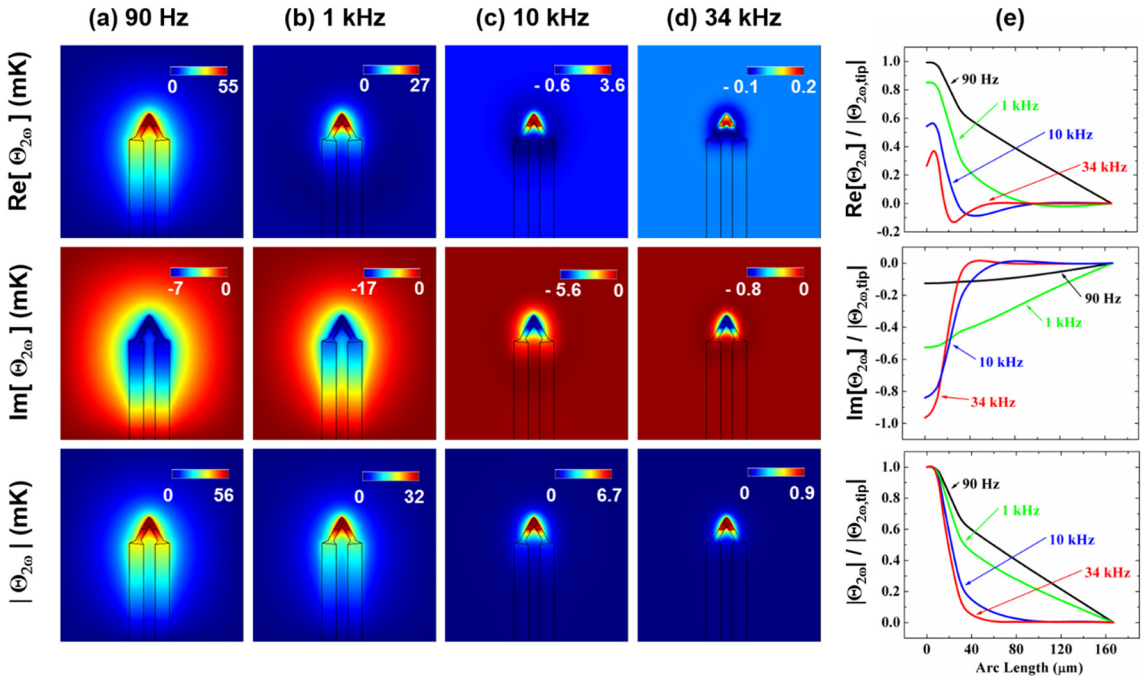

Figure 3.4. The in-phase and out-of-phase components and the magnitude of the ac temperature distributions of the cantilever under the periodic heating operation in air at various frequencies: (a) 90 Hz, (b) 1 kHz, (c) 10 kHz, and (d) 34 kHz. (e) The normalized temperature distributions along the centerline of the cantilever for different frequencies.

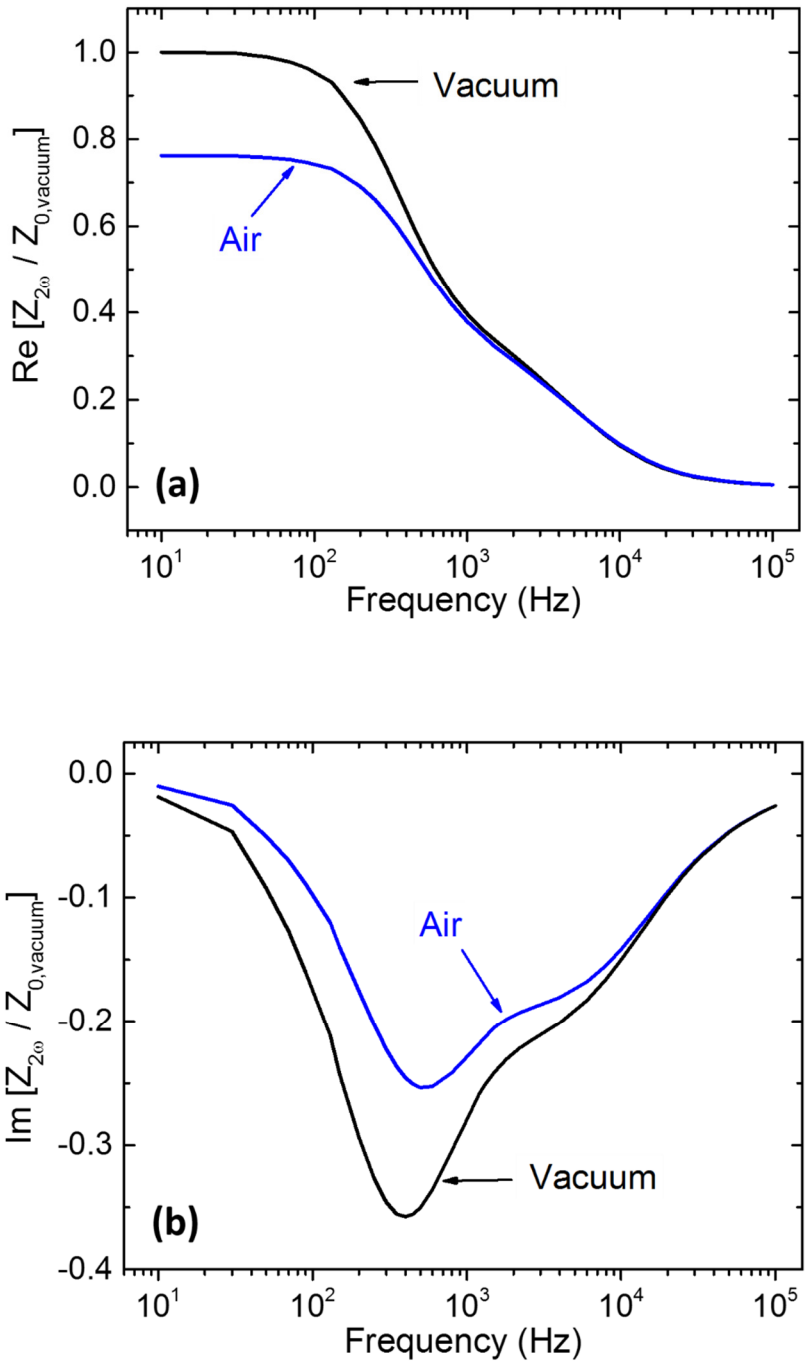

Figure 3.5. (a) In-phase and (b) out-of-phase thermal transfer functions of the cantilever for the vacuum and the air environments. Results are normalized using the thermal resistance in vacuum. The discrepancy indicates the effect of heat conduction to the air on the ac thermoelectric behaviors of the cantilever.

The heat diffusion in air has a smaller effect on the ac electrothermal behaviors of the cantilever at high frequencies.

The frequency-dependence of heat transfer in air can be further examined by calculating the frequency-dependent heat transfer coefficient. Heat transfer at the cantilever surface $(\mathbf{r}_b)$ in the frequency domain can be written as

$$-k_i \nabla \tilde{\Theta}_{n\omega}(\mathbf{r}_b) = \tilde{h}_{n\omega,i} \tilde{\Theta}_{n\omega}(\mathbf{r}_b) \tag{3.8}$$

where $\tilde{h}_{n\omega,i} = [h_R + jh_I]_i$ is the complex heat transfer coefficient at the *i*-th component. In the present study, heat transfer coefficients for the leg and the constriction regions were taken into account. The frequency-dependence of the complex heat transfer coefficient is modeled as

$$\tilde{h} = (h_0 + h_{n\omega} f^{0.5}) + jh_{n\omega} f^{0.5} \tag{3.9}$$

based on the analytical solution of heat conduction from a periodic point heat source in an infinite solid [56]. This boundary condition was implemented to the cantilever model without the environment box, and the complex heat transfer coefficient of air was extracted by comparing the thermal transfer functions calculated for the air box model and the no-box model. As shown in supplemental Fig. 3.S5, which is available under the Supplemental Data tab for this paper on the ASME Digital Collection, the computed cantilever thermal transfer functions with and without the air box are in excellent agreement within 0.1%. Figure 3.6 shows the magnitude and phase of the complex heat transfer coefficients for the

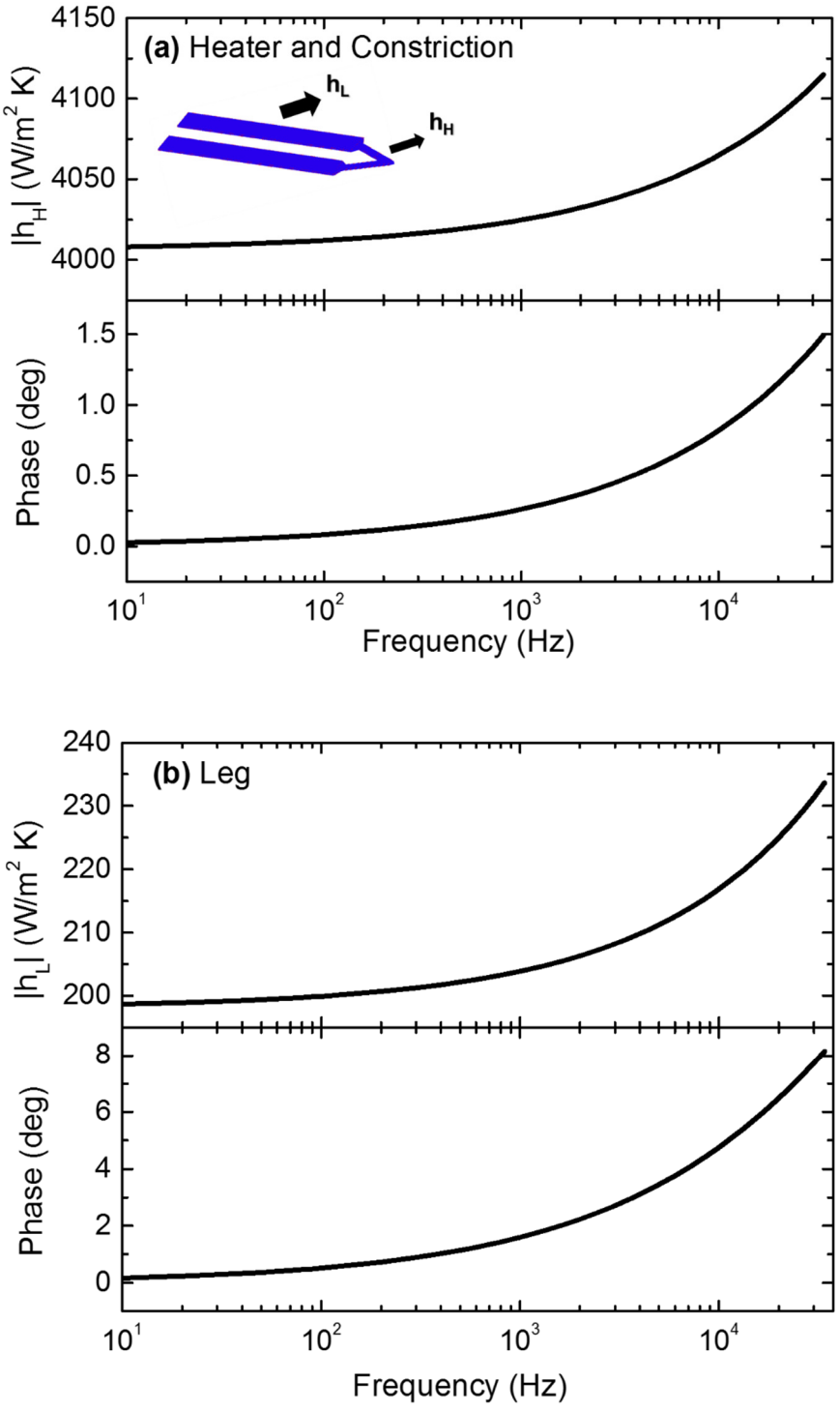

Figure 3.6. The magnitude and phase of the complex heat transfer coefficient for the (a) constriction region and (b) leg region. Both magnitude and phase increase as the frequency increases, indicating that the thermal response of the air is confined to the cantilever surface and becomes more out-of-phase.

constriction region and the leg region. The dc heat transfer coefficient of the heater is approximately 4000W/m^2 K in the low-frequency region, which is consistent with Ref. [54]. The heat transfer coefficient of the leg region is one order of magnitude smaller than that of the heater region due to the relatively larger surface area of the leg region. As the frequency increases, the magnitude and the phase of both heat transfer coefficients increase. This trend indicates that the air temperature gradient at the wall becomes steeper and more out-of-phase as the frequency increases. The air conduction at the leg region is more sensitive to the frequency than that in the heater region. The heat transfer coefficient of the leg region changes by ~15% as the frequency changes from 10 Hz to 34 kHz, while that of the heater changes by only ~2.5% in the same frequency range. This is the first demonstration of the frequency-dependent heat transfer coefficient and its effects on the transient behaviors of a heated cantilever under periodic heating. The computational cost can be drastically reduced by using the frequency-dependent heat transfer coefficient: when the 53 frequency points were calculated from 10 Hz to 34 kHz with the same computing power, the no-box simulation took around 30 minutes while the air box simulation took approximately four hours. We believe that the same scheme can be used to predict the ac thermal response of general microdevices operating in air.

The obtained thermal transfer function of the cantilever motivates further examination of the heater design and its effect on the ac electrothermal characteristics of the cantilever. Figure 3.7(a) shows the effects of the heater size on the in-phase and out-of-phase thermal transfer functions in vacuum, where the inset illustrates relative heater sizes to the actual heater under consideration. For ease of comparison, thermal transfer functions were normalized with the thermal resistance at the 100% heater size for comparison. The thermal

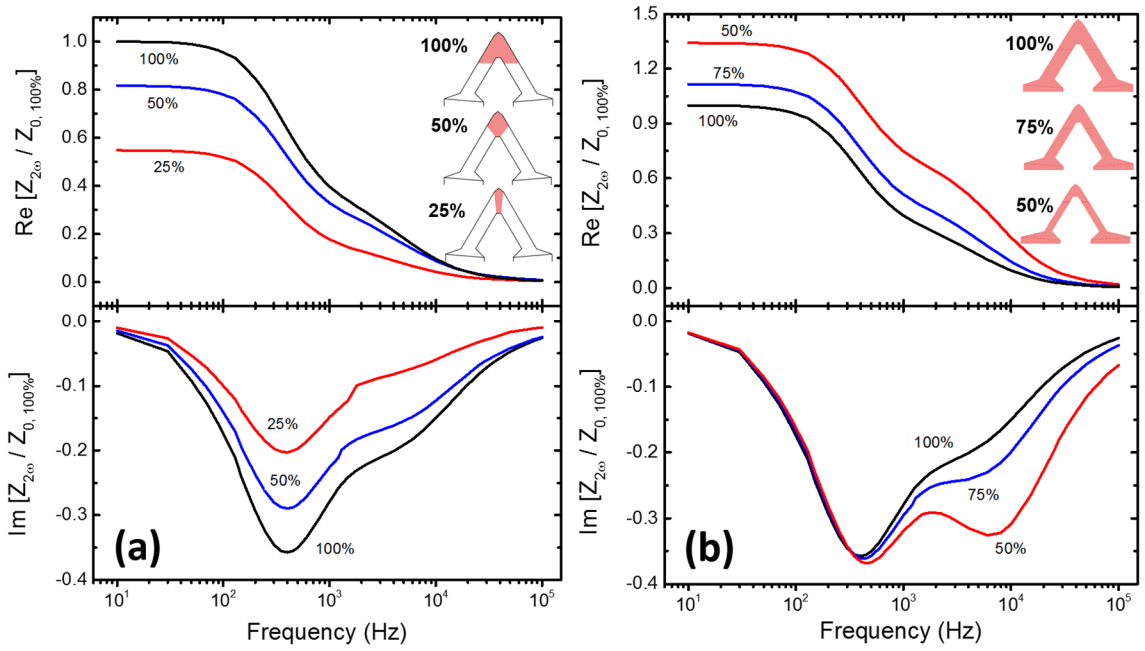

Figure 3.7. (a) The effect of the heater size to the in-phase and out-of-phase thermal transfer functions of the cantilever. The inset images illustrate different heater sizes used in the analysis. The number below each image is the percentage of the heater size as compared to the original cantilever design. (b)The effect of the constriction width to the in-phase and out-of-phase thermal transfer functions of the cantilever. The inset images illustrate different constriction widths used in the analysis. The number below each image is the percentage of the constriction width as compared to the original cantilever design. The constriction width significantly affects the high-frequency behaviors where the heater plays a dominant role.

transfer function decreases as the heater size decreases, indicating that more power is required to obtain the same ac temperature rise in a smaller heater. However, the thermal transfer function spectrum does not uniformly decrease with the heater size. The thermal transfer function at higher frequencies, corresponding to the heater-dominant frequency range, decreases more drastically than the thermal transfer function at frequencies below ~400 Hz as the heater size decreases. This is a further evidence that the heater plays a dominant role in the ac response of the cantilever at high frequencies. We also conducted the design analysis of the constriction width by comparing the thermal transfer functions in vacuum, as shown in Fig. 3.7(b). Again, thermal transfer functions were normalized with the thermal resistance at the 100% constriction width. The reduction of the constriction width increases the overall in-phase thermal transfer function, mainly due to the shrink of the cross-sectional area for heat conduction. On the other hand, the out-of-phase thermal transfer function below ~400 Hz does not change as the constriction width increases. The more prominent effect of the constriction width can be observed in the out-of-phase thermal transfer function at high frequencies. As the constriction width shrinks from 100% to 50%, for example, the shoulder of the out-of-phase thermal transfer function at ~3 kHz shifts and forms a dip at ~6 kHz. A narrow heater makes the role of the heater more dominant in the ac thermal response of the cantilever at high frequencies.

It should be noted that the thermal transfer function spectrum of the 50% constriction case is similar to that of the doped-Si nanoheater cantilever in Ref. [50], where the high-frequency dip in the out-of-phase curve is bigger than the main dip in the low-frequency region. From Fig. 3.7, it is clear that the observed ac behavior of the nanoheater cantilever is the result of the narrow constriction rather than the reduced heater size.

3.6 Conclusion

The present study reports the frequency-dependent electrothermal characteristics of a freestanding doped-silicon heated microcantilever operating under periodic joule heating. The frequency-domain FEA was implemented to compute the steady periodic temperature oscillation of the cantilever and to obtain the corresponding thermal transfer function in the full operation frequency range. From a comparison with experimental measurement, the computed thermal transfer function of the cantilever agrees very well with 2.4% and 6.1% deviations for in-phase and out-of-phase components, respectively. We also computed the thermal transfer function of the cantilever suspended in air to demonstrate the frequency-dependence of the air heat conduction and its effect to the ac responses of the cantilever. As the frequency increases, heat is diffused into the air with a smaller penetration depth, increasing the magnitude and the phase of the effective heat transfer coefficient of the air. Since the cantilever response at high frequencies is dominated by the heater region, the effects of the heater size and the constriction width to the thermal transfer function were conducted. The design analysis revealed that the constriction width is a predominant geometrical factor in altering the high-frequency electrothermal behaviors of the cantilever. Although this work focused on the ac electrothermal responses of a doped-Si heated microcantilever probe, the developed frequency-domain FEA scheme and the obtained results are generally applicable to the ac electrothermal characterizations of many other microelectromechanical devices.

3.7 Acknowledgement

This work was supported by the National Science Foundation (CBET-1403084) and the National Research Foundation of Korea funded by the Ministry of Science, ICT & Future Planning (NRF-2014R1A2A1A11053283). The authors thank Prof. William P. King at the University of Illinois at Urbana Champaign for providing doped-Si heated cantilevers for this research. SH and KP acknowledge the startup support at the University of Utah, including the support of the Center for High-Performance Computing (CHPC).

3.8 Supplemental Information

3.8.1. Cantilever Thickness

For cantilever thickness measurement 10 SEM images from different sections of the cantilever are taken and the average thickness is used as a thickness estimation and used in the modeling. A few of these SEM images are shown in Figure 3.S1(a). From the measured cantilever thicknesses at different positions, we took an average to use it for the FEA. The averaged cantilever thickness from the SEM images is 1.33 μm. We also conducted a simple FEA to calculate the resonance frequency of the cantilever with the measured thickness. The calculated resonance frequency is 83.3 kHz, which is in a good agreement with the measurement: see Figure 3.S1(b).

3.8.2. Doping Concentration

Doping profile across the cantilever thickness is not uniform and is different within the low-doped and high-doped regions, i.e. the heater and the legs regions. Figure 3.S2 shows the depth-wise doping profiles for heater and leg regions, respectively, which were

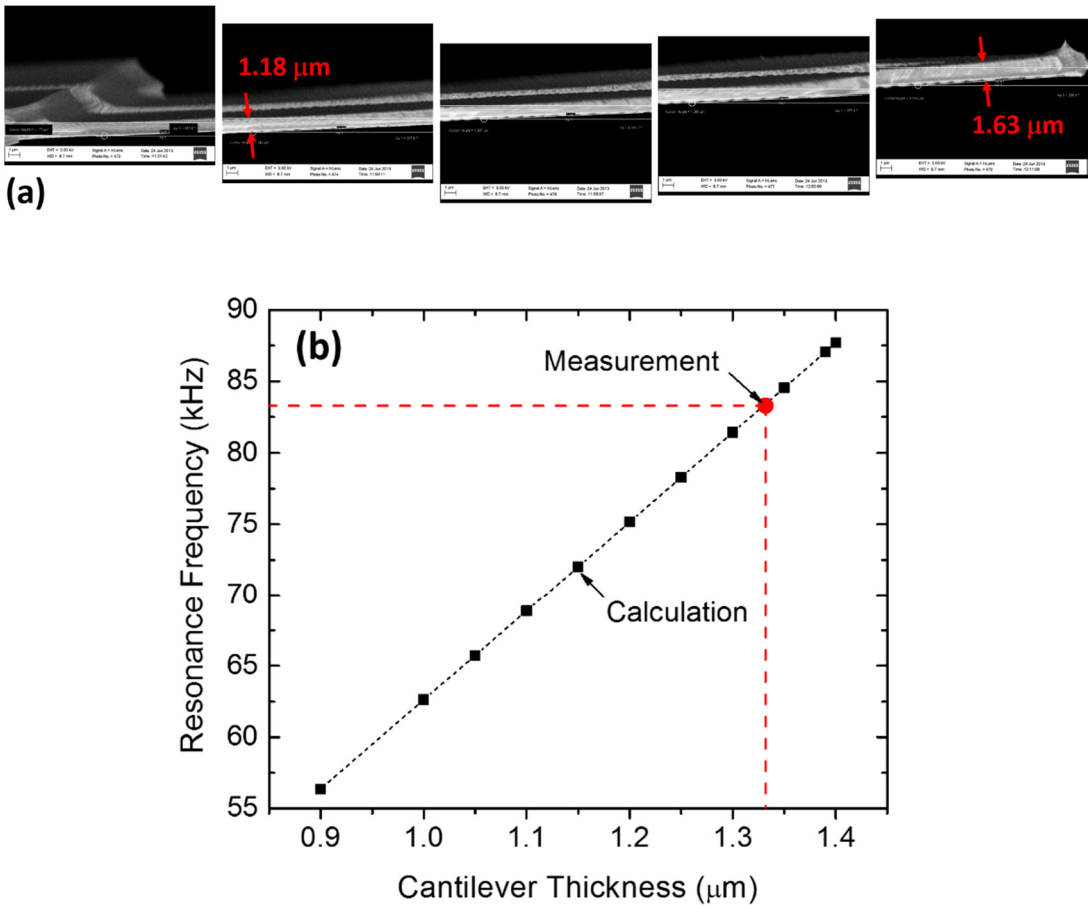

Figure. 3.S1. Shows (a) SEM images of side view of the heated cantilever (b) The resonant frequency of the cantilever as a function of the thickness. From the comparison with the measurement, the cantilever thickness estimation agrees well with thickness measured from SEM images (1.33μm).

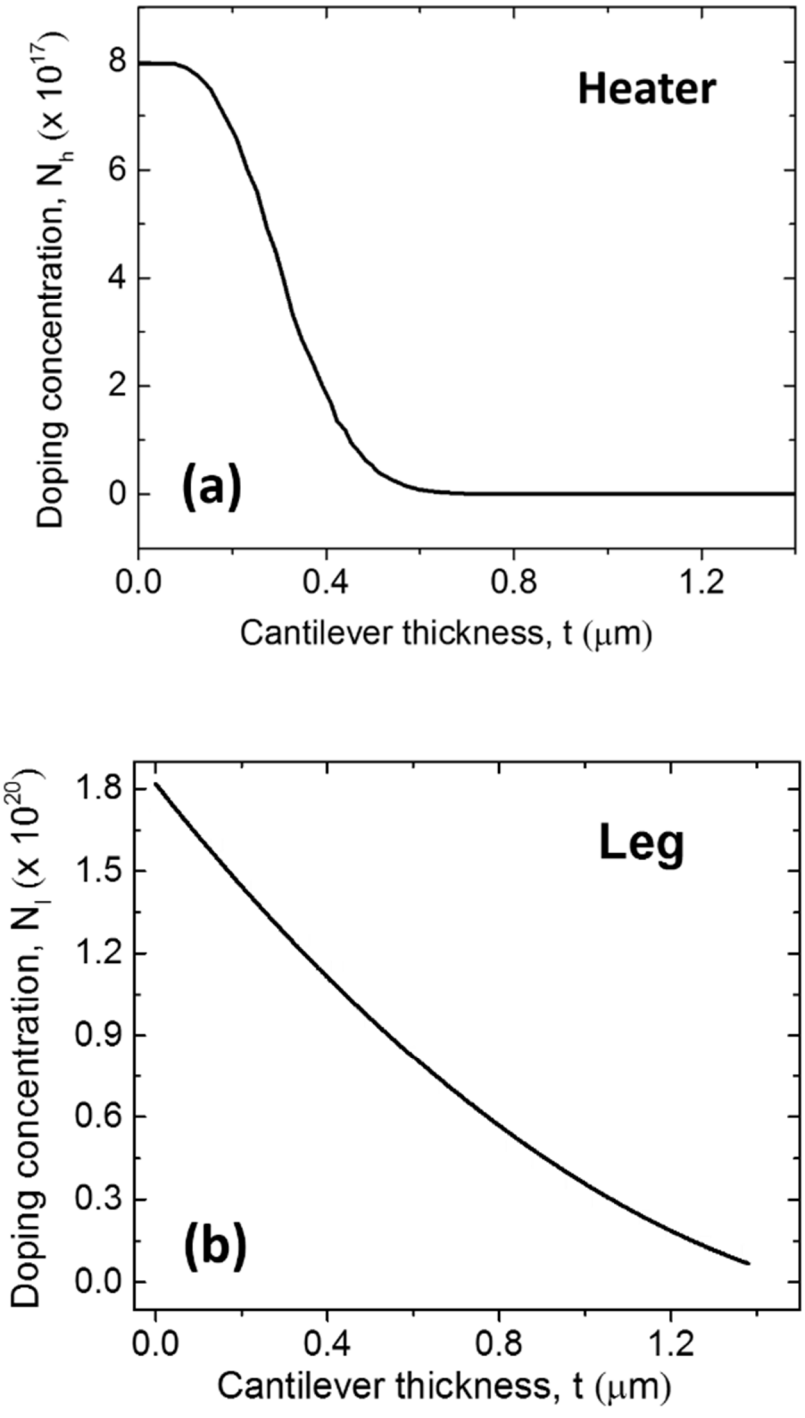

Figure. 3.S2. Shows (a) Doping profile across the heater thickness when the computed TCR matches with the measured value of $(1.77\pm0.02)\times10^{-3}$ K^{-1}. (b) Doping profile across the legs.

obtained from the Ssuprem3 simulation based on the design parameters.

3.8.3. Convergence Study

The convergence of the problem is considered by refining cantilever mesh size from total of 700 to ~675,000 finite elements. The solution is assumed to be converged when changes in maximum thermal transfer function is less than 0.03%. This is achievable using mesh size of 70,000 elements (Figure 3.S3). Comparing results from 70,000 mesh size with 675,000 elements gives us a 0.03% error while the computational time is over 20 times longer for the 675,000 case. The inset in Figure 3.S3 shows the meshed cantilever around the constriction and the heater region.

3.8.4. Temperature Coefficient of Resistivity (TCR) and DC Modeling

We calculated the electrical resistance of the cantilever suspended in vacuum for different base temperatures from 300 K to 310 K and fitted the calculated values with the measurement by adjusting N_h (0). The result is shown in Figure 3.S4(a) with the normalized cantilever resistance, $[R(T) - R_0] / R_0$, where R_0 is the cantilever resistance at room temperature. When N_h (0) is 7.96×10^{17} cm^{-3}, the FEA result provides a good agreement with the measurement within 1 % error. The corresponding temperature coefficient of resistivity (TCR) of the cantilever is estimated to be $(1.77\pm0.02)\times10^{-3}$ K^{-1} at room temperature. Figure 3.S4(b) shows the calculated dc temperature distribution of the cantilever suspended in the air when a 0.53 V dc voltage is applied to the cantilever. The dc temperature rise ΔT_{DC} is ~6 K at the tip position of the heater region and decreases along the legs. The temperature distribution reveals the basic thermal behavior of the

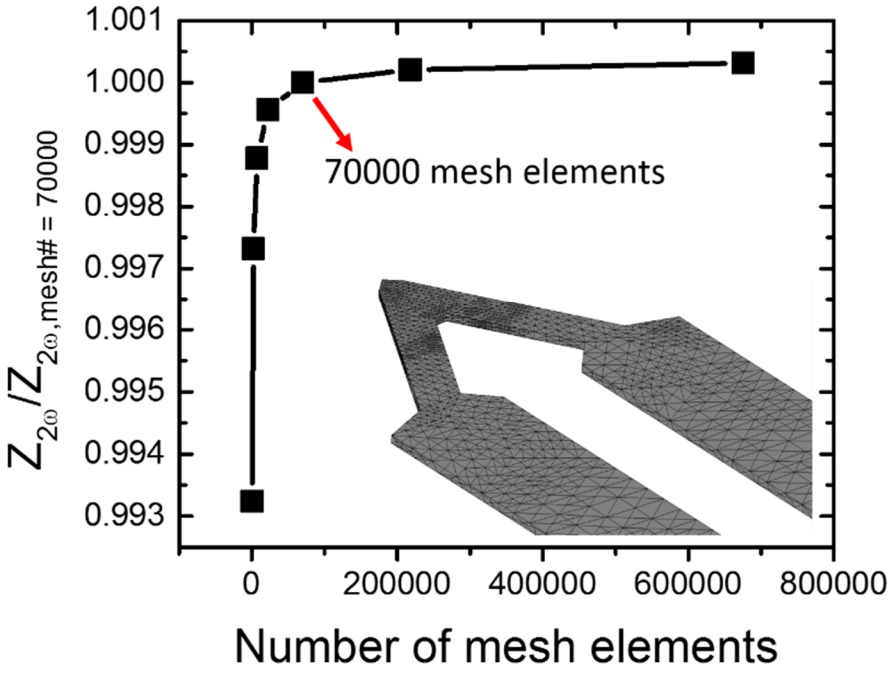

Figure. 3.S3. Convergence study as a function of cantilever mesh size with the meshed cantilever around heater and the constriction region.

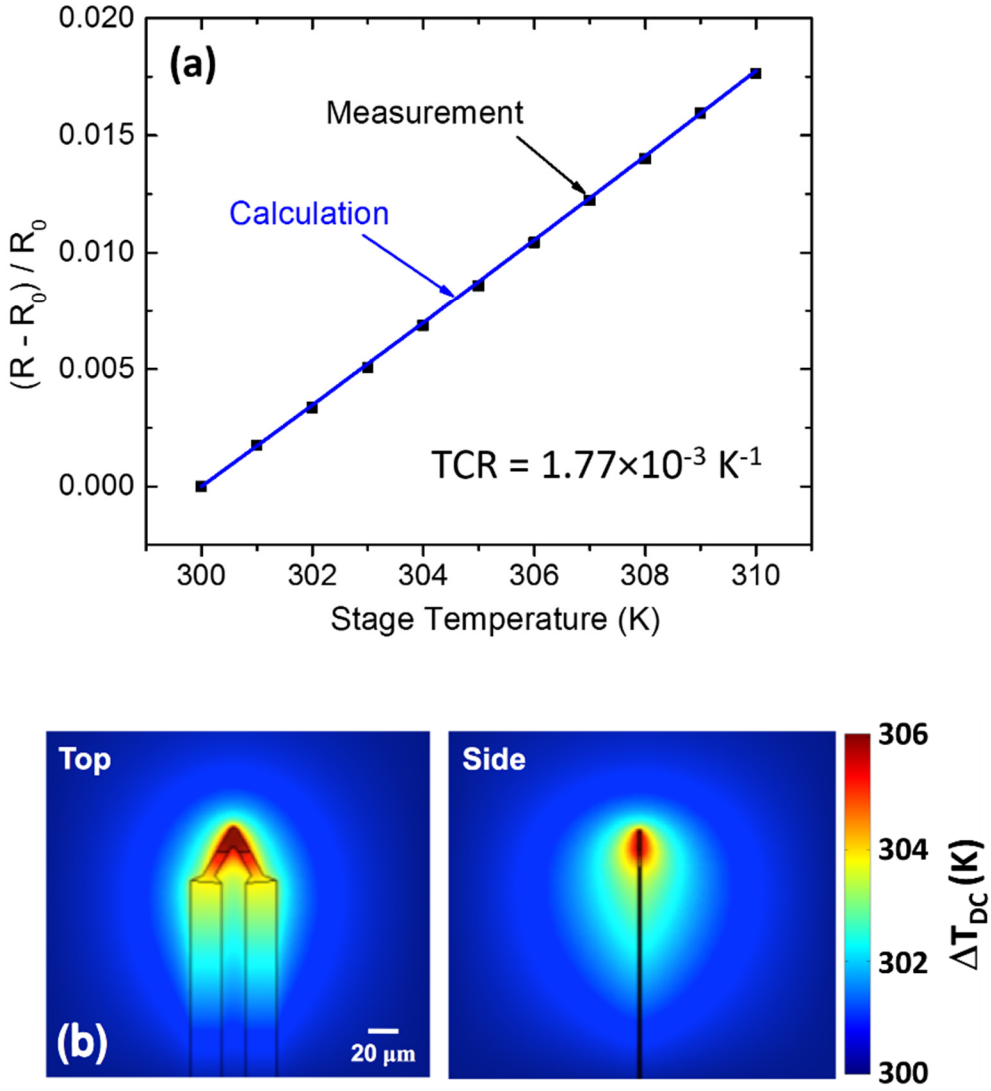

Figure. 3.S4. Shows (a) The nondimensional cantilever resistance as a function of temperature. (b) Temperature distribution of the cantilever under the steady-state heating at 0.53 V and 0.26 mA (or 0.14 mW), viewed from the top (left) and the side (right).

cantilever, showing a sharp temperature increase in the heater region. The effective heated zone in the air is formed within ~20 μm off the heater due to its low thermal conductivity.

3.8.5. Box Versus No-Box

The results of the effort to streamline the FEA model are shown in Figure 3.S5. It compares the real and imaginary thermal transfer functions with and without an air box. By removing the air box, the number of mesh elements is greatly reduced, which will reduce the computation time. However, in order to remove the box, the heat transfer to the air must be accounted for. The manner in which this was done is explained in the Results and Discussion section. From Figs. 3.S5(a) and (b), the no box model shows nearly perfect agreement with the box case. Therefore, the no box case is a valid model that can yield the same results as the box case. This is important because the no box case reduced computation time from 4 hours to 30 minutes for a full frequency sweep. The massive time savings means that more simulations can be run more quickly resulting in a more in depth understanding of the cantilever system. Also, it means that thermal properties can be extrapolated by making matching model results to experimental data more practical. With a 4 hour run time for the air box case, signal matching would take months as opposed to days or weeks with the no box case.

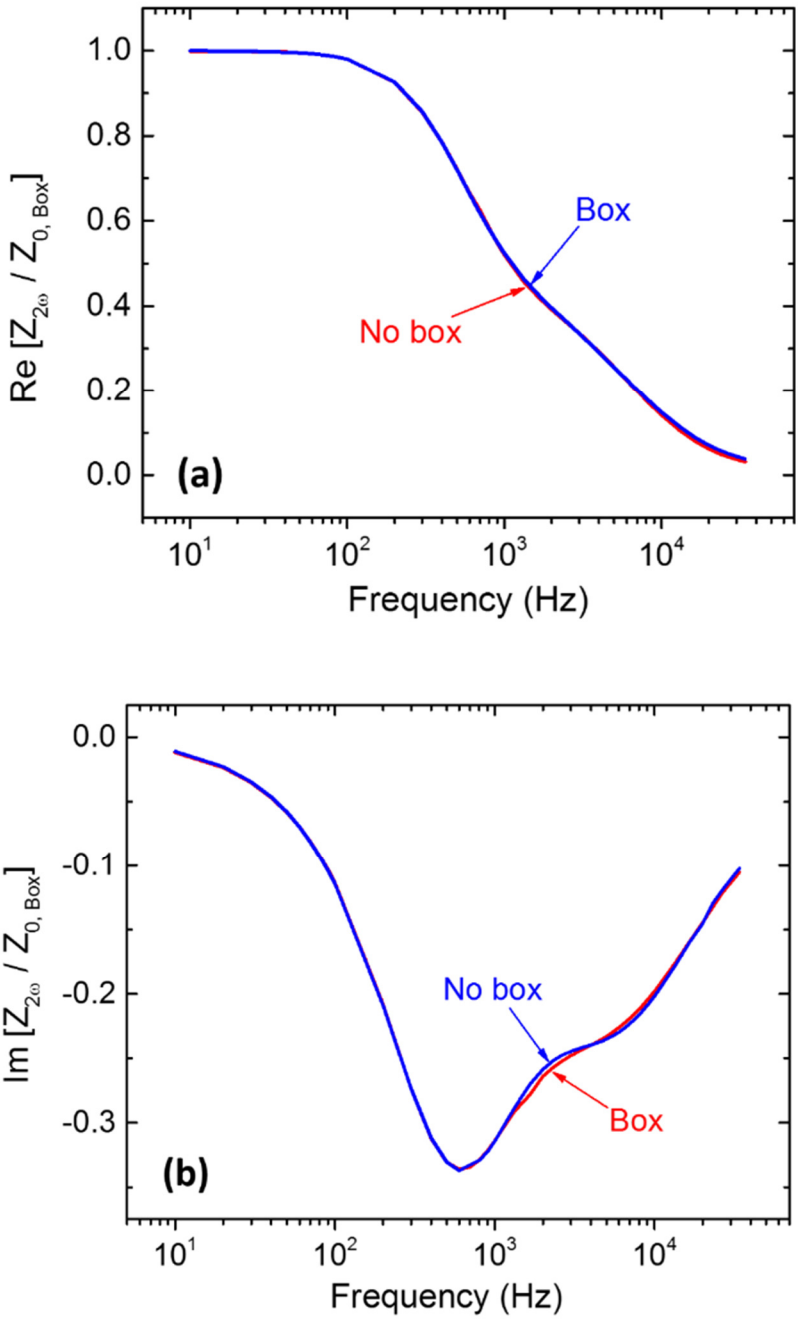

Figure. 3.S5. Comparison of the 3w voltage signal as a function of frequency from the FEA model with and without the air box for (a) the in-phase and (b) the out-of-phase signals. Both models were for an input current of 112 μA-rms.

3.9 References

[1] Majumdar, A., Lai, J., Chandrachood, M., Nakabeppu, O., Wu, Y., and Shi, Z., 1995, Thermal Imaging by Atomic Force Microscopy Using Thermocouple Cantilever Probes, Rev. Sci. Instrum., 66(6), pp. 3584–3592.

[2] Samson, B., Aigouy, L., Löw, P., Bergaud, C., Kim, B. J., and Mortier, M., 2008, AC Thermal Imaging of Nanoheaters Using a Scanning Fluorescent Probe, Appl. Phys. Lett., 92(2), p. 23101.

[3] Sadat, S., Tan, A., Chua, Y., and Reddy, P., 2010, Nanoscale Thermometry Using Point Contact Thermocouples, Nano Lett., 10(7), pp. 2613–2617.

[4] Kim, K., Chung, J., Hwang, G., Kwon, O., and Lee, J., 2011, Quantitative Measurement With Scanning Thermal Microscope by Preventing the Distortion Due to the Heat Transfer Through the Air, ACS Nano, 5(11), pp. 8700–8709.

[5] Fletcher, P., Lee, B., and King, W. P., 2011, Thermoelectric Voltage at a Nanometer-Scale Heated Tip Point Contact, Nanotechnology, 23(3), p. 35401.

[6] Kim, K., Jeong, W., Lee, W., and Reddy, P., 2012, Ultra-High Vacuum Scanning Thermal Microscopy for Nanometer Resolution Quantitative Thermometry, ACS Nano, 6(5), pp. 4248–57.

[7] King, W. P., Saxena, S., Nelson, B. a, Weeks, B. L., and Pitchimani, R., 2006, Nanoscale Thermal Analysis of an Energetic Material, Nano Lett., 6(9), pp. 2145–9.

[8] Nelson, B. a., and King, W. P., 2007, Measuring Material Softening With Nanoscale Spatial Resolution Using Heated Silicon Probes, Rev. Sci. Instrum., 78(2), p. 23702.

[9] Jesse, S., Nikiforov, M. P., Germinario, L. T., and Kalinin, S. V., 2008, Local Thermomechanical Characterization of Phase Transitions Using Band Excitation Atomic Force Acoustic Microscopy With Heated Probe, Appl. Phys. Lett., 93(7), p. 73104.

[10] Nikiforov, M. P., Gam, S., Jesse, S., Composto, R. J., and Kalinin, S. V., 2010, Morphology Mapping of Phase-Separated Polymer Films Using Nanothermal Analysis, Macromolecules, 43(16), pp. 6724–6730.

[11] Zhang, Y., Dobson, P. S., and Weaver, J. M. R., 2011, Batch Fabricated Dual Cantilever Resistive Probe for Scanning Thermal Microscopy, Microelectron. Eng., 88(8), pp. 2435–2438.

[12] Kim, K. J., Park, K., Lee, J., Zhang, Z. M., and King, W. P., 2007, Nanotopographical Imaging Using a Heated Atomic Force Microscope Cantilever Probe, Sensors Actuators A Phys., 136(1), pp. 95–103.

[13] Park, K., Lee, J., Zhang, Z. M., and King, W. P., 2007, Topography Imaging With a Heated Atomic Force Microscope Cantilever in Tapping Mode, Rev. Sci. Instrum., 78(4), p. 43709.

[14] Somnath, S., Liu, J. O., Bakir, M., Prater, C. B., and King, W. P., 2014, Multifunctional Atomic Force Microscope Cantilevers With Lorentz Force Actuation and Self-Heating Capability., Nanotechnology, 25(39), p. 395501.

[15] Kim, H. J., Moldovan, N., Felts, J. R., Somnath, S., Dai, Z., Jacobs, T. D. B., Carpick, R. W., Carlisle, J. a, and King, W. P., 2012, Ultrananocrystalline Diamond Tip Integrated Onto a Heated Atomic Force Microscope Cantilever., Nanotechnology, 23, p. 495302.

[16] Somnath, S., and King, W. P., 2014, An Investigation of Heat Transfer Between a Microcantilever and a Substrate for Improved Thermal Topography Imaging, Nanotechnology, 25, p. 365501.

[17] O'Callahan, B. T., Lewis, W. E., Jones, A. C., and Raschke, M. B., 2014, Spectral Frustration and Spatial Coherence in Thermal Near-Field Spectroscopy, Phys. Rev. B, 89(24), p. 245446.

[18] Jones, A. C., and Raschke, M. B., 2012, Thermal Infrared Near-Field Spectroscopy, Nano Lett., 12(3), pp. 1475–81.

[19] Babuty, A., Joulain, K., Chapuis, P.-O., Greffet, J.-J., and De Wilde, Y., 2013, Blackbody Spectrum Revisited in the Near Field, Phys. Rev. Lett., 110(14), p. 146103.

[20] Bozec, L., Hammiche, A., Pollock, H. M., Conroy, M., Chalmers, J. M., Everall, N. J., and Turin, L., 2001, Localized Photothermal Infrared Spectroscopy Using a Proximal Probe, J. Appl. Phys., 90, pp. 5159–5165.

[21] Hammiche, A., Bozec, L., German, M. J., Chalmers, J. M., Everall N. J., Graham, P., Reading, M., Grandy, D. B., Martin, F. L., and Pollock, H. M., 2004, Mid-Infrared Microspectroscopy of Difficult Samples Using Near-Field Photothermal Microspectroscopy, Spectroscopy, 19(2), pp. 20–42.

[22] Reading, M., Grandy, D., Hammiche, a., Bozec, L., and Pollock, H. M., 2002, Thermally Assisted Nanosampling and Analysis Using Micro-IR Spectroscopy and Other Analytical Methods, Vib. Spectrosc., 29, pp. 257–260.

[23] Binnig, G., Despont, M., Drechsler, U., Häberle, W., Lutwyche, M., Vettiger, P., Mamin, H. J., Chui, B. W., and Kenny, T. W., 1999, Ultrahigh-Density Atomic Force Microscopy Data Storage With Erase Capability, Appl. Phys. Lett., 74(9), pp. 1329–1331.

[24] King, W. P., Kenny, T. W., Goodson, K. E., Member, A., Cross, G. L. W., Despont, M., Dürig, U. T., Rothuizen, H., Binnig, G., and Vettiger, P., 2002, Design of

Atomic Force Microscope Cantilevers for Combined Thermomechanical Writing and Thermal Reading in Array Operation, 11(6), pp. 765–774.

[25] Sunden, E. O., Wright, T. L., Lee, J., King, W. P., and Graham, S., 2006, Room-Temperature Chemical Vapor Deposition and Mass Detection on a Heated Atomic Force Microscope Cantilever, Appl. Phys. Lett., 88(3), p. 33107.

[26] Lee, J., Liao, A., Pop, E., and King, W. P., 2009, Electrical and Thermal Coupling to a Single-Wall Carbon Nanotube Device Using an Electrothermal Nanoprobe, Nano Lett., 9(4), pp. 1356–61.

[27] Wei, Z., Wang, D., Kim, S., Kim, S.-Y., Hu, Y., Yakes, M., Laracuente, A., Dai, Z., Marder, S., Berger, C., King, W., Heer, W., Sheehan, P., and Riedo, E., 2010, Nanoscale Tunable Reduction of Graphene Oxide for Graphene Electronics, Science, 328(5984), pp. 1373–1376.

[28] Sheehan, P. E., Whitman, L. J., King, W. P., and Nelson, B. A., 2004, Nanoscale Deposition of Solid Inks via Thermal Dip Pen Nanolithography, Appl. Phys. Lett., 85(9), pp. 1589–1591.

[29] Yang, M., Sheehan, P. E., King, W. P., and Whitman, L. J., 2006, Direct Writing of a Conducting Polymer With Molecular-Level Control of Physical Dimensions and Orientation, J. Am. Chem. Soc., 128(21), pp. 6774–5.

[30] Lee, W. K., Dai, Z., King, W. P., and Sheehan, P. E., 2010, Maskless Nanoscale Writing of Nanoparticle-Polymer Composites and Nanoparticle Assemblies Using Thermal Nanoprobes, Nano Lett., 10(1), pp. 129–33.

[31] Wang, D., Kodali, V. K., Underwood II, W. D., Jarvholm, J. E., Okada, T., Jones, S. C., Rumi, M., Dai, Z., King, W. P., Marder, S. R., Curtis, J. E., and Riedo, E., 2009, Thermochemical Nanolithography of Multifunctional Nanotemplates for Assembling Nano-Objects, Adv. Funct. Mater., 19(23), pp. 3696–3702.

[32] Nelson, B. A., King, W. P., Laracuente, a. R., Sheehan, P. E., and Whitman, L. J., 2006, Direct Deposition of Continuous Metal Nanostructures by Thermal Dip-Pen Nanolithography, Appl. Phys. Lett., 88(3), p. 33104.

[33] Gotsmann, B., and Dürig, U., 2004, Thermally Activated Nanowear Modes of a Polymer Surface Induced by a Heated Tip, Langmuir, 20(4), pp. 1495–500.

[34] Szoszkiewicz, R., Okada, T., Jones, S. C., Li, T.-D., King, W. P., Marder, S. R., and Riedo, E., 2007, High-Speed, Sub-15 nm Feature Size Thermochemical Nanolithography, Nano Lett., 7(4), pp. 1064–9.

[35] Fenwick, O., Bozec, L., Credgington, D., Hammiche, A., Lazzerini, G. M., Silberberg, Y. R., and Cacialli, F., 2009, Thermochemical Nanopatterning of Organic Semiconductors, Nat. Nanotechnol., 4(10), pp. 664–8.

[36] Pires, D., Hedrick, J. L., De Silva, A., Frommer, J., Gotsmann, B., Wolf, H., Despont, M., Duerig, U., and Knoll, A. W., 2010, Nanoscale Three-Dimensional Patterning of Molecular Resists by Scanning Probes, Science, 328(5979), pp. 732–735.

[37] Cahill, D. G., 1990, Thermal Conductivity Measurement From 30 to 750 K: The 3ω Method, Rev. Sci. Instrum., 61(2), pp. 802–808.

[38] Corbin, E. A., Park, K., and King, W. P., 2009, Room-Temperature Temperature Sensitivity and Resolution of Doped-Silicon Microcantilevers, Appl. Phys. Lett., 94(24), p. 243503.

[39] Lee, B., and King, W., 2012, 2-ω and 3-ω Temperature Measurement of a Heated Microcantilever, Rev. Sci. Instrum., 83(7), p. 74902.

[40] Ilic, B., Krylov, S., and Craighead, H. G., 2010, Theoretical and Experimental Investigation of Optically Driven Nanoelectromechanical Oscillators, J. Appl. Phys., 107(3), p. 034311.

[41] Ilic, B., Krylov, S., Aubin, K., Reichenbach, R., and Craighead, H. G., 2005, Optical Excitation of Nanoelectromechanical Oscillators, Appl. Phys. Lett., 86(2005), p. 193114.

[42] Mahameed, R., and Elata, D., 2005, Two-Dimensional Analysis of Temperature-Gradient Actuation of Cantilever Beam Resonators, J. Micromechanics Microengineering, 15(8), pp. 1414–1424.

[43] Zalalutdinov, M., Zehnder, A., Olkhovets, A., Turner, S., Sekaric, L., Ilic, B., Czaplewski, D., Parpia, J. M., and Craighead, H. G., 2001, Autoparametric Optical Drive for Micromechanical Oscillators, Appl. Phys. Lett., 79(5), pp. 695–697.

[44] Ratcliff, G. C., Erie, D. A., and Superfine, R., 1998, Photothermal Modulation for Oscillating Mode Atomic Force Microscopy in Solution, Appl. Phys. Lett., 72(15), pp. 1911–1913.

[45] Liu, F., De Beer, S., Van Den Ende, D., and Mugele, F., 2013, Atomic Force Microscopy of Confined Liquids Using the Thermal Bending Fluctuations of the Cantilever, Phys. Rev. E: Stat., Nonlinear, Soft Matter Phys., 87, pp. 42–47.

[46] Ilic, B., Yang, Y., and Craighead, H. G., 2004, Virus Detection Using Nanoelectromechanical Devices, Appl. Phys. Lett., 85(13), pp. 2604–2606.

[47] Ilic, B., Yang, Y., Aubin, K., Reichenbach, R., Krylov, S., and Craighead, H. G., 2005, Enumeration of DNA Molecules Bound to a Nanomechanical Oscillator, Nano Lett., 5(5), pp. 925–929.

[48] Lee, J., Beechem, T., Wright, T., Nelson, B., Graham, S., and King, W., 2006, Electrical, Thermal, and Mechanical Characterization of Silicon Microcantilever

Heaters, J. Microelectromechanical Syst., 15(6), pp. 1644–1655.

[49] Lee, J., and King, W. P., 2007, Microcantilever Actuation Via Periodic Internal Heating, Rev. Sci. Instrum., 78(12), p. 126102.

[50] Dai, Z., King, W. P., and Park, K., 2009, A 100 Nanometer Scale Resistive Heater-Thermometer on a Silicon Cantilever, Nanotechnology, 20(9), p. 95301.

[51] Park, K., Lee, J., Zhang, Z. M., and King, W. P., 2007, Frequency-Dependent Electrical and Thermal Response of Heated Atomic Force Microscope Cantilevers, J. Microelectromechanical Syst, 16(2), pp. 213–222.

[52] Park, K., Marchenkov, A., Zhang, Z. M., and King, W. P., 2007, Low Temperature Characterization of Heated Microcantilevers, J. Appl. Phys., 101(9), p. 94504.

[53] Kim, J., Han, S., Walsh, T., Park, K., Lee, B. J., King, W. P., and Lee, J., 2013, Temperature Measurements of Heated Microcantilevers Using Scanning Thermoreflectance Microscopy, Rev. Sci. Instrum., 84(3), p. 34903.

[54] Kim, K. J., and King, W. P., 2009, Thermal Conduction Between a Heated Microcantilever and a Surrounding Air Environment, Appl. Therm. Eng., 29(8–9), pp. 1631–1641.

[55] Dames, C., and Chen, G., 2005, 1ω, 2ω, and 3ω Methods for Measurements of Thermal Properties, Rev. Sci. Instrum., 76(12), p. 124902.

[56] Carslaw, H. S., and Jaeger, J. C., 1986, *Conduction of Heat in Solids*, Oxford University Press, New York.

[57] Fortier, D., and Suzuki, K., 1976, Effect of P Donors on Thermal Phonon Scattering in SI, J. Phys. Fr., 37(2), pp. 143–147.

[58] Liu, W., and Asheghi, M., 2005, Thermal Conductivity Measurements of Ultra-Thin Single Crystal Silicon Layers, J. Heat Transf., 128(1), pp. 75–83.

[59] Touloukian, Y. S., and Buyco, E. H., 1970, *Thermophysical Properties of Matter: Specific Heat: Metallic Elements and Alloys*, IFI/Plenum, New York.

[60] Park, K., Cross, G. L., Zhang, Z. M., and King, W. P., 2008, Experimental Investigation on the Heat Transfer Between a Heated Microcantilever and a Substrate, ASME J. Heat Transfer, 130(10), p. 102401.

[61] Lee, J., Wright, T. L., Abel, M. R., Sunden, E. O., Marchenkov, A., Graham, S., and King, W. P., 2007, Thermal Conduction From Microcantilever Heaters in Partial Vacuum, J. Appl. Phys., 101(1), p. 14906.

[62] Reggiani, S., Valdinoci, M., Colalongo, L., Rudan, M., Member, S., Baccarani, G., Stricker, A. D., Illien, F., Felber, N., Fichtner, W., and Zullino, L., 2002, Electron

and Hole Mobility in Silicon at Large Operating Temperatures — Part I : Bulk Mobility, 49(3), pp. 490–499.

[63] Kuźmicz, W., 1986, Ionization of Impurities in Silicon, Solid. State. Electron., 29(12), pp. 1223–1227.

[64] Wright, T., 2005, Fabrication and Testing of Heated Atomic Force Microscope Cantilevers. M.Sc. thesis, Georgia Institute of Technology, Atlanta, GA.

CHAPTER 4

QUANTITATIVE PROBING OF TIP-INDUCED COOLING WITH A RESISTIVE NANOHEATER/THERMOMETER

Reproduced from Applied Physics Letter (2016) **109**, 253114. Quantitative Probing of Tip-Induced Local Cooling with a Resistive Nanoheater/Thermometer. Sina Hamian, Jeonghoon Yun, Inkyu Park, Keunhan Park, © owned by the authors, published by AIP Publishing, 2016, with the permission of the AIP Publishing.

4.1. Abstract

This article reports the investigation of tip-induced local cooling when an atomic force microscope (AFM) cantilever tip scans over a joule-heated Pt nanowire. We fabricated four-point-probe Pt resistive nanothermometers having a sensing area of 250nm×350nm by combining electron-beam lithography and photolithography. The electrical resistance of a fabricated nanothermometer is ~27.8Ω at room temperature and is linearly proportional to the temperature increase up to 350K. The equivalent temperature coefficient of resistance is estimated to be $(7.0 \pm 0.1) \times 10^{-4} K^{-1}$. We also joule-heated a nanothermometer to increase its sensing area temperature up to 338.5 ± 0.2K, demonstrating that the same device can be used as a nanoheater. An AFM probe tip scanning over a heated nanoheater/thermometer's sensing area induces local cooling due

to heat conduction through solid-solid contact, water meniscus, and surrounding air. The effective contact thermal conductance is 32.5±0.8nW/K. These results contribute to the better understanding of tip-substrate thermal interactions, which is the fundamental subject in tip-based thermal engineering applications.

4.2 Introduction

Over the past two decades, tip-based thermal engineering has made significant advances to enable various cutting-edge nanoscale applications, such as scanning thermal microscopy (SThM) for nanoscale thermal imaging[1–4] and analysis,[5–8] thermally-based topographic imaging,[9–11] mid-infrared nanospectroscopy,[12–14] high-density data storage,[15–18] and nanomanufacturing.[19–26] These applications have created strong demands to study the fundamentals of local thermal transport due to a tip contact. Advancements in nanothermometry have allowed the experimental studies of tip-substrate thermal transport mechanisms and local temperature distributions.[27–31] Nanothermometry techniques developed to date include near-field optical thermometry,[32] tip-enhanced Raman thermometry,[33–35] tip-based fluorescence microscopy,[36] SThM-based nanothermometry using thermocouple[4,29,37–39] or resistive[31,40,41] probes, and on-substrate thermocouple[42–44] or resistive[28,45] nanothermometry. Among different techniques, four-point-probe resistive thermometry has several advantages over other methods, such as relatively easy fabrication and instrumentation, high precision temperature measurement,[46,47] and the use of the same device as a local heater for thermophysical property measurement.[48–50] However, a relatively large sensing area is required to achieve a high temperature sensitivity for resistive thermometry. On-substrate resistive nanothermometers developed to date have

nanoscale confinement in only one direction,[28,45] which has prevented the probing of local thermal transport with a fully nanoscale spatial resolution.

In this article, we present the design, fabrication, and characterization of on-substrate platinum (Pt) resistive nanothermometers having a 250 nm × 350 nm sensing area and its use for quantitative probing of tip-substrate thermal transport. The developed nanothermometers show a linear proportionality of the electrical resistance with increasing temperature, which is a desired performance for reliable temperature measurement. In addition, we demonstrate that the device can be used as a nanoheater by increasing the input current. The resistive nanothermomer/heater is used for the experimental study of tip-induced local cooling in an atomic force microscope (AFM) platform. When an AFM microcantilever probe scans over a heated nanothermometer (or nanoheater) in contact mode, a relatively cold tip induces local cooling from a heated area. Measuring the temperature and heating power changes of the nanothermometer allows the probing of the tip-induced local cooling, from which the effective contact thermal conductance is determined.

4.3 Results and Discussion

Fig. 4.1(a) shows the schematics and scanning electron microscope (SEM) micrographs of a fabricated four-point resistive nanothermometer device. The detailed fabrication steps of the nanothermometer are provided in Fig. 4.S1 of the Supplemental Information (SI). The key of the fabrication process is to combine e-beam nanolithography and photolithography techniques to align nanopatterned Pt strips with micropatterned gold (Au) electrical leads. The Au micropatterns cover the Pt nanopatterns with an average area of 3

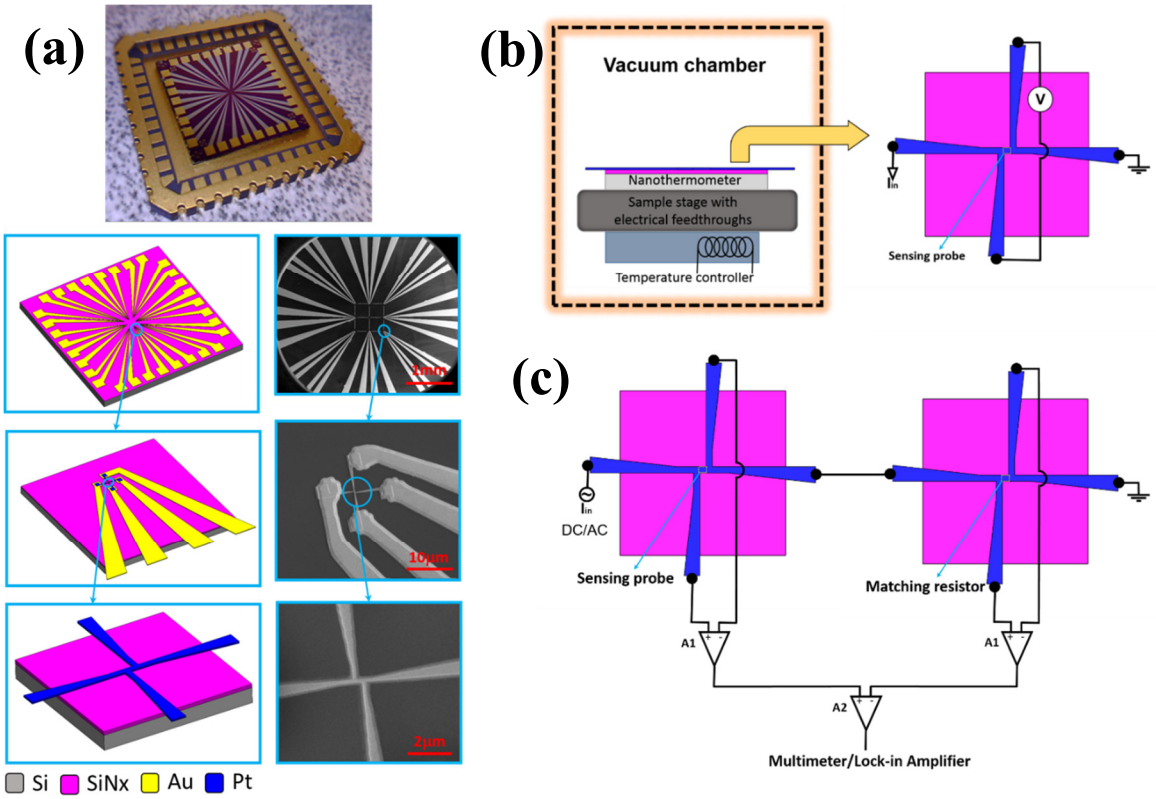

Figure 4.1. (a) Picture, schematic, and SEM images of a fabricated chip having eight independent nanothermometer/heaters. (b) Experimental setup for TCR measurement and (c) the differential scheme to isolate the signal of interest to precisely measure relative temperature change of the device.

μm × 3 μm to minimize contact electrical resistance. Pt nanowires and Au electrical leads are 40nm and 180nm thick, respectively, according to the AFM measurement shown in Figure 4.S2. Eight nanothermometers are fabricated on a 1 cm × 1 cm SiNx-on-Si chip. Adjacent nanothermometers are separated by 300μm for thermal isolation during independent measurements and to provide a suitable platform for the differential measurement scheme. The resistive sensing area is at the very center of the Pt nanowires with an area of approximately 250 nm × 350 nm, where 250 nm is the width of the Pt nanopattern and 350 nm is the length of the thermometer sensing area as measured between

the centers of the inner electrodes.

The nanothermometers were calibrated in a vacuum chamber equipped with a heater stage and electrical feedthroughs. The heater and a K-type thermocouple in the sample stage are connected to a temperature controller (Cryo-Con 22C) to feedback control the stage temperature with 50 mK accuracy. Figure 4.1(b) illustrates the experimental setup for nanothermometer calibration, where the voltage drop across the inner electrodes is measured while a constant input current of 100 μA is applied through the outer electrodes of the nanothermometer. The input current of 100 μA was carefully chosen to guarantee a stable thermometer signal without self-heating the thermometer in a vacuum condition at ~1×10^{-5} Torr. The finite element analysis (COMSOL Multiphysics) predicts the temperature increase of the sensing area to be 45mK when the input current is 100 μA (or the power dissipation of 27.8 μW) in vacuum. A compelling advantage of having multiple thermometers in one chip is to implement a differential scheme for precision measurement. Figure 4.1(c) illustrates the differential scheme, where a reference nanothermometer is connected in series with the sensing nanothermometer. Each thermometer is connected to an instrument amplifier (Analog Devices, AD524) with the gain of ×10, and their output signals are supplied to the third instrument amplifier with the gain of ×10 to yield an amplified differential signal (×100) due to a small temperature change of the sensing nanothermometer. The temperature resolution of the nanothermometer under the differential scheme can be determined by conducting a noise spectrum analysis within a small frequency range close to 0 Hz.[46] The power spectral density of the nanothermometer is shown in Figure 4.S3 in the SI for the frequency range between 0 to 0.5 Hz, from which the noise equivalent voltage is estimated to be 12.96 μV. The corresponding noise

equivalent temperature is 410mK: see the SI for more details.

The base electrical resistance of the nanothermometer used for calibration is $R_0 = 27.82 \pm 0.01\Omega$ at room temperature, which is equivalent to the resistivity of $(7.9 \pm 1.1) \times 10^{-7}\ \Omega$-m from the geometry of the sensing area (40nm in thickness, 350nm in length between two inner electrodes, and 250nm in width, with approximately 10% uncertainties). It should be noted that the estimated resistivity is almost eight times larger than that of bulk Pt (i.e., $1.06 \times 10^{-7}\ \Omega$-m). This high resistivity may be due to the boundary scattering of electrons and defects formed during fabrication.[51] Figure 4.2(a) shows the calibration result of a nanothermometer over the temperature range from room temperature to 350K, where the electrical resistance of the thermometer sensing area is linearly proportional to the temperature increase. The corresponding temperature coefficient of resistance (TCR) is $(7.0 \pm 0.1) \times 10^{-4}\ \mathrm{K}^{-1}$, which is in good agreement with previous research.[28] From the determined TCR, we can measure the temperature change of the nanothermometer's sensing probe using $\Delta T_S = \Delta V_S / (\alpha \cdot G \cdot I \cdot R_0)$, where ΔV_S and G are the voltage change and the gain of the differential measurement circuit, respectively, α is the TCR, and I is the input current to the nanothermometer.[4,27] We also tested the feasibility of using the nanothermometer device as a heater by increasing the input current in the air. Fig. 4.2(b) shows the parabolic increases of the thermometer resistance and the power dissipation of the entire Pt nano-strip with the input current increase, demonstrating that the nanothermometer is joule-heated. At the input current of 1.6 mA, the sensing probe temperature becomes 338.5 ± 0.2 K, which is high enough to conduct tip-induced local cooling measurements. It should be noted that further heating was possible but the

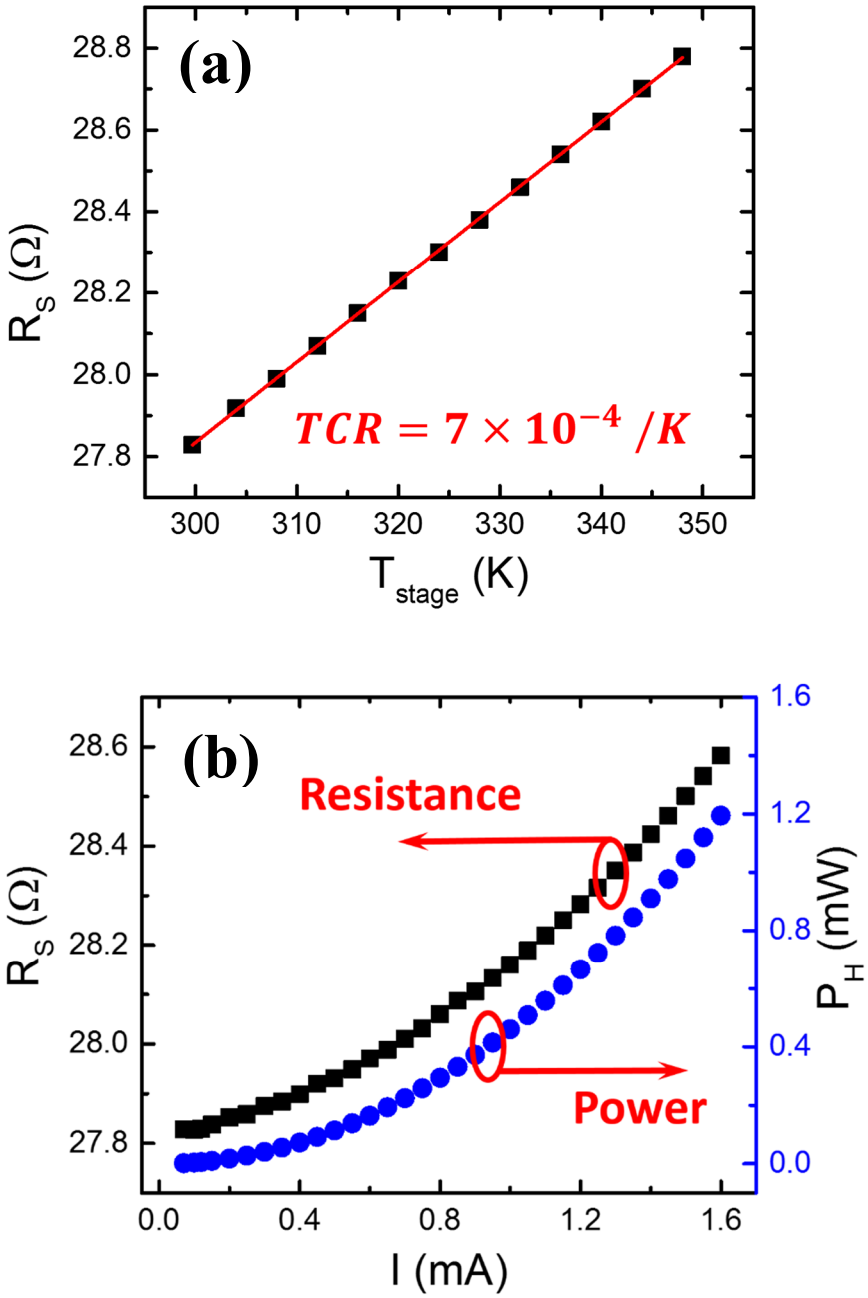

Figure 4.2. (a) The electrical resistance of the nanothermometer sensing area as a function of the stage temperature. From the linear proportionality, the TCR of the nanothermometer is determined to be 7.0×10^{-4} K^{-1}. (b) The parabolic curves of the thermometer resistance and power dissipation of the Pt nano-strip demonstrate the heating capability of the device up to 338.5K.

experiment was stopped at 1.6mA to avoid thermal damage of the device.

The tip-induced cooling experiment was conducted by raster-scanning the sensing area of a heated nanothermometer (or nanoheater) with a silicon AFM cantilever probe (Bruker, FMV-A) and simultaneously mapping topographic and thermometer signals. The tip-induced cooling rate can be determined by $P_C = I\Delta V_H$, where ΔV_H is the voltage change of the entire Pt heater between the outer electrodes, under the assumption that any change in the power dissipation across the Pt heater is due to heat loss to the tip. Figure 4.3(a) shows the SEM image of the cantilever probe used for the experiment, which has a pyramidal tip with a 16μm tip height and 8nm tip radius. The nanothermometer was joule-heated with the input current of 1.6mA, raising the temperature of the thermometer sensing area at 338.5 ± 0.2K. The cantilever scans around the thermometer sensing area (2μm×2μm) in contact mode with the set-point contact force of 15 ± 5nN. The scanning speed was set to 0.3μm/s to provide sufficient time for the thermometer to thermally respond to the tip movement, as will be discussed in Figure 4.3(c).

Figure 4.3(a) shows the topographic image around the thermometer sensing area along with the corresponding temperature and power dissipation images measured by the thermometer. The dark region in the temperature image attests local cooling by the tip when it scans over the heated thermometer sensing area. The tip-induced cooling is better depicted by the average temperature of the nanothermometer sensing area (T_S), power dissipation of the nanoheater (P_H), and the corresponding tip-substrate thermal conductance (G_C) with respect to the tip position in Figure 4.3(b). The local tip-substrate thermal conductance is estimated from $G_C = (P_{H,0} - P_H)/(T_S - T_\infty)$, where $P_{H,0}$ is the

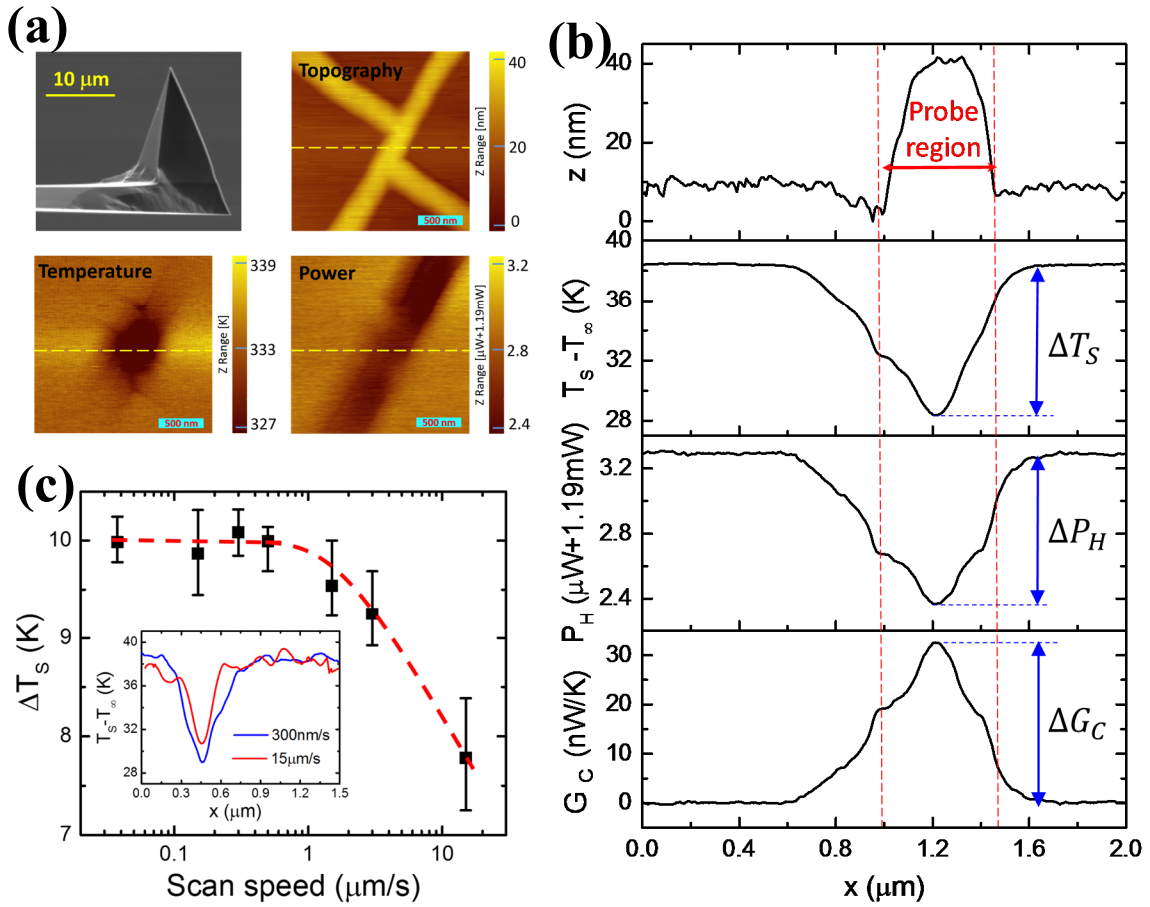

Figure 4.3. Shows (a) SEM image of the cantilever tip used as a point heat sink in contact with the nanoheater and the topography image of the thermometer sensing area (2μm×2μm) with its corresponding temperature change and the power dissipation of the Pt nano-strip. (b) The line scan profiles of the topography, thermometer temperature, and the power dissipation when the tip scans along the dashed line in (a). (c) Temperature dip depths of the thermometer sensing area due to tip-induced cooling for different tip scan speeds. The inset compares the temperature line-scan profiles for tip scan speeds at 0.3μm/s and 15μm/s. This measurement demonstrates that the nanothermometer cannot fully respond to the tip scan speed higher than 1 μm/s.

initial thermometer power dissipation, under the assumption that the tip base temperature remains constant at room temperature T_∞. As the tip scans along the yellow-dashed line in Figure 4.3(a), the thermometer sensing area, initially at $T_{S,0} = 338.5 \pm 0.2$K by $I = 1.6$mA (or $P_H = 1.19$mW), cools down due to heat conduction from the heated thermometer to the tip through solid-solid contact, water meniscus, and surrounding air molecules. The gradual change of the thermometer temperature signal follows the same trend as the numerically calculated local temperature distribution across the thermometer as shown in Figure 4.S4, indicating that the nanothermometer captures the local cooling at different tip positions: maximal cooling at the center due to the highest local temperature. The shoulders at the thermometer edges in Figure 4.3(b) are due to sudden changes in contact area between the tip and the thermometer when the tip moves from the thermometer edge to the substrate.[4] We also believe that the slightly asymmetric temperature profile is due to the uneven pyramidal tip shown in Figure 4.3(a), which may be convoluted with the thermometer signal.

From Figure 4.3(b), the temperature dip depth is $\Delta T_S = 10.1 \pm 0.2$ K when the tip is placed in the center of the thermometer sensing area. The corresponding heat loss is measured to be $\Delta P_H = 923 \pm 15$nW. The effective contact thermal conductance can be estimated from $\Delta G_C = \Delta P_H / (T_{S,\min} - T_\infty)$, where $T_{S,\min}$ denotes the dip temperature of the thermometer sensing area in Figure 4.3(b). The estimated thermal conductance is $\Delta G_C =$ 32.5 ± 0.8nW/K. The equivalent contact thermal resistance is estimated to be ~6.2×10^{-9} m^2K/W by assuming the contact diameter of the tip as ~16 nm: see the SI for more discussion about the tip contact area. This value is qualitatively in good agreement with

previous works, such as ~1.5×10^{-8} m^2K/W for SiO_2-Pt,[4] ~2.0×10^{-8} m^2K/W for Si-Si,[31] and ~2.7×10^{-9} m^2K/W for SiO_2-Au.[27] However, it should be noted that the measured thermal conductance includes heat conduction through solid-solid contact as well as water meniscus and air conduction. Although the contribution of each heat transfer mechanism was not directly measured in the present study, we estimated each thermal conductance using the theoretical model for solid-solid contact,[4] water meniscus,[52] and surrounding air[1]: further discussion can be found in the SI.

The thermal response time of the nanothermometer can also be determined by measuring ΔT_S at different tip scanning speeds. As shown in Figure 4.3(c), ΔT_S does not change until the tip scan speed increases to ~1 μm/s, but starts decreasing at higher scan speeds. The inset in Figure 4.3(c) compares temperature line profiles as the tip scans across the thermometer sensing area at 0.3μm/s and 15μm/s scan speeds, demonstrating that the thermometer cannot fully respond to the tip scan speed at 15μm/s. The tip scan speed at 1 μm/s is equivalent to the travel time of 7.8ms between adjacent pixels when a 2μm × 2μm area is scanned with a 256 × 256 resolution. Therefore, the thermal response time that is required for the nanothermometer to reach thermal equilibrium with a moving tip can be approximated at ~8ms. The tip scan speed for all experiments reported in this article was set to 0.3μm/s (~26ms per pixel) to provide sufficient time for the nanothermometer to thermally respond to the tip-induced cooling.

Figure 4.4 shows the *z*-spectroscopy of the cantilever deflection and the corresponding thermometer signal when the cantilever approaches and retracts from the thermometer sensing area. The tip was placed at the thermometer sensing area with feedback-loop control of *x*- and *y*-positions after topographic imaging. The thermometer was joule-heated

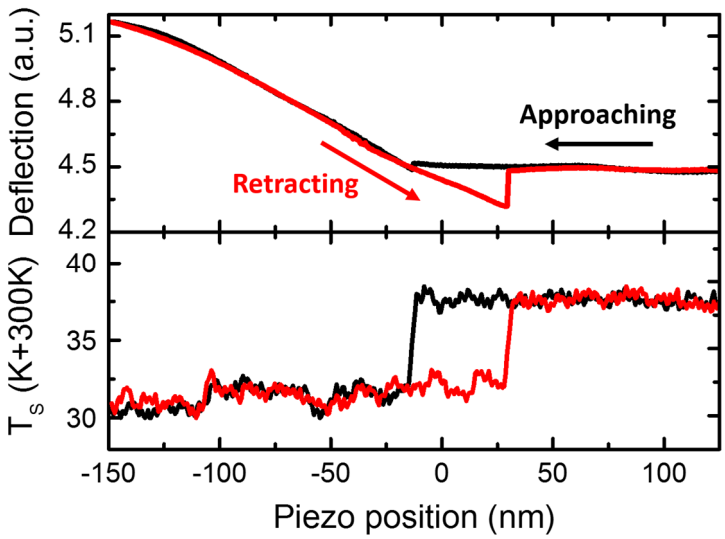

Figure 4.4. Z-spectroscopy of the cantilever deflection and the thermometer signal, initially heated at 338.5K. As the cantilever approaches the thermometer sensing area, the tip jumps into contact on the thermometer to cause a sudden temperature drop. A sudden temperature jump is also observed in the cantilever retraction curve, demonstrating that the thermometer signal change is solely due to local heat transfer through the tip-substrate contact.

with the input current of 1.6mA during the *z*-spectroscopy measurement. The cantilever deflection signal in the top figure depicts the jump-into-contact during the tip approach and the jump-out-of-contact during the tip retraction. The sudden drop and retract points are because of attractive forces between the tip and the substrate due to the capillary and the thermal forces.[27,28,53] The hysteresis of deflection response is due to elastic and possibly plastic deformation of tip and sample, resulting in larger attractive forces during retraction of the tip. The bottom plot also shows temperature jumps in the thermometer signal, corresponding to the contact of the tip. It should be noted that the thermometer z-spectroscopy was obtained by averaging 5 measurements to reduce the noise caused by the z-piezo movement in the AFM. The temperature drop when the cantilever jumps to contact is measured to be 8.3 ± 0.2K, which is slightly smaller than the temperature dip measured

from the scanning experiment (i.e., $\Delta T_S = 10.1 \pm 0.2$ K). We believe that this is because of the slightly off-center position of the tip when the z-spectroscopy was conducted. Nonetheless, the obtained *z*-spectroscopy result confirms that the temperature change of the thermometer is solely due to the local heat transfer from the heated nanothermometer to the cantilever probe upon the contact of the tip.

4.4 Conclusion

In conclusion, on-substrate resistive Pt nanothermometer/nanoheater with the sensing area of 250nm×350nm have been fabricated by combining e-beam lithography and photolithography. We believe that the fabricated device is among the smallest resistive thermometers ever made to date. The sensitivity (or TCR) of the nanothermometer is $(7.0 \pm 0.1) \times 10^{-4}$ K^{-1}, which is approximately five times smaller than that of a commercially available bulk Pt thermometer, and its noise-equivalent temperature resolution is estimated to be 410mK. In addition, we have demonstrated that the nanothermometer can be used as a nanoheater by joule-heating the device. By scanning over the heated nanothermometer sensing area with a silicon AFM probe, we measured tip-induced local cooling across the nanoscale point contact. The effective contact thermal conductance is estimated to be 32.5$\pm$0.8nW/K. The obtained results will provide physical insight onto local heat transfer and the resultant temperature distribution in various tip-based thermal engineering technologies.

4.5 Acknowledgements

This work was supported by the National Science Foundation (CBET- 1403084 and CBET-1605584) and startup support at the University of Utah. The AFM was built up partly by the Research Instrumentation Fund from the University of Utah.

4.6 Supplemental Information

4.6.1 Nanothermometer Fabrication

This section describes the combination of e-beam lithography for Pt nanopatterns and photolithography for Au micropatterns to fabricate four-point-probe Pt resistive nanothermometers. Figure 4.S1 shows the schematics of the fabrication process. The fabrication starts with a deposition of 500nm thick SiN_x layer on an 8 inch Si wafer using plasma-enhanced chemical vapor deposition (PECVD). SiN_x is chosen over SiO_2 for more favorable nanopatterning processes. This step is followed by spin coating on the wafer to generate 50nm thick PMGI (MicroChem) and 140nm thick PMMA layers for the e-beam lithography of the nanopatterns. Here, PMGI thin film is used as a lift-of-layer and PMMA is used as an e-beam resist. The next step is to deposit a Cr adhesive layer and Pt nanopatterns with e-beam evaporation followed by the lift-off process. For the lift-off process, the PMMA layer was removed by rinsing with fresh acetone at room temperature by several times and the PMGI layer was removed by dipping into Remover PG (MicroChem) at 100°C. Au micropatterns were then fabricated to be properly aligned with the nanopatterns using standard optical lithography. To this end, a negative photoresist (NLOF 2035, MicroChemicals) was coated on the wafer with nanopatterns, exposed to UV light source with the micropatterned mask on it, and developed in TMAH (2.38%) for 1

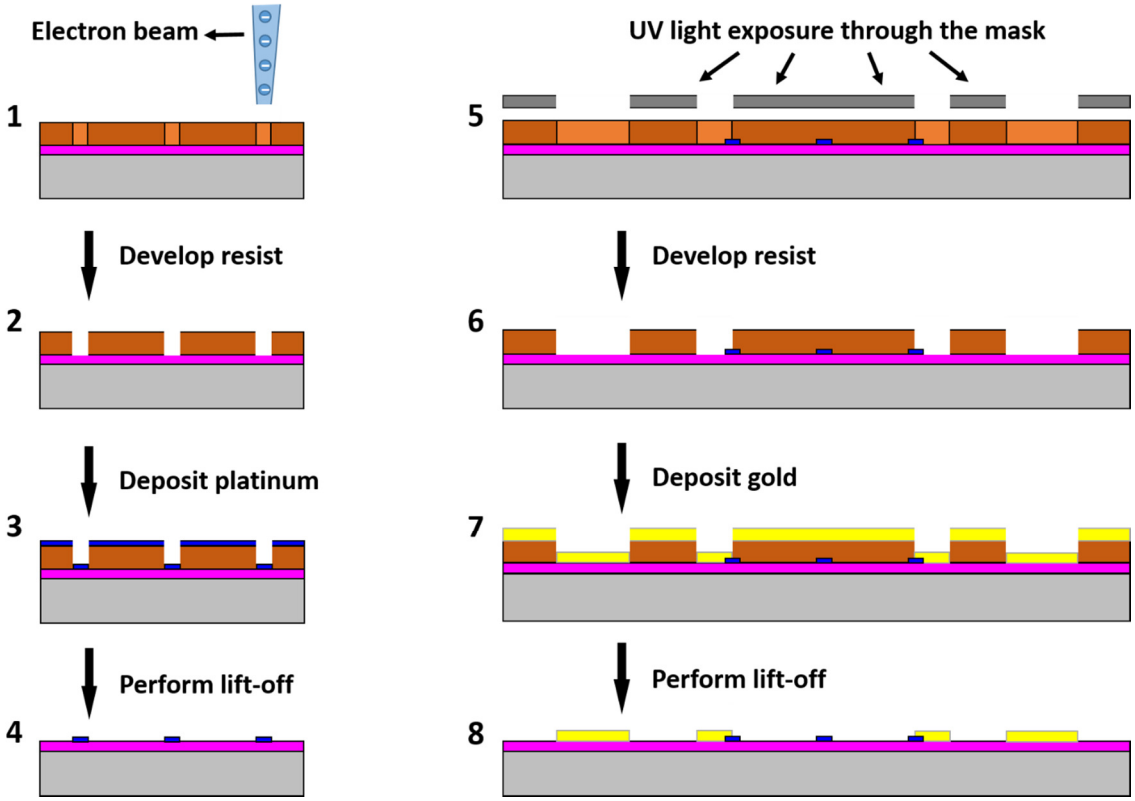

Figure 4.S1. Schematic of the nanothermometer fabrication process.

minute. After descumming by oxygen plasma for 30 seconds, Au/Cr layers were deposited by e-beam evaporation to fabricate micropatterned electrodes. We determined the optimal thickness ratio to be 200nm/10nm for Au/Cr. The photoresist was removed by dipping in acetone and the device was finally cleaned by dipping in the piranha solution for 5 minutes, rinsing with DI water and blow drying with N_2 gas.

4.6.2 Topography Image of a Nanothermometer

Topographic imaging of the nanothermometer was done using a Bruker FMV-A cantilever with resonant frequency of 75kHz in tapping mode in a customized AFM. To avoid tip wear or contamination, scanning parameters were chosen to have minimal interaction between the tip and the sample along with high feedback gains. Figure 4.S2 shows the topographic image of a nanothermometer showing its Au leading patterns within scan area of 30 μm × 30 μm. The obtained topography measures the thicknesses of Pt and Au patterns to be 40nm and 180nm, respectively. Once the large area of the nanothermometer was scanned, we zoomed in the sensing area and switch to contact mode to perform cooling experiment. Scanning parameters in contact mode were chosen very carefully to keep the tip-sample contact force at 15nN.

4.6.3 Calculation of Tip-Substrate Contact Area

According to the Hertzian theory, a contact diameter can be calculated using $d_c = (3d_t F / E^*)^{1/3}$ where d_t, F, and E^* are cantilever tip diameter, tip-substrate contact force, and effective elastic modulus, respectively. The effective elastic modulus can be

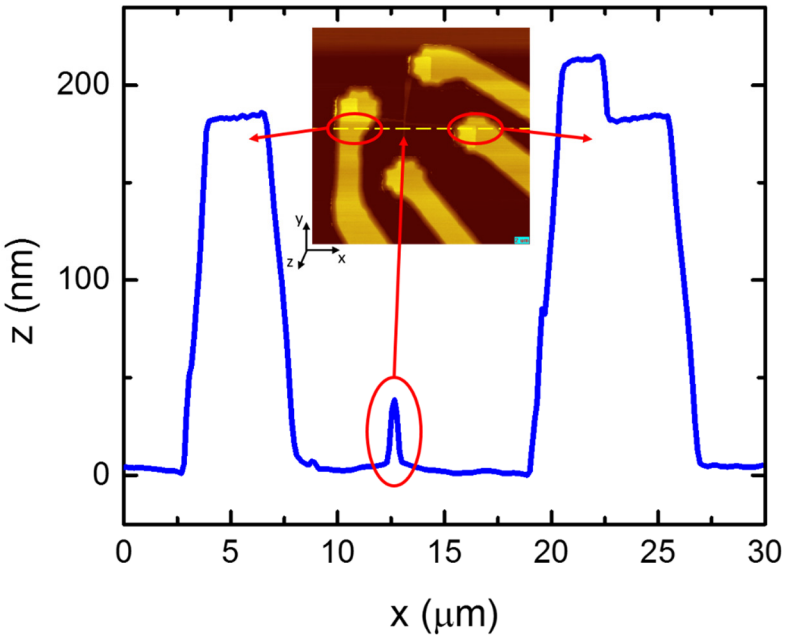

Figure 4.S2. Topography image around the sensing area of the nanothermometer. The scanned area is 30 μm × 30 μm to show both the Pt pattern and Au electrodes.

written as $E^* = \left[\frac{1-\upsilon_1^2}{E_1} + \frac{1-\upsilon_2^2}{E_2}\right]$ where υ_1 (υ_2) and E_1 (E_2) are Poisson's ratio and Young's modulus for Si (Pt[54,55]), respectively. Mechanical properties of the substrate will be more accurate if we consider it as a 40 nm Pt thin film over a 500nm SiN_x[56]. When a Si tip with an 8nm tip radius is in contact with a Pt layer with the contact force is 15 ± 5nN, the contact diameter predicted by the Hertzian theory is 2.0 ± 0.2nm.

While the ideal contact area can be calculated from the Hertzian model, the realistic contact area may be much larger as the cantilever is tilted slightly (~11°) toward the substrate in its holder. In this case, the tip-substrate contact can be made on the front surface of the tip to form an elliptic contact area. Pettes and Shi[31] estimated the upper limit of the contact diameter to be 122nm from the SEM image of the AFM probe tip having the tip

radius of $r_{tip} = 62.5\,\text{nm}$, while the lower limit was estimated to be 3.4±0.7nm from the Derjaguin-Muller-Toporov model. Using the same scheme, we estimate the upper limit of the contact diameter to be approximately 16nm when the tip radius is 8nm.

4.6.4 Calculation of Thermal Conductance for Different Tip-Substrate Heat Transfer Mechanisms

Although contribution of each heat transfer mechanism could not be measured directly in the present study, we estimated it by using theoretical thermal conductance models for solid-solid contact,[4] water meniscus,[52] and surrounding air.[1]

Solid-solid thermal conductance can be estimated from $G_{ss} = \pi a k_s k_t \tan\theta / \left(2k_s + k_t \tan\theta\right)$, where a is the contact diameter, θ is the half angle of a cone-shaped tip, and k_s and k_t are thermal conductivity of the substrate and the tip, respectively.[4] We used $\theta =$ 17° and $k_t = 20$ W/m-K for a Si tip.[57] We also calculated k_s as the effective thermal conductivity of the substrate that is composed of a Pt layer with 40 nm in thickness and SiNx layer with 500 nm in thickness.[4] The calculated k_s is ~12.5W/m-K from thermal conductivities found in literature.[46,58] The solid-solid contact thermal conductance is estimated to be ~15.7 nW/K when the contact diameter is estimated from the Hertzian model.

Thermal conductance due to water meniscus can be modeled as the series connection of two thermal conductances at the water-sample interface and at the probe-water interface, i.e., $G_{\text{meniscus}}^{-1} = G_{\text{water-substrate}}^{-1} + G_{\text{probe-water}}^{-1}$.[52] The thermal conductance through the water meniscus can be ignored compared to the other conductances.[59] Detailed procedures to

calculate $G_{\text{water-substrate}}$ and $G_{\text{probe-water}}$ are well described in Ref. [52] and will not be repeated here. Since the thermal conductance per unit area at the water-solid interface is reported to be in the range of $h =$ 100–180 MW/m^2-K,[60] we estimate the thermal conductance for water-sample interface to be 4.8–8.6 nW/K from $G_{\text{water-substrate}} = h\pi r_w^2$ and the thermal conductance of probe-water interface to be 58–104 nW/K from $G_{\text{probe-water}} = 2h\pi R_a^2$ for the relative humidity of 20% (Salt Lake City, UT, USA) and the capillary force at 20 nN. Here, r_w is the effective radius formed by water meniscus between the probe and substrate, and R_a is an equivalent curvature radius of a probe. Therefore, the thermal conductance due to water meniscus, G_{meniscus}, can be estimated to be in a range of 4.4–7.9 nW/K.

The total air conductance can be calculated using $G_{air} = 2\pi k_g L \tan\theta\left[1 - l\tan\theta/(2L)\right]$ where k_g is the air thermal conductivity, l is the mean free path of air molecules, and L is decided by the isothermal length of the tip.[1] The isothermal length of the tip defines the effective surface area of air conduction and should be determined by a smaller geometry between the tip and the nanoheater. For the range of L between 100 nm and 1 μm (i.e., half the width and the length of the nanoheater, respectively), the air thermal conductance ranges from 4.5 to 49.8 nW/K.

We did not consider the effect of near-field thermal radiation when considering the small temperature increase of the nanothermometer.[31] The recent quantitative measurements[61] reveal the thermal conductance due to near-field radiation is ~1.5 nW/K for SiO_2-SiO_2, ~0.4 nW/K for SiN-SiN, and ~0.1 nW/K for Au-Au tip-substrate materials when the gap distance is less than 2nm and the temperature difference is 115 K. When considering our configuration (i.e., Si tip on a Pt substrate), we estimate that the thermal

conductance due to near-field thermal radiation would be smaller than 1 nW/K.

From the theoretical modeling, the effective thermal conductance between the tip and the substrate is estimated to be in the range of 24.6–73.4 nW/K, which is in good agreement with our measurement for the maximum thermal conductance in this letter (i.e., 32.5 nW/K).

4.6.5 Power Spectral Density

Figure 4.S3 shows power spectral density (PSD) curves of the voltage signal of the differential measurement circuit in figure 4.1(c) when the input current is zero and 1.6mA. The two curves are almost overlapped in the frequency range over 1 Hz: small difference in this frequency range may be due to shot noise and temperature drift effects[62]. However, there is a significant difference between the two curves in lower frequencies due to the dc experiment performed in this work. To calculate the noise equivalent temperature (NET), the obtained PSD is curve-fitted with a ninth order polynomial function for the frequency range between f=0Hz and f=0.5Hz (see inset Figure 4.S3). By integrating the PSD over frequency range from 0 to 0.5Hz ($NEV^2 = \int_0^f PSD_V(f)df$), we calculated the noise equivalent voltage to be 12.97μV. Since the noise equivalent temperature can be calculated from the noise equivalent voltage using $NET = NEV/(I \cdot \alpha \cdot R_0)$, the noise-equivalent temperature resolution is calculated to be 410mK. Noise floor of the experimental setup is measured to be below 10 nV/Hz$^{1/2}$.

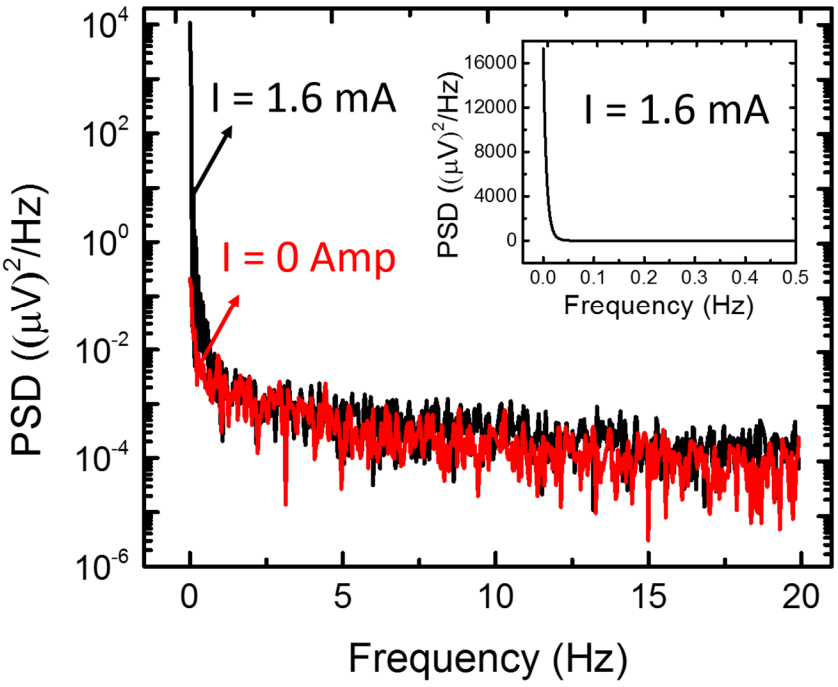

Figure 4.S3. The power spectral density (PSD) curves of voltage signals for I=0 Amp and I=1.6 mA, showing small shot noise and noise due to temperature drift for frequency range over 1Hz. However, the 1/f noise is high below 1 Hz. Inset shows a curve fitted with obtained PSD data for the frequency range from 0 to 0.5Hz, from which the noise equivalent temperature (NET) of the thermometer is calculated.

4.6.6 Temperature Distribution Within the Heater

In order to verify the temperature distribution measurement shown in Figure 4.3, we numerically computed the temperature distribution across the Pt nano-strip under joule-heating using the finite element method (COMSOL Multiphysics). This shows that the trend in the temperature drop of the sensor mean temperature with respect to tip location, follows the same trend as the temperature distribution across the sensing area. COMSOL Multiphysics is used in other numerical modeling problems as well[63,64]. Assuming perfect electrical leading of Au leads, we modeled the joule-heating of a 40nm-thick Pt nano-strip

on a 500nm-thick SiN_x substrate. Knowing the width of the sensing probe being ~250nm, we used the Fourier law for thermal transport simulation assuming diffusive heat transfer. Since the mean free path of free electrons in Pt is ~10 nm,[65] the size of the Pt nano-strip is big enough to ignore sub-continuum heat transfer, such as ballistic heat conduction. The temperature at the bottom of SiN_x layer is assumed to be constant at room temperature, while the adiabatic conditions are given to the rest of surface boundaries to simulate the vacuum operation of the nanothermometer. An electric potential is set on two sides of the Pt, one at high voltage and the other one at ground with insulated boundaries for the rest of Pt nanowires. Figure 4.S4 shows the geometry as well as the temperature distribution within the domain for an input current of 1.6 mA. The graph shows dimensionless temperature distribution along the dotted lines shown in both 2-D schematic and the AFM topography image. Due to thermal conduction to the substrate, the temperature distribution along the dotted line has a maximum temperature in the middle. This is consistent with the maximum temperature drop of the thermometer when the tip is placed in the middle of the sensing area. The normalized temperature distribution curve (inversed) obtained from the tip-cooling measurement is in good agreement with the calculated temperature distribution, indicating that the tip-induced cooling is due to the local heat transfer between a tip and a substrate area confined to the tip contact.

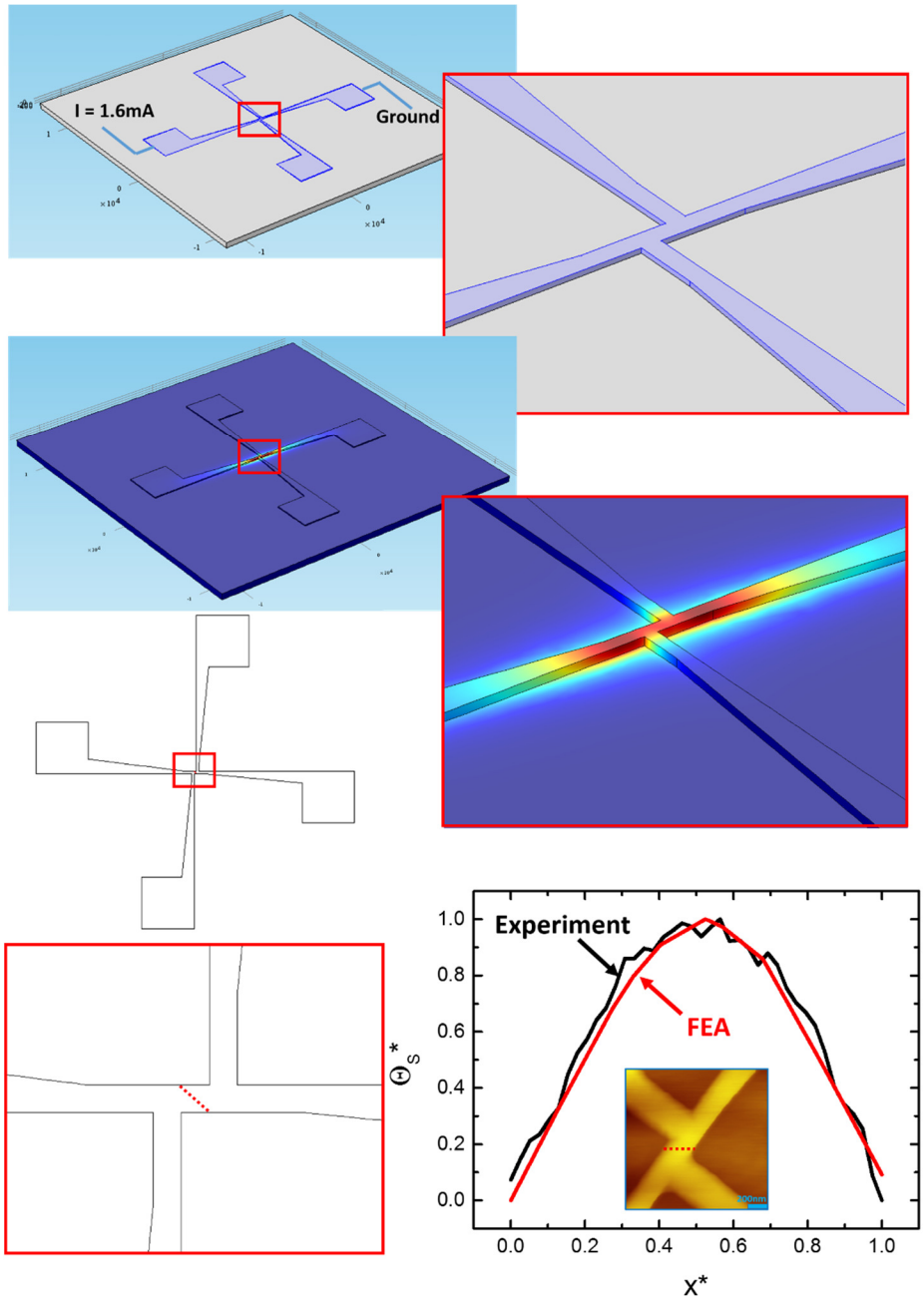

Figure 4.S4. 3-D Schematic, boundary conditions, and the finite element analysis results for a joule-heated Pt nano-strip. The comparison of normalized temperature distributions across the Pt nano-strip between the measurement and computation verifies that the tip-induced cooling is due to local heat transfer between a tip and a substrate area confined to the tip contact.

4.7 References

[1] A. Majumdar, Annu. Rev. Mater. Sci. **29**, 505 (1999).

[2] M. Hinz, O. Marti, B. Gotsmann, M. A. Lantz, and U. Durig, Appl. Phys. Lett. **92**, 43122 (2008).

[3] U. F. Wischnath, J. Welker, M. Munzel, and A. Kittel, Rev. Sci. Instrum. **79**, 73708 (2008).

[4] K. Kim, W. Jeong, W. Lee, and P. Reddy, ACS Nano **6**, 4248 (2012).

[5] W. P. King, S. Saxena, B. A. Nelson, B. L. Weeks, and R. Pitchimani, Nano Lett. **6**, 2145 (2006).

[6] J. Lee, A. Liao, E. Pop, and W. P. King, Nano Lett. **9**, 1356 (2009).

[7] S. Jesse, M. P. Nikiforov, L. T. Germinario, and S. V. Kalinin, Appl. Phys. Lett. **93**, 73104 (2008).

[8] M. P. Nikiforov, S. Gam, S. Jesse, R. J. Composto, and S. V. Kalinin, Macromolecules **43**, 6724 (2010).

[9] K. J. Kim, K. Park, J. Lee, Z. M. Zhang, and W. P. King, Sens. Actuators, A **136**, 95 (2007).

[10] S. Somnath, E. A. Corbin, and W. P. King, IEEE Sens. J. **11**, 2664 (2011).

[11] B. Lee, S. Somnath, and W. P. King, Nanotechnology **24**, 135501 (2013).

[12] A. Hammiche, L. Bozec, M. Conroy, H. M. Pollock, G. Mills, J. M. R. Weaver, D. M. Price, M. Reading, D. J. Hourston, and M. Song, J. Vac. Sci. Technol. B **18**, 1322 (2000).

[13] M. Reading, D. Grandy, A. Hammiche, L. Bozec, and H. M. Pollock, Vib. Spectrosc. **29**, 257 (2002).

[14] A. C. Jones and M. B. Raschke, Nano Lett. **12**, 1475 (2012).

[15] G. Binnig, M. Despont, U. Drechsler, W. Haberle, M. Lutwyche, P. Vettiger, H. J. Mamin, B. W. Chui, and T. W. Kenny, Appl. Phys. Lett. **74**, 1329 (1999).

[16] W. P. King, T. W. Kenny, K. E. Goodson, G. Cross, M. Despont, U. Durig, H. Rothuizen, G. K. Binnig, and P. Vettiger, Appl. Phys. Lett. **78**, 1300 (2001).

[17] D.-W. Lee, T. Ono, T. Abe, and M. Esashi, J. Microelectromech. Syst. **11**, 215 (2002).

[18] W. A. Challener, C. Peng, A. V. Itagi, D. Karns, W. Peng, Y. Peng, X. Yang, X. Zhu, N. J. Gokemeijer, Y.-T. Hsia, G. Ju, R. E. Rottmayer, M. A. Seigler, and E. C. Gage, Nat.

Photonics **3**, 303 (2009).

[19] P. E. Sheehan, L. J. Whitman, W. P. King, and B. A. Nelson, Appl. Phys. Lett. **85**, 1589 (2004).

[20] M. Yang, P. E. Sheehan, W. P. King, and L. J. Whitman, J. Am. Chem. Soc. **128**, 6774 (2006).

[21] R. Szoszkiewicz, T. Okada, S. C. Jones, T.-D. Li, W. P. King, S. R. Marder, and E. Riedo, Nano Lett. **7**, 1064 (2007).

[22] A. A. Milner, K. Zhang, and Y. Prior, Nano Lett. **8**, 2017 (2008).

[23] O. Fenwick, L. Bozec, D. Credgington, A. Hammiche, G. M. Lazzerini, Y. R. Silberberg, and F. Cacialli, Nat. Nanotechnol. **4**, 664 (2009).

[24] A. W. Knoll, D. Pires, O. Coulembier, P. Dubois, J. L. Hedrick, J. Frommer, and U. Duerig, Adv. Mater. **22**, 3361 (2010).

[25] D. Pires, J. L. Hedrick, A. De Silva, J. Frommer, B. Gotsmann, H. Wolf, M. Despont, U. Duerig, and A. W. Knoll, Science **328**, 732 (2010).

[26] Z. Wei, D. Wang, S. Kim, Y. Hu, M. Yakes, A. Laracuente, Z. Dai, S. Marder, C. Berger, W. King, W. Heer, P. Sheehan, and E. Riedo, Science **328**, 1373 (2010).

[27] L. Shi and A. Majumdar, J. Heat Transfer **124**, 329 (2002).

[28] K. Park, G. L. W. Cross, Z. M. Zhang, and W. P. King, J. Heat Transfer **130**, 102401 (2008).

[29] K. Kim, J. Chung, G. Hwang, O. Kwon, and J. S. Lee, ACS Nano **5**, 8700 (2011).

[30] W. Lee, K. Kim, W. Jeong, L. A. Zotti, F. Pauly, J. C. Cuevas, and P. Reddy, Nature 498, 209 (2013).

[31] M. T. Pettes and L. Shi, J. Heat Transfer **136**, 32401 (2013).

[32] K. E. Goodson and M. Ashegh, Microscale Thermophys. Eng. **1**, 225 (1997).

[33] B. McCarthy, Y. Zhao, R. Grover, and D. Sarid, Appl. Phys. Lett. **86**, 111914 (2005).

[34] A. A. Milner, K. Zhang, V. Garmider, and Y. Prior, Appl. Phys. A **99**, 1 (2010).

[35] Y. Yue, X. Chen, and X. Wang, ACS Nano **5**, 4466 (2011).

[36] B. Samson, L. Aigouy, P. Lo€uw, C. Bergaud, B. J. Kim, and M. Mortier, Appl. Phys. Lett. **92**, 23101 (2008).

[37] K. Kim, J. Chung, J. Won, O. Kwon, J. S. Lee, S. H. Park, and Y. K. Choi, Appl. Phys.

Lett. **93**, 203115 (2008).

[38] S. Sadat, A. Tan, Y. Chua, and P. Reddy, Nano Lett. **10**, 2613 (2010).

[39] P. C. Fletcher, B. Lee, and W. P. King, Nanotechnology **23**, 035401 (2011).

[40] E. A. Corbin, K. Park, and W. P. King, Appl. Phys. Lett. **94**, 243503 (2009).

[41] B. Lee and W. P. King, Rev. Sci. Instrum. **83**, 74902 (2012).

[42] D. Chu, D. Bilir, R. Pease, and K. Goodson, J. Vac. Sci. Technol. B **20**, 3044 (2002).

[43] H. Liu, W. Sun, and S. Xu, Adv. Mater. **24**, 3275 (2012).

[44] X. Huo, H. Liu, Y. Liang, M. Fu, W. Sun, Q. Chen, and S. Xu, Small **10**, 3869 (2014).

[45] F. Menges, H. Riel, A. Stemmer, and B. Gotsmann, Nano Lett. **12**, 596 (2012).

[46] S. Sadat, E. Meyhofer, and P. Reddy, Rev. Sci. Instrum. **83**, 84902 (2012).

[47] S. Sadat, E. Meyhofer, and P. Reddy, Appl. Phys. Lett. **102**, 163110 (2013).

[48] D. G. Cahill, Rev. Sci. Instrum. **61**, 802 (1990).

[49] L. Lu, W. Yi, and D. L. Zhang, Rev. Sci. Instrum. **72**, 2996 (2001).

[50] C. Dames and G. Chen, Rev. Sci. Instrum. **76**, 124902 (2005).

[51] X. Zhang, H. Xie, M. Fujii, H. Ago, K. Takahashi, T. Ikuta, H. Abe, and T. Shimizu, Appl. Phys. Lett. **86**, 171912 (2005).

[52] A. Assy and S. Gomès, Nanotechnology **26**, 355401 (2015).

[53] B. Gotsmann and U. Durig, Appl. Phys. Lett. **87**, 194102 (2005).

[54] M. C. Salvadori, I. G. Brown, A. R. Vaz, L. L. Melo, and M. Cattani, Phys. Rev. B, **67**, 153404 (2003).

[55] M. A. Mamun, D. Gu, H. Baumgart, and A. A. Elmustafa, Surf. Coatings Technol., **265**, 185 (2015).

[56] L. Buchaillot, E. Farnault, M. Hoummady, and H. Fujita, Jpn. J. Appl. Phys., 36, **794** (1997).

[57] B. A. Nelson, and W. P. King, Nanosc. Microsc. Therm., **12**, 98 (2008).

[58] X. Zhang, and C. P. Grigoropoulos, Rev. Sci. Instrum., **66**, 1115 (1995).

[59] K. Luo, Z. Shi, J. Varesi, and A. Majumdar, J. Vac. Sci. Technol. B, **15**, 349 (1997).

[60] Z. Ge, D. G. Cahill, and P. V. Braun, Phys. Rev. Lett., **96**, 186101 (2006).

[61] K. Kim, B. Song, V. Fernández-Hurtado, W. Lee, W. Jeong, L. Cui, D. Thompson, J. Feist, M. T. H. Reid, F. J. García-Vidal, J. C. Cuevas, E. Meyhofer, and P. Reddy, Nature, **528**, 387–391 (2015).

[62] J. Zheng, M. C. Wingert, E. Dechaumphai, and R. Chen, Rev. Sci. Instrum., **84**, 114901 (2013).

[63] S. Chen, Q. Wu, C. Mishra, J. Kang, H. Zhang, K. Cho, W. Cai, A. A. Balandin, and R. S. Ruoff, Nat. Mater., **11**, 203 (2012).

[64] Z. Yan, C. Jiang, T. R. Pope, C. F. Tsang, J. L. Stickney, P. Goli, J. Renteria, T. T. Salguero, and A. A. Balandin, J. Appl. Phys., **114**, 204301 (2013).

[65] K. T. Regner, D. P. Sellan, Z. Su, C. H. Amon, A. J. H. McGaughey, and J. A. Malen, Nat. Commun., **4**, 1640 (2013).

CHAPTER 5

CONCLUSIONS AND FUTURE RECOMMENDATIONS

5.1 Conclusion

This dissertation provides a profound experimental and numerical study on diffusive and ballistic thermal transport in micro/nanometer scale to help understand fundamentals of heat transfer in subcontinuum regime. The research follows three main scopes including (1) the theory behind nanoscale heat transfer in thin films, in which for the first time the corresponding governing equations are solved in two-dimensions using a publicly available commercial package, COMSOL Multiphysics; (2) full-spectrum investigation of thermal behavior of scanning thermal microscope's heated microcantilever probe, which is the first three-dimensional frequency-dependent thermal analysis on heated microcantilevers and is expandable to other MEMS devices; and (3) tip-substrate thermal transport analysis, in which the smallest-ever fabricated four-probe Pt resistive nanothermometer is used to quantitatively measure tip-substrate thermal transport in air and vacuum environments, followed by extensive analysis of the contribution of each heat transfer mechanism.

It is shown that Fourier's law is incapable of predicting thermal transport at a length scale smaller than or comparable to mean free path (mfp) of phonons, the dominant thermal energy carriers, or at very short time scale. On the other hand, due to its statistical base accounting for phonon-phonon and phonon-boundary interactions, Boltzmann transport

equation (BTE) has shown strong capability in modeling thermal transport in sub-continuum regime. However, as a very complicated equation, it is so hard to solve BTE even with many simplifications. Therefore, in this work, a widely available commercial package is used to solve BTE under gray relaxation time approximation using combination of discrete ordinate method (DOM) and finite element analysis (FEA) to model thermal transport from continuum to sub-continuum regime for two-dimensional slabs at different Knudsen numbers ranging from 0.01 to 10 showing gradual transition from diffusive to ballistic heat transfer as Kn number increases. The total number of 256 phonon propagation directions are considered in solving the phonon BTE equation to minimize ray effect at higher Kn numbers. Even though the model is solved only for simple 2-D geometries, it can be easily expanded to 3-D and more complicated geometries which will be discussed in the next subsection, in the future recommendations.

It is also shown how a thermal microcantilever, capable of localized heating in nanometer scale, behaves under periodic joule heating operational condition. The thermal transfer function is calculated by measuring the third harmonic voltage change of the microcantilever at a range of operational frequencies from 10 Hz up to 34 kHz, and compared with a finite element analysis of the heat equation in frequency-domain. The simulation solves for an actual thermal cantilever, for the first time, in a three-dimensional model. The experiment and the modeling are done in both air and vacuum environments to fully understand the effect of air as the surrounding medium on the in-phase and out-of-phase components of thermal transfer function. The ac temperature distribution is also shown at different heating frequencies, indicating the hot area to be more localized and confined to the heater and constricted regions as the heating frequency increases. The effect

of heater size and the constriction size is also studied at the end to see the geometry effect on how a thermal microcantilever behaves under periodic heating.

Finally, a quantitative measurement is presented to study thermal transport between a sharp Si tip and an on-Si/SiN_x-substrate nanothermometer/heater with a sensing probe size of 250 nm × 350 nm, fabricated using combination of electron-beam lithography for Pt nanowires and photolithography for Au connections and contact pads. The four-probe resistive nanothermometer has the smallest sensing probe among all its predecessors, representing the temperature averaged over the small area of 250 nm × 350 nm. The device is calibrated, its temperature coefficient of resistance is measured, and the noise-equivalent temperature resolution is calculated. After showing that the device can be used as a local heater, it is used in an elevated temperature while an AFM Si cantilever at room temperature is used to scan over the sensing area, causing heat transfer from the hot nanoheater to the cantilever through the tip in contact with the substrate. This experiment is done in an air environment followed by extensive analysis to theoretically model contribution of each thermal transport mechanism (i.e., conduction through solid-solid contact, water meniscus, surrounding air, and radiative heat transfer due to near-field effects). The results show that the effective thermal conductance of the experiment in air is 32.5 nW/K. Thermal conductance due to near-field thermal radiation is shown that can be neglected. The range for thermal conductance for each of solid-solid, water meniscus, and air conduction is estimated to be 15.7 nW/K, 4.4 – 7.9 nW/K, and 4.5 – 49.8 nW/K, respectively. The overall range for effective thermal conductance is 24.6 – 73.4 nW/K which is in good agreement with the measured value (i.e., 32.5nW/K).

To experimentally study the effect of each mechanism, the same experiment is

conducted in both air and vacuum, complementing the aforementioned results. For the new experiment, the effective thermal conductance is measured to be 35.2 nW/K and 17.8 nW/K for air and vacuum, respectively. The details of the results are presented in the Appendix. The ratio between the results in air and vacuum is 50% whereas this ratio in the previous experiment between the solid-solid conduction and the effective thermal conductance in air was 48%. This is correct if we assume that there would be no water meniscus formed around the cantilever's tip in the vacuum condition at 10^{-5} Torr. The deviation between the measured effective thermal conductances in air is due to the new set up (i.e., different cantilever and nanothermometer that could potentially result in a different tip-substrate contact quality). Also, different temperatures that the nanothermometer is operating at affect the conduction through surrounding air.

5.2 Future Recommendations

5.2.1 Tip-Substrate Thermal Transport Modeling

One of the limitations in modeling subcontinuum thermal transport is the complicated governing equations that require high-speed computational power. As mentioned in Chapter 2, the 2D DOM-FEA model for ballistic-diffusive heat transfer can be simply extended to 3D and complicated geometries upon availability of computing machines with large memories. The tip-substrate geometry would be a very interesting model to simulate as it helps predict thermal transport between a sharp tip and a substrate. This model provides a strong tool for predicting temperature distribution throughout the tip in contact with the substrate, at different contact forces and corresponding contact areas. This allows accurately defining operation parameters of different tip-based thermal engineering

applications. Figure 5.1 shows an example of such geometry in 2D.

5.2.2 Thermophysical Property Measurement of Materials

Electrothermal characterization of thermal microcantilevers, combined with the frequency-dependent heat transfer model, provides a strong tool to estimate thermophysical properties of materials at nano/picogram level. A thermal microcantilever at an elevated temperature in contact with a substrate can be used to locally melt down a small area near the hot tip. Once the material is melted, the microcantilever can be moved around and scoop small amounts of material on the top of it. Using the 3ω method, and the developed model, thermophysical properties of the scooped material can be used to curve-fit the experimental results with the model. Figure 5.2 shows a thermal microcantilever with some PMMA melted on the top. The weight of the PMMA can be calculated using changes in the resonance frequency of the microcantilever.

5.2.3 Tip-Substrate Thermal Conduction

The effect of a water meniscus surrounding a tip in contact with a substrate on thermal transport is reported for the tip at different temperatures [1]. Yet, it would be of great interest to systematically control humidity of the environment and measure tip-substrate thermal transport to precisely evaluate contribution of heat transfer through water meniscus. One of the methods for controlling a chamber's humidity is to use salt solutions in the medium. Table 5.1 shows a list of salts with specific weight ratio to achieve a specific humidity [2]. Conducting the tip-induced cooling experiments at different humidities would be an important step in tip-based thermal engineering. In addition, thermal

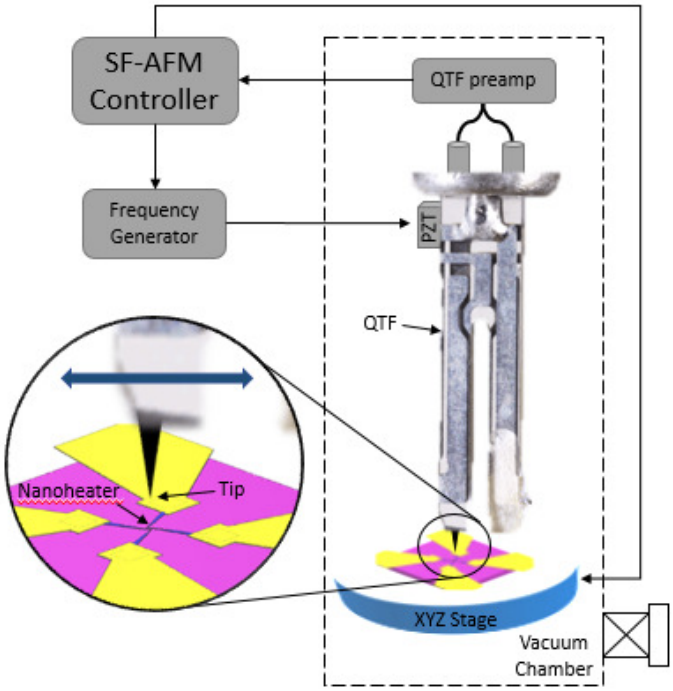

Figure 5.1. Schematic of shear force AFM using a quartz tuning fork oscillator scanning over a nanothermometer to quantitatively measure near-field radiative heat transfer between a tip and a substrate.

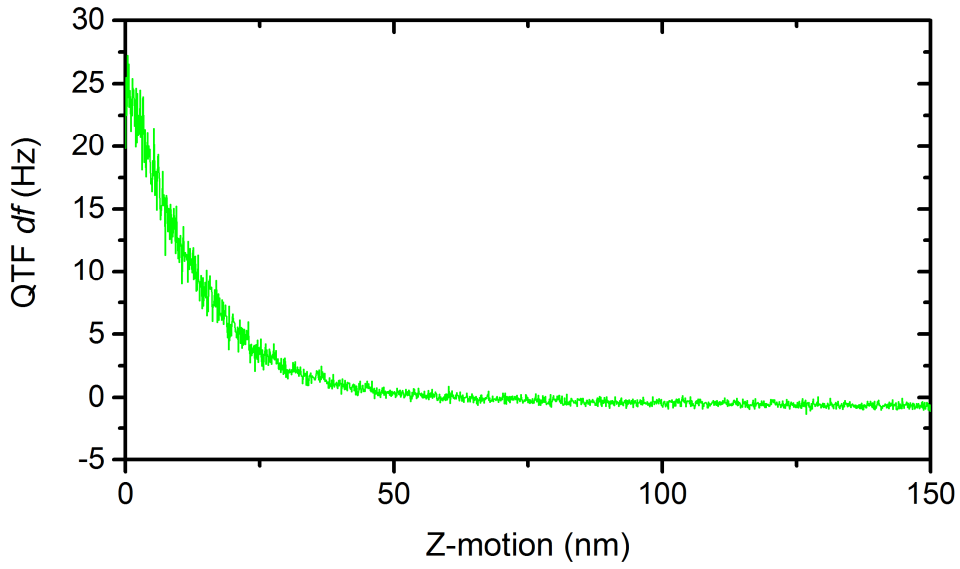

Figure 5.2. QTF resonant frequency shift as it approaches a substrate

Table 5.1. Salt solution and expected relative humidity [2].

Salt	Water content	Expected relative humitidy
15g LiCl	12 ml	11%
30 g Mg Cl_2	3 ml	33%
20g NaCl	10 ml	75%
30g K_2SO_4	10 ml	97%

conductance between different materials can open up new horizons in different applications of tip-based thermal engineering. In the reported experiment in Chapter 4, an Si tip is used, while by simply changing the tip to SiN_x or another widely used semiconductor material, the effect of tip thermal conductivity on heat transfer can be studied. Finally, effective thermal conductance measurement in vacuum at different nanothermometer temperatures can provide information on contribution of near-field radiative heat transfer and whether it is comparable to solid-solid conductance.

5.2.4 Radiative Heat Transfer at Extreme Near-Field

One of the thermal transport mechanisms between a sharp tip and a substrate at an elevated temperature is near-field thermal radiation, which has been shown to exceed the far-field limit, governed by Planck's blackbody distribution, due to the contribution of evanescent modes to energy transport as the emitter-receiver separation becomes much smaller than the thermal wavelength [3]. Measurement of radiative heat transfer is very challenging mainly because of difficulties in precision gap control between a sharp tip and a substrate. Quantitative measurement of near-field radiation using an AFM cantilever is reported for gap distances below 10nm [4]. It is extremely difficult to use a cantilever for gap distances below 2nm as the tip snaps into the substrate because of cantilever deflection due to strong attractive forces of the substrate, however such a small gap distance can be

achieved by shear force AFM (SF-AFM) using a quartz tuning fork (QTF) with a tip glued on one of its prongs. Oscillating a QTF at its scissor-like fundamental mode allows lateral movement of the tip, maintaining the tip-substrate gap distance, while preventing it from snapping into the substrate due to the QTF stiffness. While maintaining a constant gap distance between the tip and the substrate, the QTF can be used to scan over the nanothermometer/heater sensing area in vacuum condition to quantitatively measure radiative heat transfer from the nanoheater to the tip. Figure 5.1 shows the schematic of SF-AFM using a QTF oscillator, scanning over a nanothermometer in vacuum chamber. To operate the QTF, SF-AFM controller feedbacks off of the resonant frequency shift of the QTF due to tip-substrate force interactions as the QTF approaches the substrate. Figure 5.2 shows the resonant frequency shift of a QTF as it approaches to a substrate in vacuum. Although not shown, a sudden change in *df* happens upon tip contact with the substrate. To this end, some preliminary data is collected indicating validity of this promising approach. Figure 5.3 shows temperature response of the nanoheater as the QTF tip approaches the nanoheater. More experiments can be conducted to quantitatively measure thermal radiation between a sharp tip and a substrate.

5.2.5 Temperature-Dependent Near-Field Force-Gradient in Air and Vacuum

Force microscopy at nanoscale is the base of significant inventions such as AFM providing a strong tool to investigate forces between a tip and a substrate, including but not limited to Van Der Waals forces [5] in molecular regime, Casimir-Polder force [6–8] in quantum electrodynamics (QED) and meniscus forces [9]. There are many applications benefitting from force analysis at nanoscale such as material characterization by force

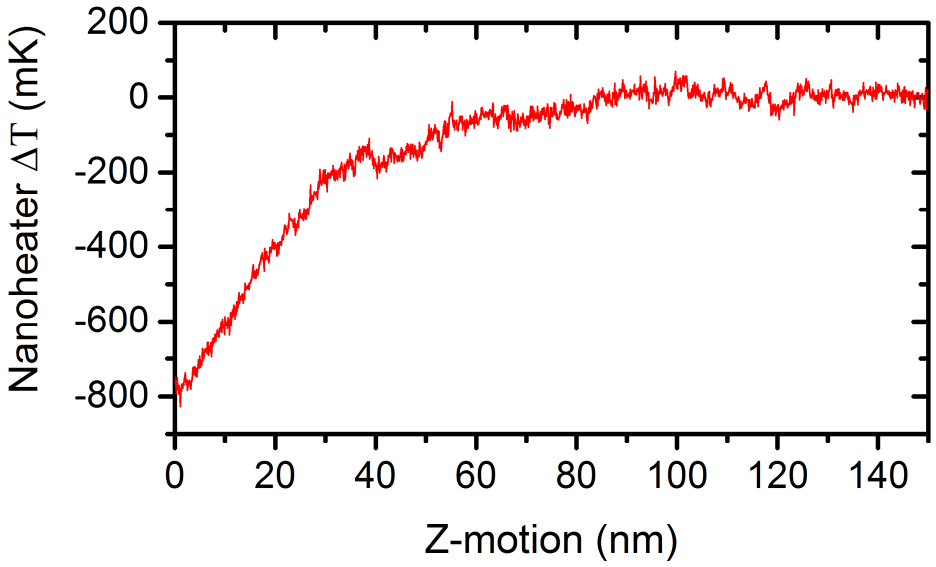

Figure 5.3. Temperature response of the nanoheater as the QTF approaches resulting in temperature drop in nanoheater due to tip-substrate radiative heat transfer.

spectroscopy using quartz tuning fork (QTF) scanning probes [10,11]. Not many studies considered temperature dependence of such close range forces. QTF probes are promising tools for near-field force analysis, due to their high sensitivity to force gradient. To study effect of temperature on the aforementioned close range forces, shear force-AFM with a QTF probe can be used to scan over a nanoheater at different elevated temperatures while monitoring the substrate motion. During an SF-AFM scan over the nanoheater using a QTF probe, at a constant QTF resonant frequency shift (*df*), a substrate's z-motion can be monitored which can be used to provide information of force gradient for different nanoheater temperatures. Figure 5.4 shows some preliminary measurements for substrate z-motion as a function of substrate temperature for different *df* as the feedback loop parameter to the SF-AFM controller to keep the QTF tip-substrate distance constant. *df* also allows direct computation of force gradient ($\partial F/\partial Z$) given the QTF spring constant

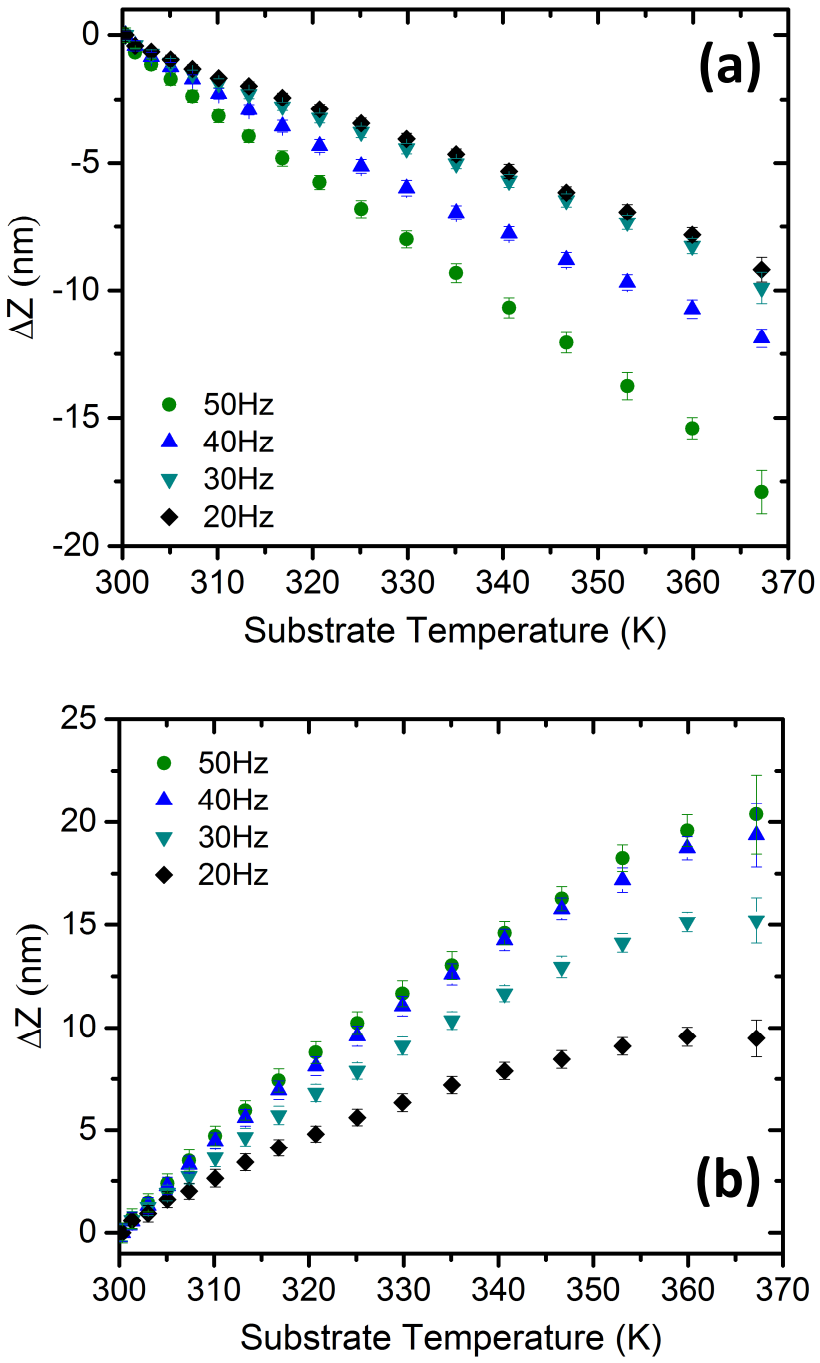

Figure 5.4. Measured substrate z-motion at different nanoheater temperature for QTF resonant frequency shifts in (a) air and (b) vacuum.

(k) and fundamental frequency (f_0) [12]: $2df/f_0 \cong (\partial F/\partial z)/k$. The substrate's z-motion is defined relative to the z-position at room temperature (T_0) as $\Delta Z = Z(T) - Z(T_0)$. Therefore, $\Delta Z > 0$ indicates motion of the sample towards the tip, while $\Delta Z < 0$ indicates sample motion away from the tip. Figure 5.4 (a) shows ΔZ for different temperatures at different *df* in air. The larger the *df* is, the QTF is closer to the substrate, therefore it is more sensitive to temperature change. As the temperature increases, while *df* maintains constant (by the SF-AFM feedback controller), the sample stage has to back out ($\Delta Z < 0$) to keep $\partial F/\partial z$ constant, meaning that the forces between the tip and the substrate increase with temperature which can be explained by the fact that kinetic energy of the air molecules between the tip and the substrate increase with temperature resulting in larger forces between the two. This phenomena is vice versa in vacuum condition, meaning the tip-substrate near-field forces decrease as the temperature increases, resulting in the sample stage moving closer to the QTF with temperature increase. Further investigations are required to precisely address these data.

5.3 References

[1] Assy, A., Lefèvre, S., Chapuis, P.O., and Gomès, S., 2014, Analysis of Heat Transfer in the Water Meniscus at the Tip-Sample Contact in Scanning Thermal Microscopy, J. Phys. D. Appl. Phys., 47(44), p. 442001.

[2] Vaisala's calibrator [Online]. Available: http://www.vaisala.com/.

[3] Polder, D., and Van Hove, M., 1971, Theory of Radiative Heat Transfer Between Closely Spaced Bodies, Phys. Rev. B, 4(10), pp. 3303–3314.

[4] Kim, K., Song, B., Fernández-Hurtado, V., Lee, W., Jeong, W., Cui, L., Thompson, D., Feist, J., Reid, M. T. H., García-Vidal, F. J., Cuevas, J. C., Meyhofer, E., and Reddy, P., 2015, Radiative heat transfer in the extreme near field, Nature, 528(7582), pp. 387–391.

[5] Margenau, H., 1939, Van Der Waals forces, Rev. Mod Phys., 11, p. 1.

[6] Casimir, G., 1948, The Influence of Retardation on the London-Van Der Waals Forces, 73(4), pp. 360–372.

[7] Sukenik, C. I., Boshier, M. G., Cho, D., Sandoghdar, V., and Hinds, E. A., 1993, Measurement of the Casimir-Polder force, Phys. Rev. Lett., 70(5), pp. 560–563.

[8] Harber, D. M., Obrecht, J. M., McGuirk, J. M., and Cornell, E. A., 2005, Measurement of the Casimir-Polder Force Through Center-of-Mass Oscillations of a Bose-Einstein Condensate, Phys. Rev. A - At. Mol. Opt. Phys., 72(3), pp. 1–6.

[9] Assy, A., and Gomès, S., 2015, Temperature-Dependent Capillary Forces at Nano-Contacts for Estimating the Heat Conduction Through a Water Meniscus, Nanotechnology, 26(35), p. 355401.

[10] Polesel-Maris, J., Legrand, J., Berthelot, T., Garcia, A., Viel, P., Makky, A., and Palacin, S., 2012, Force Spectroscopy by Dynamic Atomic Force Microscopy on Bovine Serum Albumin Proteins Changing the Tip Hydrophobicity, with Piezoelectric Tuning Fork Self-Sensing Scanning Probe, Sensors Actuators, B Chem., 161(1), pp. 775–783.

[11] Makky, A., Viel, P., Chen, S. W. W., Berthelot, T., Pellequer, J. L., and Polesel-Maris, J., 2013, Piezoelectric Tuning Fork Probe for Atomic Force Microscopy Imaging and Specific Recognition Force Spectroscopy of an Enzyme and its Ligand, J. Mol. Recognit., 26(11), pp. 521–531.

[12] Castellanos-Gomez, A., Agra, N., and Rubio-Bollinger, G., 2011, Force-Gradient-Induced Mechanical Dissipation of Quartz Tuning Fork Force Sensors Used in Atomic Force Microscopy, Ultramicroscopy, 111(3), pp. 186–190.

APPENDIX

TIP-SUBSTRATE THERMAL TRANSPORT ANALYSIS IN AIR AND VACUUM

This appendix discusses quantitative measurement of tip-induced local cooling in air and vacuum environment, providing the possibility to distinguish between different heat transfer mechanisms, conduction through solid-solid contact and air conduction. The results are in good agreement with the theoretical modeling in Chapter 4, where the solid-solid conduction is ~32% of the average of calculated effective thermal conductance in air (i.e. 49 nW/K).

Following the schematic shown in Chapter 4, a nanothermometer/heater is set up for calibration. The temperature coefficient of resistance (TCR) is measured to be 8.3×10^{-4} /K with a sensing current of I = 100 μA. The electrical resistance of the sensing probe is R_0 = 24.88 Ω at room temperature. Figure A.1(a) shows the calibration of the nanothermometer over the range of room temperature to 340 K, and the corresponding TCR. Figure A.1(b) shows the resistance of the sensing probe with respect to input current to the circuit in air and vacuum, indicating the capability of the nanothermometer to be used as a nanoheater. Figure A.1(c) again shows the heater nanowire power with input current again indicating the heating capability of the device. The inset in figure A.1(c) shows the resistance of the heater wire with input current. There is a slight difference

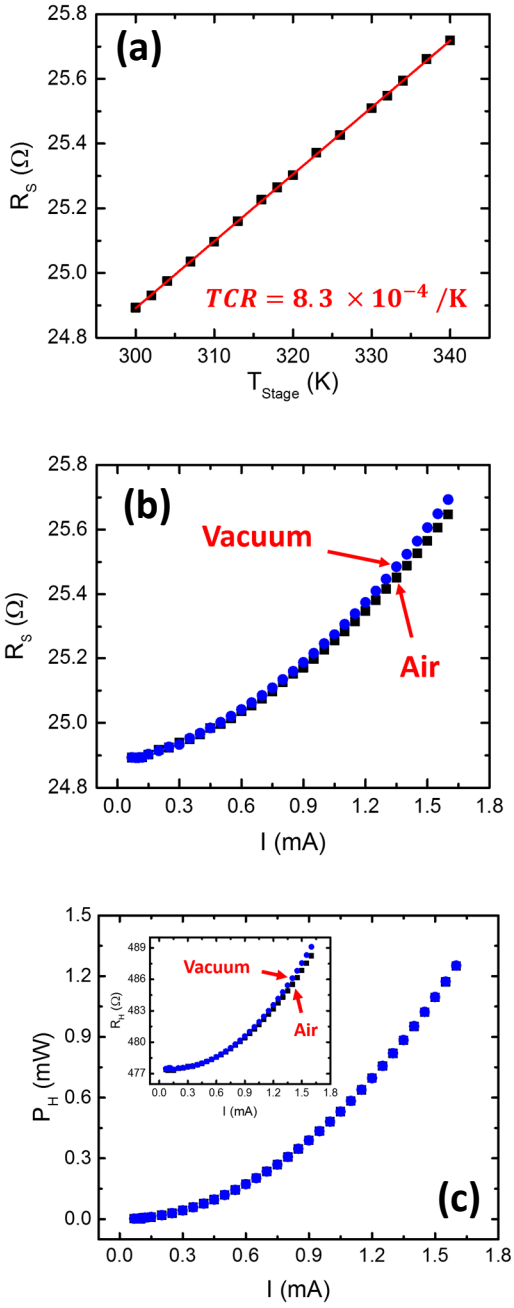

Figure A.1. Calibration of the nanothermometer: (a) Resistance change of the sensing area with the stage temperature is used to calculate the temperature coefficient of resistance in vacuum condition. (b) The electrical resistance change of the sensing probe with input current in air and vacuum showing the heating capability of the device. (c) The electrical power dissipated in the heater line as a function of input current. There is a slight difference within μW scale between the heating power in air and vacuum at higher input currents. The inset shows the electrical resistance change with increasing input current better showing the difference between air and vacuum measurement at high input currents.

between the vacuum and air measurement, showing the cooling effect of air due to free thermal transport between the heater line and the surrounding medium. Using this data, different input currents can be used to set the sensing probe's temperature at the same value weather it is in air or in vacuum. For the tip-induced cooling experiment, input currents of 1.6 mA and 1.55 mA is used in air and vacuum, respectively, corresponding to the sensing probe temperature of 336.5 K. The vacuum pressure used in the experiment is 10^{-5} Torr. Now it is time to conduct the tip-induced cooling experiment same as in Chapter 4.

The tip-induced cooling experiment is conducted using similar Si cantilevers as in Chapter 4, as well as same AFM operating parameters to maintain similar tip-substrate contact force. An input current of 1.6 mA is used to heat up the sensing probe to 336.5K in air environment. The scanning speed is well discussed in Chapter 4, therefore, the same optimum scanning speed is used to scan an area of 2 μm × 2 μm area with maximum thermal transport between the tip and the substrate. After running the experiment in air, the chamber is pumped down to 10^{-5} Torr vacuum pressure, which used to run the experiment in vacuum environment. An input current of 1.55 mA is used in vacuum that results in an elevated temperature of 336.5 K in the sensing probe, equal to the air case. Figure A2 shows the response of the nanothermometer/heater as the tip scans over the sensing area in (a) air and (b) vacuum. The maximum temperature drop in the sensing probe is 9.5 K and 5.2 K in air and vacuum, respectively, corresponding to heating power change of 951 ± 14 nW and 557 ± 25 nW, respectively. Using thermal conductance definition, $\Delta G_C = \Delta P_H / (T_{S,\min} - T_\infty)$, effective thermal conductance is calculated to be 35.2 ± 0.8 nW/K and 17.8 ± 0.9 nW/K in air and in vacuum, respectively. From Chapter 4, effective thermal conductance in air is measured to be 32.5 ± 0.8 nW/K where solid-solid conduction,

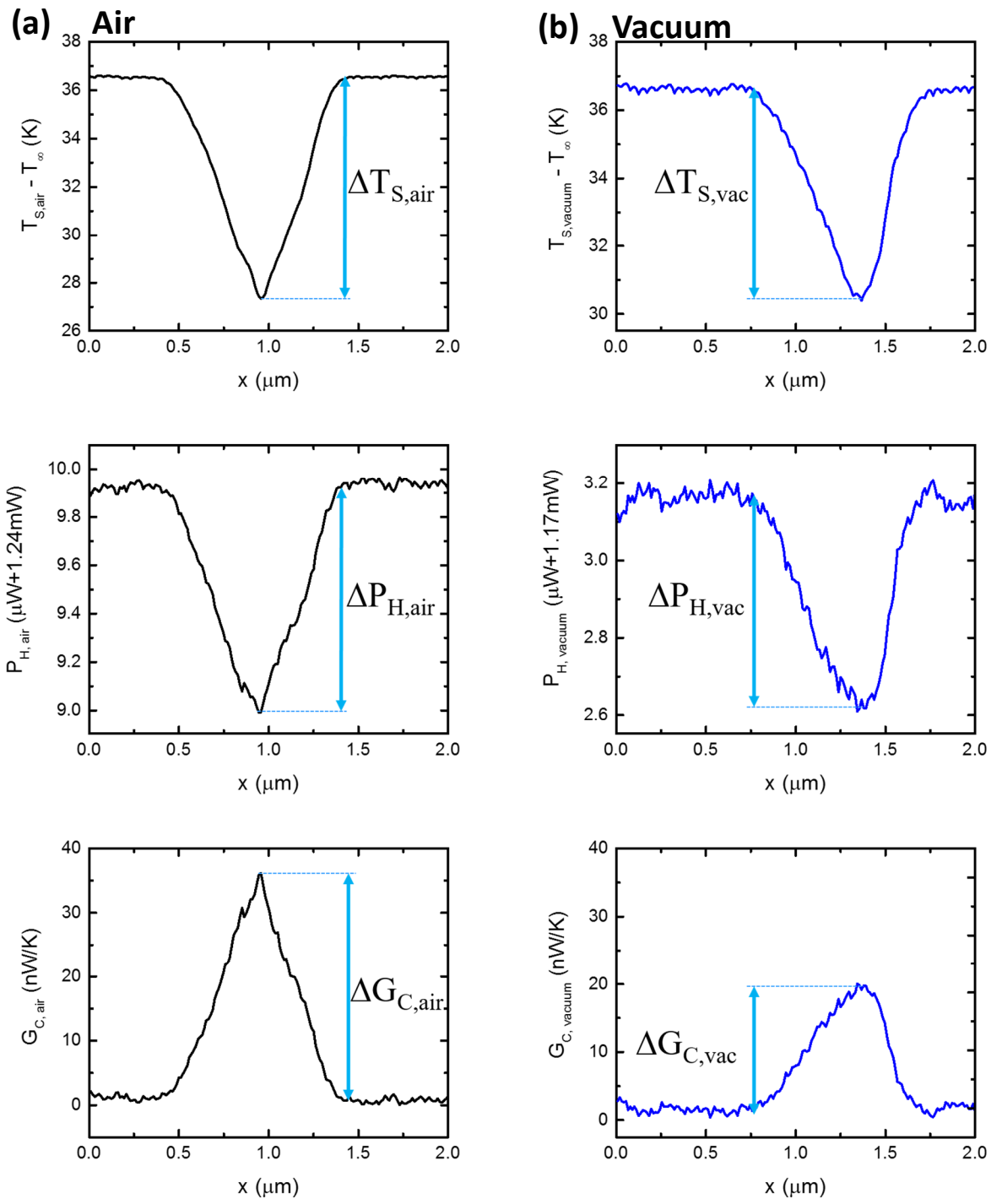

Figure A.2. The sensing probe temperature change and the corresponding heating power response followed by the effective thermal conductance in (a) air and (b) vacuum condition, as the cantilever scans across the sensing probe.

water meniscus conduction, and air contribution are calculated to be 15.7 nW/K, 4.8 – 8.6 nW/K, and 4.5 – 49.8 nW/K, respectively. If it is assumed that there is no water meniscus at that vacuum level, thermal conduction through solid-solid contact has ~50% contribution of total tip-substrate thermal transport for the case of this experiment. This is in good agreement with the ratio of calculated solid-solid conduction to the measured effective thermal conductance in Chapter 4 (i.e., ~48%). This ratio will be larger assuming contribution of water meniscus at its lower value (4.8 nW/K) in vacuum condition: 63%. Implementing the calculated values and using the average value for the calculated air conduction, these ratios will become 32% and 41% with and without water meniscus in vacuum condition.